

Mechatronic design exploration for wide format printing systems

Citation for published version (APA):

Bruijnen, D. J. H. (2007). *Mechatronic design exploration for wide format printing systems*. [Phd Thesis 1 (Research TU/e / Graduation TU/e), Mechanical Engineering]. Technische Universiteit Eindhoven.
<https://doi.org/10.6100/IR628762>

DOI:

[10.6100/IR628762](https://doi.org/10.6100/IR628762)

Document status and date:

Published: 01/01/2007

Document Version:

Publisher's PDF, also known as Version of Record (includes final page, issue and volume numbers)

Please check the document version of this publication:

- A submitted manuscript is the version of the article upon submission and before peer-review. There can be important differences between the submitted version and the official published version of record. People interested in the research are advised to contact the author for the final version of the publication, or visit the DOI to the publisher's website.
- The final author version and the galley proof are versions of the publication after peer review.
- The final published version features the final layout of the paper including the volume, issue and page numbers.

[Link to publication](#)

General rights

Copyright and moral rights for the publications made accessible in the public portal are retained by the authors and/or other copyright owners and it is a condition of accessing publications that users recognise and abide by the legal requirements associated with these rights.

- Users may download and print one copy of any publication from the public portal for the purpose of private study or research.
- You may not further distribute the material or use it for any profit-making activity or commercial gain
- You may freely distribute the URL identifying the publication in the public portal.

If the publication is distributed under the terms of Article 25fa of the Dutch Copyright Act, indicated by the "Taverne" license above, please follow below link for the End User Agreement:

www.tue.nl/taverne

Take down policy

If you believe that this document breaches copyright please contact us at:

openaccess@tue.nl

providing details and we will investigate your claim.

Mechatronic Design Exploration for Wide Format Printing Systems

PROEFSCHRIFT

ter verkrijging van de graad van doctor
aan de Technische Universiteit Eindhoven,
op gezag van de Rector Magnificus, prof.dr.ir. C.J. van Duijn,
voor een commissie aangewezen door het College voor Promoties
in het openbaar te verdedigen
op donderdag 30 augustus 2007 om 16.00 uur

door

Dennis Johannes Hubertinus Bruijnen

geboren te Tegelen

Dit proefschrift is goedgekeurd door de promotor:

prof.dr.ir. M. Steinbuch

Copromotor:

dr.ir. M.J.G. van de Molengraft

This research is supported by Océ-Technologies B.V. in Venlo, The Netherlands.

A catalogue record is available from the Eindhoven University of Technology Library.

Mechatronic Design Exploration for Wide Format Printing Systems / by Dennis J.H. Bruijnen. – Eindhoven : Technische Universiteit Eindhoven, 2007
Proefschrift. – ISBN: 978-90-386-1077-1

Copyright © 2007 by D.J.H. Bruijnen.

This thesis was prepared with the pdfL^AT_EX documentation system.

Cover Design: Oranje Vormgevers, Eindhoven, The Netherlands

Reproduction: Universiteitsdrukkerij TU Eindhoven, Eindhoven, The Netherlands

Summary

Mechatronic Design Exploration for Wide Format Printing Systems

This work aims at increasing the performance of Wide Format Printing Systems (WFPS) via a mechatronic approach. With increasing performance is meant that one or more of the categories: productivity, print quality, reliability and/or cost of production, is improved without sacrificing one of the others. Although the main focus lies on WFPS, the methodology in this work can be extended to a wider class of printers or to other applications.

Multi-printhead scanning inkjet configurations are considered where each printhead contains hundreds of nozzles. This work mainly concentrates on positioning of the 6 degrees of freedom of all printheads in time and space. Questions about what happens inside the nozzles will not be addressed. However, the macroscopic characteristics of the droplet formation process are taken into account, such as jet speed, jet timing and temporary nozzle congestion.

A concept exploration is carried out, including a productivity analysis and a printing accuracy analysis focussing on mechanical design parameters. Both analyses are set up in a generic way such that they can be applied to other printer configurations or to a wider range of applications. Based on this analysis, two concepts are chosen to be investigated further.

The first concept is active printhead alignment. Instead of putting all effort and cost in reduction of the manufacturing tolerances to obtain an accurate printhead alignment for higher productive WFPS, the misalignment of each printhead is measured and actively controlled. A low cost sensor, actuator, and alignment mechanism are developed to achieve this. An experimental setup is built to validate this concept. The concept has been shown to be feasible satisfying the accuracy specification of less than 10 μm . Moreover, this concept enables several extensions, such as (i) adding redundant printheads which take over printing for temporarily congested nozzles, (ii) staggering of printheads in paper transport direction or even distribute the printheads over multiple carriages which would be infeasible for fixed printheads due to thermal effects and parasitic dynamics.

The second concept is a new carriage drive design for higher productive WFPS. A productivity increase can be achieved by increasing the amount of effectively printing nozzles and increasing the jet frequency. As a result, the carriage will be heavier due to the addition of printheads and the carriage speed will need to be increased due to the higher jet frequency. A doubling in mass and speed results in an actuator power increase by a factor of 16 for the case that the effective relative printing time is kept equal. Scaling of the drive in conventional WFPS is therefore expensive and energy inefficient. As an alternative, an energy buffering drive concept is developed which stores the kinetic energy of the carriage in a spring and returns this energy to the carriage in the opposite direction. This way, only a small additional carriage drive is required to overcome friction forces acting on the carriage while moving at a constant speed. To validate this concept, an experimental setup is built. The concept has been shown to be feasible. However, the prototype has to be engineered further to make it simpler such that it becomes cheaper in comparison with an equivalent conventional WFPS where the drive motor has been upscaled.

The mechatronic design of both concepts focus on a much higher performance than conventional WFPS. The results are innovative designs which are easier scalable than conventional methods and enable new features which would not be possible by scaling conventional WFPS.

Contents

Summary	iii
I Motivation	1
1 Introduction	3
1.1 History of Inkjet	3
1.2 Wide Format Printing Systems	6
1.3 Problem Definition and Goal	7
1.4 Design Methodology for Performance Improvement	8
1.5 Outline of this Thesis	11
2 Printing Accuracy Sensitivity Analysis	13
2.1 Notation	13
2.2 Kinematic Model	14
2.3 Linearization of the Dot Positioning Error Model	16
2.4 Dot Positioning Error Example	18
2.5 Error budgeting via the inverse model	18
2.6 Conclusions	23
3 Productivity Analysis of a Wide Format Printing System	25
3.1 Introduction	25
3.2 Printing Process	26
3.3 Productivity Model	28
3.4 Cost Model	29
3.5 Print Process Analysis	30
3.6 Conclusions	33
4 Concept Exploration	35
4.1 Concepts for Improving Printing Accuracy	35
4.2 Concepts for Improving Printing Efficiency	40

II	Active Printhead Alignment	43
5	Printhead Position Sensor	45
5.1	Introduction	45
5.2	A String as an Absolute Reference	46
5.3	Alignment Sensor Design	47
5.4	Measurement Signal Properties	57
5.5	Harmonics Filter Design	60
6	Short Stroke Printhead Guidance Mechanism	65
6.1	Mechatronic Concept	65
6.2	Overview of the Printhead Alignment Mechanism	67
6.3	Design of the Guiding Mechanism	68
6.4	Actuator Design	75
6.5	Eigenmode Analysis	79
6.6	Thermal Analysis	82
7	Active Printhead Alignment Implementation	85
7.1	Experimental Setup	85
7.2	System Identification	87
7.3	Controller Design	88
7.4	Experimental Results	93
7.5	Discussion	99
III	Energy Buffered Carriage Reversal	101
8	Reversal Mechanism Design	103
8.1	Introduction	103
8.2	Concept Exploration	104
8.3	Prototype Design	107
8.4	Design of a Prototype	111
9	Reversal Mechanism Implementation	117
9.1	Experimental Setup	117
9.2	Hybrid Controller Design	119
9.3	System Identification	121
9.4	Controller Synthesis	126
9.5	Experimental Results	127
9.6	Discussion	131
IV	Closing	135
10	Conclusions and Recommendations	137
10.1	Conclusions	137
10.2	Recommendations	140

Bibliography	141
A Efficient Harmonic Disturbance Rejection via Multirate Notch Filtering	149
A.1 Introduction	149
A.2 Method	150
A.3 Simulations	155
A.4 Conclusions	158
B Alternative Printhead Alignment Sensor Methods	161
B.1 Inductive Sensors	161
B.2 Capacitive Sensors	164
B.3 Hall Effect Sensor	167
B.4 Optical Sensors	168
B.5 Conclusions	170
C Optimization Aided Loop Shaping for Motion Systems	171
C.1 Introduction	171
C.2 High Gain Feedback Loop Shaping	172
C.3 Loop Shaping Strategy	176
C.4 Application Description	178
C.5 Loop Shaping Example	180
C.6 Experiments	182
C.7 Conclusions	183
D Redesign of the Drive-aid	185
Samenvatting	189
Dankwoord	191
Curriculum Vitae	193

Part I

Motivation

Chapter 1

Introduction

In this chapter, a brief overview of the history of inkjet is given. More detailed information about the development path of inkjet technology can be found in [36, 46, 54, 57, 59, 82, 93]. Furthermore, the application area of wide format printing systems is introduced after which the problem definition and goal are given. Then, the design methodology followed in this thesis is presented and finally, the outline of this thesis is given.

1.1 History of Inkjet

In 1879, Rayleigh described the mechanism of breaking up a liquid stream into droplets [72]. This mechanism was successfully implemented by Elmqvist in 1951 [20] where it was used as a recording instrument for mechanical or electromechanical measuring devices. In 1965, the first continuous inkjet device was introduced by Sweet [79]. The droplet formation process is shown in Figure 1.1.

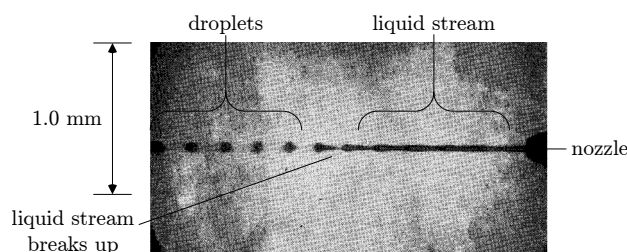


Figure 1.1: Droplet formation process of a liquid inkjet stream (picture from [79]).

In continuous inkjet, droplets of ink are electrostatically charged and deflected depending on a command signal driving an electric field. This process is shown in Figure 1.2. The main application of continuous inkjet at that time was oscillography. About a decade later, in the 1970s, this technology was used to develop the first continuous inkjet printer [12]. A schematic view of this printer is shown in Figure 1.3.

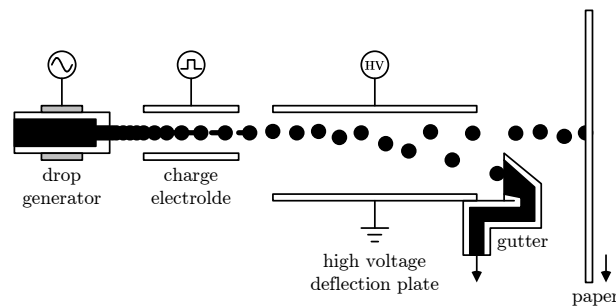


Figure 1.2: Continuous inkjet process, binary deflection principle (image from [57]).

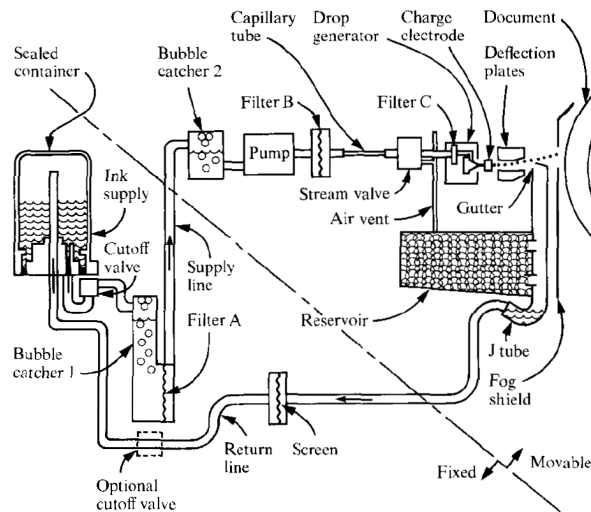


Figure 1.3: Schematic view of the first continuous inkjet printer (image from [12]).

At the same time, drop-on-demand inkjet systems were developed where only droplets are ejected when required, instead of continuously ejecting droplets while intercepting droplets that should not reach the print media. In [97], a piezo actuator is used to create a pressure wave in a nozzle to eject a droplet. These systems could not compete with continuous inkjet because the reliability of these systems remained poor. In 1979, a drop-on-demand inkjet method was developed simultaneously by HP [89] and Canon [21] based on the growth and collapse of a

water vapor bubble using a small heat element near the nozzle, also called thermal inkjet or bubble jet. The thermal inkjet principle is shown in Figure 1.4.

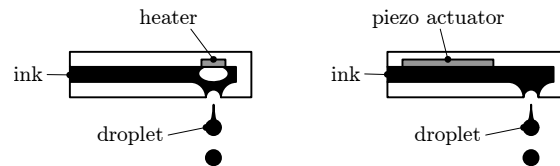


Figure 1.4: Principle of thermal inkjet and piezoelectric inkjet.

This technology resulted in the first successful low-cost inkjet printer, the HP ThinkJet printer, introduced in 1984. The reliability issue was solved by making the inkjet printheads disposable, also called ink cartridges.

In the late 1980s, thermal inkjet began to gain ground replacing impact dot-matrix printers and currently, thermal inkjet is dominant in the low-end consumer market [4]. In 1993, Epson introduced the first low-cost reliable piezoelectric printer with a permanent printhead which was a direct competitor of thermal inkjet.

More drop-on-demand methods have been developed recently, such as electrostatic [45] and acoustic inkjet, to meet with the ever increasing specifications on productivity, print quality, cost and reliability, boosted by the expanding semiconductor industry. In Figure 1.5, an overview of developed inkjet technologies is given.

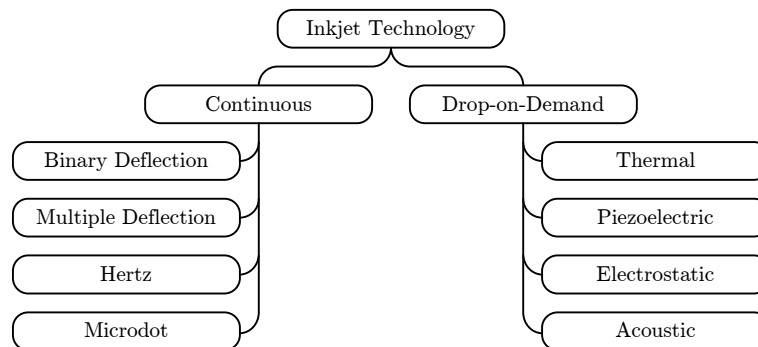


Figure 1.5: Overview of inkjet technologies [57].

Inkjet technology has also been applied to a larger variety of print media, from paper and textile to tiles and doors and print media from a few centimeters to a few meters wide. Important inkjet technology markets are: small home/ office, home photo, office network, display graphics, industrial/postal marking, large format, color copier, digital color press, textile, 3D printing, computer-to-plate and more.

1.2 Wide Format Printing Systems

Besides the inkjet printers for the small home/ office market, also printers have been developed for the professional market to print advertising graphics and designs of architects and engineers. For this market, the print media are generally larger than for the low-end consumer market, categorized by wide format: 24"-100" (= 0.61 m - 2.54 m) and grand format: >100" (= 2.54 m). Depending on speed, quality, resolution, print media and reliability, prices vary from € 10k to over € 1000k. An example of wide format printing systems (WFPS) is shown in Figure 1.6.



Figure 1.6: Océ TCS500, a wide format printing system with a wide format scanner and control unit.

A schematic view of WFPS is shown in Figure 1.7. To obtain an acceptable printing throughput and resolution, WFPS contain hundreds of nozzles to jet ink onto the print medium. However, a print-medium-wide printhead is not feasible because it would contain ten thousands of nozzles which is way too expensive and unreliable. Therefore, WFPS are equipped with a carriage that is moving across the paper containing several printheads. Each printhead contains an amount of nozzles typically in the order of 10^2 . Printheads of several colors are staggered to enable color printing. A typical printing resolution is 600 dpi, however, a single printhead can only reach a resolution in the order of 100 dpi with a single swath due to manufacturing limitations. A swath is defined as one pass of the carriage across the print medium. To obtain the required printing resolution of 600 dpi, multiple printheads and/or multi-pass are used. Multi-pass is the process of using several swaths passing the same print area to obtain the required resolution (see Figure 3.2).

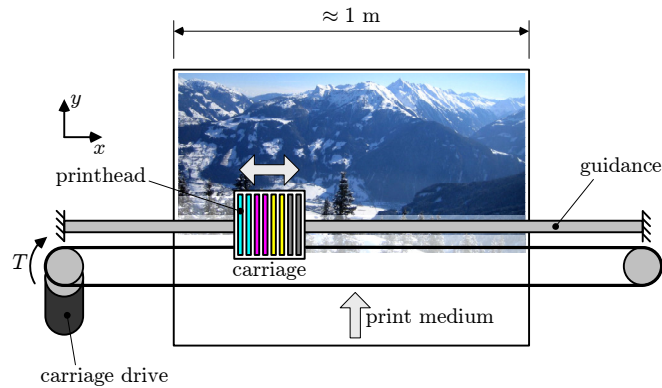


Figure 1.7: A schematic overview of WFPS. This particular example shows a configuration with a carriage moving across the print medium which contains two printheads for each color. The printing resolution of one printhead is in the order of 100 npi (nozzles per inch). The required resolution is obtained by overlapping three swaths resulting in $100 \text{ npi} \times 2 \text{ printheads} \times 3 \text{ swaths} = 600 \text{ dpi}$ printing resolution.

1.3 Problem Definition and Goal

The design of WFPS is a trade-off between productivity, print quality, reliability and cost of production. A lot of disciplines are involved in this trade-off including mechanics, electronics, software, control, physics, and chemistry. The synergy of multiple disciplines, especially mechanics, electronics, software and control, is denoted as mechatronics. This integration of the involved disciplines is complex but crucial to obtain a successful design. This work aims at increasing the performance of WFPS via a mechatronic approach which is the process of trading off multiple disciplines in the design space. With increasing performance is meant that one or more of the categories: productivity, print quality, reliability and/or cost of production, is improved without sacrificing the other categories. The main focus lies on WFPS, however, extension to a wider class of printers or other applications is possible. The problem definition is formulated as follows:

Exploration of the mechatronic design space to improve WFPS in terms of productivity, print quality, reliability, and cost of production.

Multi-printhead scanning inkjet configurations are considered where each printhead contains hundreds of nozzles. This work mainly concentrates on positioning of the 6 degrees of freedom of all printheads in time and space. Questions about what happens inside the nozzles will not be addressed. However, the macroscopic characteristics of the droplet formation process are taken into account, such as varying jet speed, varying jet timing and temporary nozzle congestion.

The goal of this work is to come up with innovative solutions to improve higher productive WFPS. The followed design procedure in this work is shown below:

1. Investigate the influence on performance of printer design parameters which are related to printhead positioning in time and space.
2. Explore mechatronic concepts to improve performance.
3. Work out promising concepts.
4. Validate concepts by carrying out simulations, realizing experimental setups and conducting experiments for proof-of-concept.

The two worked out concepts are: (i) active printhead alignment, and (ii) energy buffered carriage reversal. In the active printhead alignment concept, the position of each printhead located at the carriage is measured with respect to a string which is tensioned parallel to the carriage guidance. This results in a better printhead alignment accuracy without being limited by manufacturing tolerances. For higher productive WFPS, a better print quality is obtained compared to scaling conventional WFPS. In Part II, this concept is investigated in detail. In the energy buffered carriage reversal concept, a spring is used to buffer the kinetic energy of the carriage while reversing. This way, only a small actuator is needed to keep the carriage at a constant speed while printing. The spring stiffness and carriage mass determine the reversal time independent of the carriage speed. For higher productive WFPS, this concept scales easily while a large carriage drive is required when scaling conventional WFPS as investigated in detail in Part III.

1.4 Design Methodology for Performance Improvement

The first drop-on-demand printers were developed in the 1980s. The amount of printers made and the range of applications have grown enormously since then, hence, how to transfer ink from an ink reservoir onto the print medium is extensively explored and exploited. Performance specifications increase steadily using the established technique. By optimizing the design for conventional WFPS, small steps in performance are made, however, over the years, the design optimization converges towards design boundaries. When such a boundary has been reached, the performance can only be improved by a large conceptual step. There is an analogy with optimizing a complex, non-convex function: with downhill methods, the objective function is optimized towards the nearest local optimum. However, to be able to jump to another, better local optimum a large step in the search space has to be made and afterwards being optimized again with downhill methods.

The design exploration in this work is aimed at making such a large step in the search space resulting in a large step in performance with the potential to be exploited to improve the performance even further. In literature, several de-

sign methodologies are proposed [34, 35, 65]. These methods describe the design methodology for the entire product development from customer to realized product, whereas the design methodology presented below is more specific and focuses on concept innovation for a given research problem. The intention of the methodology is to trigger research to make a large step in the design space as shown in Figure 1.8 and explained below:

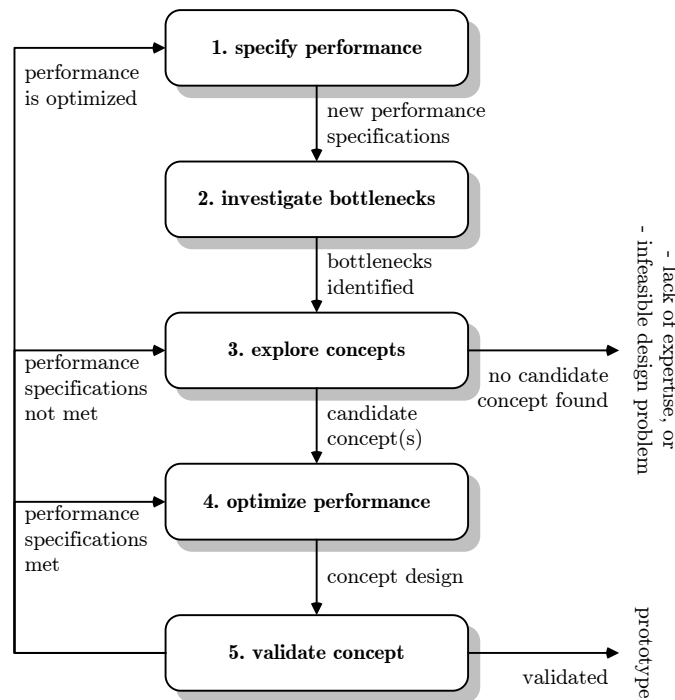


Figure 1.8: Methodology for performance improvement.

1. **specify performance:** the starting point is a concept which has been optimized against design boundaries. To trigger research to make a huge step in the search space, the performance specifications are tightened enormously, e.g. at least doubling the performance. The term 'performance' can contain specifications such as accuracy, productivity, reliability and/or cost of production.
2. **investigate bottlenecks:** due to the increase of the performance specifications in step 1, boundaries are crossed because of the assumption that the design is optimized against the design boundaries resulting in an infeasible design. By analyzing the influence of design parameters on the performance, the main design parameters are captured causing the bottlenecks.
3. **explore concepts:** after the bottlenecks have been identified in step 2, a concept exploration is carried out to overcome the limitations regarding the

involved design parameters. This is a very creative step. The creativity mostly lies in combining existing methods to come up with innovative solutions. If no feasible concept is found, then (i) the problem can be infeasible or (ii) the group of designers have a lack of expertise or imagination.

4. **optimize performance:** if a concept is found in step 3 that has the potential to fulfill the performance specifications, then a solution is found close to another (local) optimum. The found concept is not yet the local optimum because exploitation has not been taken place yet in that part of the search space. By alternating between (i) optimizing the performance specifications by changing the design parameters and (ii) keeping the performance specifications equal while redistributing the design parameters, the local optimum in the search space is approached.
5. **validate concept:** to show that the concept is indeed feasible, simulations and experiments with a prototype have to be carried out because theory will generally not foresee everything in practice. After this step, step 4 can be repeated several times until the performance cannot be improved anymore, and hence, we go back to step 1. If for some reason, performance specifications were not met due to problems found in practice, we have to return to step 3.

This design methodology for improving performance can now be projected onto improving WFPS as is the focus of this thesis. Key ideas and connections with parts in this thesis will be pointed out.

1. **specify performance:** performance specifications in the field of WFPS are e.g. print quality, reliability, productivity, and cost of production as presented in this chapter. The search space involves knowledge of a wide range of disciplines, such as mechanics, dynamics, physics, chemistry and computer science. Print quality and productivity are converging towards design boundaries due to manufacturing tolerances and scaling difficulties of conventional methods which are cost related. This thesis deals with both printing accuracy (improvement $\sim 4\times$) and print productivity (improvement $\sim 4\times$) which is a large step beyond the design boundaries.
2. **investigate bottlenecks:** the bottlenecks are determined by investigating the influence of design parameters on the printing accuracy in Chapter 2 and on the productivity in Chapter 3. Found bottlenecks are printhead alignment and printing efficiency for higher productive WFPS.
3. **explore concepts:** mechatronics is a relatively young field of research which exploits the synergy of the range of disciplines mentioned in step 1. The field of mechatronics expands the search space, hence, chances increase that there exist better local optima to fulfill the performance specifications. After having determined the bottlenecks in step 2, a concept exploration is conducted in Section 4.1 and Section 4.2. The two most promising concepts have been chosen for further investigation in Part II and Part III.

4. **optimize performance:** in Chapter 5, Chapter 6, and Chapter 8 both concepts will be investigated by trading off the design parameters to obtain the performance specifications. In Chapter 2 and Chapter 3 several methods have been presented for this, e.g., in Section 2.5, a systematic method has been presented which keeps the performance specification constant while redistributing the design parameters as chosen by the engineer.
5. **validate concept:** in Chapter 7 and Chapter 9, experiments with the prototypes will be presented that validate the designed concepts. Both concepts show to be promising, however, they are the first prototypes which can still be improved by further engineering, hence, future work implies to go back to step 4 again.

1.5 Outline of this Thesis

This thesis is divided into 4 parts. The motivation for this research is written in Part I. In Chapter 2, the dot positioning sensitivity subjected to the 6 degrees of freedom is investigated. In Chapter 3, the influence of mechanical design parameters on the printer productivity is investigated. In Chapter 4, mechatronic concepts are introduced from which two are investigated. These two concepts are presented in Part II and Part III.

In Part II, the active printhead alignment concept is presented. In Chapter 5, the design of the printhead position sensor is described and analyzed. In Chapter 6, the design of the short stroke guidance mechanism is described and analyzed including the actuator design and the short stroke guidance design. Experiments of the total integration of the printhead alignment concept are presented in Chapter 7.

In Part III, the energy buffered carriage reversal concept is presented. In Chapter 8, the design of the drive-aid is described including concept exploration, modeling, and simulation. In Chapter 9, the experimental setup is described, the controller design is presented and the experimental results are shown.

In Part IV, conclusions and recommendations for further research are given.

Chapter 2

Printing Accuracy Sensitivity Analysis

In this chapter, an investigation is presented of how dot positioning deviations depend on design parameters and their tolerances. A generic 3D kinematic model is derived which can be evaluated analytically. A linearization of the obtained model is analyzed which is a valid approximation because we only deal with small variations. Based on the inverse model, a method for error budgeting is presented.

2.1 Notation

$\{X, \underline{\bar{e}}^X\}$	a frame with origin X and orientation $\underline{\bar{e}}^X$
X	a body-fixed point
$\underline{\bar{e}}^X$	an orientation which is a set of three mutually orthogonal unit vectors $[\ \bar{e}_1^X \ \bar{e}_2^X \ \bar{e}_3^X \]^T$
$\vec{r}_{Y/X}$	a vector which indicates the position of point Y relative to point X
$\vec{r}_{Y/X} _{\underline{\Delta}=0}$	a vector which indicates the nominal position of point Y relative to point X where the variations in $\underline{\Delta}$ are equal to zero
$\underline{\Delta}$	variations array
Δx	variation of scalar x
$\underline{\Delta x}$	variation of array \underline{x}
Δx_3	third element of $\underline{\Delta x}$
$r_{Y/X}^X$	coordinate of point Y in the frame $\{X, \underline{\bar{e}}^X\}$
$\underline{A}^{YX}(\alpha)$	direction cosine matrix which describes the rotation from $\underline{\bar{e}}^X$ to $\underline{\bar{e}}^Y$. The rotation order has to be fixed to obtain a unique solution. A rotation order $(\alpha_1, \alpha_2, \alpha_3)$ is used (also called Tait-Bryant angles).

2.2 Kinematic Model

The positioning accuracy of a dot relative to dots in its neighborhood is an essential part to obtain a good print quality. The dot positioning accuracy is determined by many design parameters. To determine the relation between these design parameters and their tolerances, a kinematic model is developed. The set of parameters consist mainly of mechanical parameters such as geometry parameters, carriage speed v_c and jet speed v_j . These parameters can show small variations i.e. their tolerances. Because we only consider small variations, a linearization of the kinematic model is a good approximation and will be investigated. Furthermore, the print surface is assume to be flat. Print medium height variations can be taken into account via the nozzle-paper distance h .

Some conclusions about how to maintain/improve accuracy when productivity is increased will be drawn by means of this linearized model.

The kinematic model describes where a single nozzle jets an ink droplet onto the print medium. Parameters which are taken into account are:

- (i) the position of the carriage C relative to the print medium P , $\vec{r}_{C/P}$ which includes the carriage speed v_c in m/s and nozzle-paper distance h in m,
- (ii) the location of the nozzle N relative to the center of the carriage C , $\vec{r}_{N/C}$ which includes the nozzle position coordinates x in m and y in m,
- (iii) the location of an ink dot D jetted by the nozzle N , $\vec{r}_{D/C}$ which includes the carriage speed v_c in m/s, and the jet speed v_d in m/s.

Variations which are taken into account are:

- (i) the angular orientation of the carriage $\Delta\theta \in \mathbb{R}^3$,
- (ii) the slant jetting of the nozzle $\Delta\varphi \in \mathbb{R}^2$,
- (iii) the variation of the carriage position $\Delta\vec{r}_c \in \mathbb{R}^3$,
- (iv) the variation of the nozzle location $\Delta\vec{r}_n \in \mathbb{R}^3$,
- (v) the carriage speed variation $\Delta v_c \in \mathbb{R}$,
- (vi) the jet speed variation $\Delta v_d \in \mathbb{R}$, and
- (vii) the jet timing variation $\Delta t \in \mathbb{R}$.

These variations are gathered in the variations array $\underline{\Delta} \in \mathbb{R}^{14}$:

$$\underline{\Delta} = [\Delta\theta^T \quad \Delta\varphi^T \quad \Delta\vec{r}_c^T \quad \Delta\vec{r}_n^T \quad \Delta v_c \quad \Delta v_d \quad \Delta t]^T \quad (2.1)$$

In Figure 2.1, an illustration of these parameters with their variations is shown. We introduce three bodies: the print medium, the carriage and a single nozzle where the frames $\{P, \vec{e}^P\}$, $\{C, \vec{e}^C\}$ and $\{N, \vec{e}^N\}$ are attached to respectively. The orientations of these frames are related as follows:

$$\vec{e}^C = \underline{A}^{CP} \vec{e}^P \quad (2.2)$$

$$\vec{e}^N = \underline{A}^{NC} \vec{e}^C = \underline{A}^{NC} \underline{A}^{CP} \vec{e}^P \quad (2.3)$$

is composed of the carriage position relative to the print medium $\underline{r}_{C/P}^P(t)$, (2.7), the nozzle position relative to the carriage $\underline{r}_{N/C}^C$, (2.8), and the dot position relative to the nozzle location $\underline{r}_{D/N}^N$, (2.9):

$$\underline{r}_{C/P}^P(t) = [(v_c + \Delta v_c)t \quad 0 \quad h] + \Delta \underline{r}_{C/P}^P \quad (2.7)$$

$$\underline{r}_{N/C}^C = [x \quad y \quad 0] + \Delta \underline{r}_{N/C}^C \quad (2.8)$$

$$\begin{aligned} \underline{r}_{D/N}^N &= [0 \quad 0 \quad -t_d(v_j + \Delta v_j)] + \dots \\ &[(v_c + \Delta v_c)(t_d + \Delta t) \quad 0 \quad 0] \underline{A}^{PC} \underline{A}^{CN} \end{aligned} \quad (2.9)$$

in which t is the moment that a droplet has to be jetted in s. The time of flight of the droplet t_d is computed by solving:

$$t_d = \{t_d \in \mathbb{R}^+ | r_{3,D/P}^P(t) = 0\} \quad (2.10)$$

where the print surface lies in the $(\vec{e}_1^P, \vec{e}_2^P)$ -plane. From (2.6) and (2.10) we obtain the dot positioning error $\Delta \underline{e} \in \mathbb{R}^2$:

$$\Delta \underline{e}(t) = \begin{bmatrix} 1 & 0 & 0 \\ 0 & 1 & 0 \end{bmatrix} \left(\underline{r}_{D/P}^P(t) - \underline{r}_{D/P}^P(t) \Big|_{\Delta=0} \right) \quad (2.11)$$

2.3 Linearization of the Dot Positioning Error Model

The analytic result of (2.11) is nonlinear so interpretation is difficult. To improve clarity and because we only deal with relatively small variations, we will investigate the linearization of $\Delta \underline{e}(t)$ instead denoted by $\Delta \underline{e}^*(t)$:

$$\Delta \underline{e}^*(t) = \underbrace{\Delta \underline{e}(t) \Big|_{\Delta=0}}_{\begin{bmatrix} 0 \\ 0 \end{bmatrix}} + \underbrace{\left(\frac{\partial \Delta \underline{e}(t)}{\partial \Delta} \Big|_{\Delta=0} \right)^T}_{\underline{E}} \Delta = \underline{E} \Delta \quad (2.12)$$

where

$$\underline{E} = \begin{bmatrix} \frac{v_c}{v_j} y & -h - \frac{v_c}{v_j} x & -y & 0 & -h & 1 & 0 & \frac{v_c}{v_j} & 1 & 0 & \frac{v_c}{v_j} & + \frac{h}{v_j} & -\frac{v_c}{v_j} \frac{h}{v_j} & v_c \\ h & 0 & x & h & 0 & 0 & 1 & 0 & 0 & 1 & 0 & 0 & 0 & 0 \end{bmatrix} \quad (2.13)$$

In Table 2.1, a qualitative overview of the influence of parameters onto the sensitivity to the variations is given based on (2.12) using the absolute value. Time t is disregarded and set equal to zero further, because a constant deviation of v_c does not harm printing accuracy because jet timing is usually done position-based in printers. For now, the variations $\underline{\Delta}$ are considered to be constant to give a qualitative overview.

Table 2.1: A qualitative overview of the influence of printhead design parameters onto the sensitivity to the variations $\underline{\Delta}$ where \vec{e}_1^P is the carriage movement direction and \vec{e}_2^P is the paper transport direction.

increase	effect in \vec{e}_1^P	effect in \vec{e}_2^P
x	$+\Delta\theta_2$	$+\Delta\theta_3$
y	$+\Delta\theta_1, +\Delta\theta_3$	none
h	$+\Delta\theta_2, +\Delta\varphi_2, +\Delta v_c, +\Delta v_j$	$+\Delta\theta_1, +\Delta\varphi_1$
v_c	$+\Delta\theta_1, +\Delta\theta_2, +\Delta r_{c3}, +\Delta r_{n3}, +\Delta v_j, +\Delta t$	none
v_j	$-\Delta\theta_1, -\Delta\theta_2, -\Delta r_{c3}, -\Delta r_{n3}, -\Delta v_c, -\Delta v_j$	none

Aim at Accuracy

A better printing accuracy for given variations $\underline{\Delta}$ can be obtained by decreasing the sensitivity of the printing accuracy to $\underline{\Delta}$ indicated by Table 2.1. For example, if x increases, the sensitivity to the variations $\Delta\theta_2$ and $\Delta\theta_3$ increases in the directions \vec{e}_1^P and \vec{e}_2^P respectively. Table 2.1 shows that the sensitivity of the printing accuracy to the variations can be decreased by:

- (i) decreasing the carriage speed v_c ,
- (ii) increasing the jet speed v_j ,
- (iii) decreasing the size of the carriage by decreasing the amount of nozzles such that the average x and y for all nozzles becomes smaller.
- (iv) decreasing the nozzle-paper distance h .

Calibration by adjusting the jet timing as a function of the carriage position can already reduce a large amount of repetitive variations in carriage movement direction \vec{e}_1^P . These variations, shown in Table 2.1, also contain a non-repetitive part in practice, such as the carriage drive servo error (which increases Δv_c), droplet formation dynamics (which increases Δv_j , $\Delta\varphi$), and parasitic dynamics (which increases $\Delta\theta$, Δr_c), which cannot be dealt with by calibration. Moreover, such calibration can not improve printing accuracy in print medium transport direction \vec{e}_2^P . Hence, to improve printing accuracy, it is not sufficient to only apply advanced calibration.

Trade-Off Between Accuracy and Productivity

Increasing both the accuracy and productivity results in conflicting demands. For the carriage size and speed there is a trade-off between accuracy and productivity.

On the contrary, jet speed and nozzle-paper distance only influence accuracy and do not influence productivity.

According to Chapter 3, an increase of productivity can be realized by moving the carriage faster (i.e. increasing the jet frequency) and increasing the amount of nozzles (i.e. increasing the carriage size). To maintain the printing accuracy without changing $\underline{\Delta}$, we have to increase the jet speed and to decrease the nozzle-paper distance. Or else, $\underline{\Delta}$ has to be decreased by tightening manufacturing tolerances or by measuring and regulating errors via active control.

2.4 Dot Positioning Error Example

The variables in $\Delta e^*(t)$ and in $\underline{\Delta}$ are considered to be stochastic variables with a gaussian probability distribution. Assuming that $\mathbb{E}\Delta e^*(t) = \underline{0}$ we obtain from (2.12):

$$\sigma(\Delta e^*(t)) = \sqrt{(\underline{E} \cdot \underline{E})(\sigma \underline{\Delta})^2} \quad (2.14)$$

where \cdot denotes the Hadamard product or entrywise product. The assumption that the variations are uncorrelated is of course not entirely true but it is useful to make a qualitative comparison between a reference printer and a printer with a 4 times higher productivity obtained by doubling the amount of nozzles and doubling the carriage speed. Because the carriage size is increased, printhead position variations are also increased, assuming an increase of 50%. In Table 2.2, the dot positioning error of both printers is compared. The dot positioning accuracy deteriorates with a factor of 2.3. Together with increasing productivity and print quality requirements, the dot positioning accuracy has to be improved even more than a factor of 2.3. In Chapter 4, these results will be further used for concept exploration.

2.5 Error budgeting via the inverse model

In the previous section, the resulting dot positioning error is computed via a linearized kinematic model. The contribution of each variation to the total dot positioning error is computed. However, from an engineering point of view, the dot positioning error is specified which has to be distributed over the variations present in the printer design or another positioning application. In this section a method is presented to do this so-called error budgeting systematically based on the derived linearized kinematic model.

For error budgeting we have to make $\underline{\Delta}$ a function of Δe^* such that we can choose the required dot positioning error directly instead of iterating with $\underline{\Delta}$. According

with null space mapping:

$$\ker(\underline{A}) = \{\underline{x} \in \mathbb{R}^n \mid \underline{A}\underline{x} = \underline{0}\} \quad (2.18)$$

which maps the collection of vectors in \mathbb{R}^n to the zero vector in \mathbb{R}^m for matrix $A^{m \times n}$. For clarity of notation, the vectors which span $\ker(\underline{A})$ are joined into a matrix. The parameters \underline{p}^* can be tuned for error budgeting while satisfying (2.14) and (2.15). If we combine (2.14), (2.15) and (2.17) we obtain:

$$\underbrace{\begin{bmatrix} (\sigma(\Delta \underline{e}^*(t)))^2 \\ \underline{0}^{r \times 1} \\ \underline{p}^* \end{bmatrix}}_{\underline{p}} = \underbrace{\begin{bmatrix} \underline{E} \cdot \underline{E} \\ \underline{R} \\ \ker \left(\begin{bmatrix} \underline{E} \cdot \underline{E} \\ \underline{R} \end{bmatrix} \right)^T \end{bmatrix}}_{(\underline{B}^{n \times n})^{-1}} (\sigma \underline{\Delta})^2 \quad (2.19)$$

$$(\sigma \underline{\Delta})^2 = \underline{B}^{n \times n} \underline{p} = \begin{bmatrix} \underline{B}_1^{n \times (n-p)} & \underline{B}_2^{n \times p} \end{bmatrix} \underline{p} \quad (2.20)$$

where $\underline{B}^{n \times n}$ has rank n , i.e. it contains a unique inverse and \underline{p}^* has to be chosen such that $(\sigma \underline{\Delta})^2 \geq (\sigma \underline{\Delta}_{min})^2$. The vector $\sigma \underline{\Delta}_{min}$ is the minimum standard deviation of the variations $\underline{\Delta}$. We can rewrite this to a set of linear matrix inequalities (LMIs):

$$\begin{aligned} \underline{B}_1 \begin{bmatrix} (\sigma(\Delta \underline{e}^*))^2 \\ \underline{0}^{r \times 1} \end{bmatrix} + \underline{B}_2 \underline{p}^* &\geq (\sigma \underline{\Delta}_{min})^2 \\ -\underline{B}_2 \underline{p}^* &\leq \underline{B}_1 \begin{bmatrix} (\sigma(\Delta \underline{e}^*))^2 \\ \underline{0}^{r \times 1} \end{bmatrix} - (\sigma \underline{\Delta}_{min})^2 \end{aligned} \quad (2.21)$$

This can be solved using linear programming, quadratic programming or an LMI-solver depending on the choice for the objective function which can be chosen freely. In our case, we choose for linear programming resulting in the objective function $\underline{f}^T \underline{p}^*$ which results in a linear trade-off between the four degrees of freedom. The optimization problem becomes:

$$\min_{\underline{p}^*} \underline{f}^T \underline{p}^* \quad (2.22)$$

For the given parameters in the reference printer shown in the left column of

Table 2.2 we obtain the following null-space:

$$\ker \left(\begin{bmatrix} \underline{E} \cdot \underline{E} \\ \underline{R} \end{bmatrix} \right) = \begin{bmatrix} 1 & 0 & 0 & 0 \\ 1 & 0 & 0 & 0 \\ 1 & 0 & 0 & 0 \\ 0 & 1 & 0 & 0 \\ 0 & 1 & 0 & 0 \\ -5 \cdot 10^{-3} & -5 \cdot 10^{-7} & 0 & 0 \\ -5 \cdot 10^{-3} & -5 \cdot 10^{-7} & 0 & 0 \\ -5 \cdot 10^{-3} & -5 \cdot 10^{-7} & 0 & 0 \\ -5 \cdot 10^{-3} & -5 \cdot 10^{-7} & 0 & 0 \\ -5 \cdot 10^{-3} & -5 \cdot 10^{-7} & 0 & 0 \\ -5 \cdot 10^{-3} & -5 \cdot 10^{-7} & 0 & 0 \\ 0 & 0 & 1 & 0 \\ 0 & 0 & 0 & 1 \\ 9 \cdot 10^{-3} & 2 \cdot 10^{-8} & -2 \cdot 10^{-8} & -4 \cdot 10^{-10} \end{bmatrix} \quad (2.23)$$

Considering (2.23) and the order of magnitude of the variations as shown in Table 2.2, the dominant standard deviations of the variations in the cost function can be determined. The first column represents the degree of freedom where the carriage orientation variations $\Delta\theta$ are dominant in comparison to the carriage and nozzle position variations. The second degree of freedom is dominated by the slant jetting with respect to the position and jet timing variations. The third and last column are dominated by variations of the carriage speed and the jet speed respectively. Herein, the jet timing has a negligible influence.

As an example we use:

$$f = [1 \quad 1 \quad 1 \quad 1]^T \quad (2.24)$$

which means that we want to increase the position variations at the cost of the remaining variations. Furthermore, as a lower bound on $\sigma\Delta$ we choose:

$$\sigma\Delta_{min} = [5 \cdot 10^{-3} \quad 5 \cdot 10^{-3} \quad 5 \cdot 10^{-3} \quad 5 \cdot 10^{-2} \quad 5 \cdot 10^{-2} \quad \dots \\ 10^{-6} \quad 10^{-6} \quad 10^{-6} \quad 10^{-6} \quad 10^{-6} \quad 10^{-2} \quad 10^{-1} \quad 10^{-6}]^T \quad (2.25)$$

Error budgeting keeping the dot positioning error variance equal

The optimization problem (2.22) subjected to the LMIs (2.21) is solved using linear programming (Matlab: LINPROG). The result compared with the result for the reference printer is shown in Table 2.3. The position variations are increased at the cost of the other variations as expected. The total dot positioning error Δe^* is computed by (2.14) which remains equal with respect to the reference printer. However, the error contribution in both directions is changed. By changing the optimization parameters f and the lower bound of the standard deviations $\sigma\Delta_{min}$, the dot positioning error variance can be easily redistributed over the variations which is a common task in product design.

Table 2.3: Dot positioning error Δe^* in μm for two sets of parameters and variations. Left table: reference printer with parameters $x = 0.1$ m, $y = 0.03$ m, $h = 1$ mm, $v_c = 1.0$ m/s, $v_j = 7.0$ m/s, right table: a change in variations while keeping the total dot positioning error equal.

reference printer				error budgeted printer			
Δ	1σ	$\sigma\Delta e_1^*$	$\sigma\Delta e_2^*$	Δ	1σ	$\sigma\Delta e_1^*$	$\sigma\Delta e_2^*$
$\Delta\theta_1$	0.020 °	1.50	0.35	$\Delta\theta_1$	0.019 °	1.41	0.30
$\Delta\theta_2$	0.020 °	5.34	0.00	$\Delta\theta_2$	0.019 °	5.04	0.00
$\Delta\theta_3$	0.020 °	10.47	34.91	$\Delta\theta_3$	0.019 °	9.90	32.99
$\Delta\varphi_1$	0.50 °	0.00	8.73	$\Delta\varphi_1$	0.05 °	0.00	0.87
$\Delta\varphi_2$	0.50 °	8.73	0.00	$\Delta\varphi_2$	0.05 °	0.87	0.00
Δr_{c1}	5.0 μm	5.00	0.00	Δr_{c1}	11.3 μm	11.30	0.00
Δr_{c2}	5.0 μm	0.00	5.00	Δr_{c2}	11.3 μm	0.00	11.30
Δr_{c3}	5.0 μm	0.71	0.00	Δr_{c3}	11.3 μm	1.61	0.00
Δr_{n1}	5.0 μm	5.00	0.00	Δr_{n1}	11.3 μm	1.14	0.00
Δr_{n2}	5.0 μm	0.00	5.00	Δr_{n2}	11.3 μm	0.00	11.30
Δr_{n3}	5.0 μm	0.71	0.00	Δr_{n3}	11.3 μm	1.61	0.00
Δv_c	0.030 m/s	4.29	0.00	Δv_c	0.010 m/s	1.43	0.00
Δv_j	0.50 m/s	10.20	0.00	Δv_j	0.10 m/s	2.04	0.00
Δt	2.0 μs	2.00	0.00	Δt	1.0 μs	1.00	0.00
total: ($\ \cdot\ _2$)		19.85	36.67	total: ($\ \cdot\ _2$)		19.85	36.67

Error budgeting with a decreased dot positioning error variance

The described error budgeting method can also be used to distribute the error for a specified dot positioning error. In Table 2.4, the result is shown when the dot positioning error standard deviation in both directions is set to 10 μm while the other settings are not changed.

Table 2.4: Dot positioning error Δe in μm for two sets of parameters and variations. Left table: reference printer with parameters $x = 0.1$ m, $y = 0.03$ m, $h = 1$ mm, $v_c = 1.0$ m/s, $v_j = 7.0$ m/s, right table: a change in variations where the total dot positioning error is set to 10 μm in both directions.

reference printer				error budgeted printer			
Δ	1σ	$\sigma\Delta e_1^*$	$\sigma\Delta e_2^*$	Δ	1σ	$\sigma\Delta e_1^*$	$\sigma\Delta e_2^*$
$\Delta\theta_1$	0.02 °	1.50	0.35	$\Delta\theta_1$	0.005 °	0.37	0.09
$\Delta\theta_2$	0.02 °	5.34	0.00	$\Delta\theta_2$	0.005 °	1.33	0.00
$\Delta\theta_3$	0.02 °	10.47	34.91	$\Delta\theta_3$	0.005 °	2.62	8.73
$\Delta\varphi_1$	0.5 °	0.00	8.73	$\Delta\varphi_1$	0.05 °	0.00	0.87
$\Delta\varphi_2$	0.5 °	8.73	0.00	$\Delta\varphi_2$	0.05 °	0.87	0.00
Δr_{c1}	5.0 μm	5.00	0.00	Δr_{c1}	3.4 μm	3.40	0.00
Δr_{c2}	5.0 μm	0.00	5.00	Δr_{c2}	3.4 μm	0.00	3.40
Δr_{c3}	5.0 μm	0.71	0.00	Δr_{c3}	3.4 μm	0.49	0.00
Δr_{n1}	5.0 μm	5.00	0.00	Δr_{n1}	3.4 μm	3.40	0.00
Δr_{n2}	5.0 μm	0.00	5.00	Δr_{n2}	3.4 μm	0.00	3.40
Δr_{n3}	5.0 μm	0.71	0.00	Δr_{n3}	3.4 μm	0.49	0.00
Δv_c	0.03 m/s	4.29	0.00	Δv_c	0.01 m/s	1.43	0.00
Δv_j	0.5 m/s	10.20	0.00	Δv_j	0.1 m/s	2.04	0.00
Δt	2.0 μs	2.00	0.00	Δt	7.8 μs	7.79	0.00
total: ($\ \cdot\ _2$)		19.85	36.67	total: ($\ \cdot\ _2$)		10.00	10.00

While decreasing the dot positioning error standard deviation, at some point, the optimization problem becomes infeasible because too strict tolerances are specified. For the reference printer, a standard deviation of $9 \mu\text{m}$ for the dot positioning error is about the minimum to obtain a feasible solution. For the higher productive printer as depicted in Table 2.2, the dot positioning error standard deviation should be at least $15 \mu\text{m}$ to obtain a feasible solution. The main contribution to $\sigma\Delta e_1^*$ is the jet timing which can be easily reduced via calibration, i.e. position dependent jet timing. This calibration procedure adjusts the jet timing slightly by examining scanned prints. However, position dependent jet timing only removes repetitive errors in \vec{e}_1^P -direction and not in \vec{e}_2^P -direction. In conventional WFPS, $\sigma\Delta e_2^*$ is only determined by manufacturing tolerances. We can conclude that printhead alignment becomes difficult for higher productive WFPS when scaling conventional WFPS. In Chapter 4, concepts are presented which address this printhead alignment problem via active printhead position control in \vec{e}_2^P -direction.

2.6 Conclusions

A systematic method is presented to determine the relation of printer design parameters to the dot positioning error. Via linearization a parametrized relation is obtained giving insight how the sensitivity to manufacturing tolerances changes for varying design parameters. A higher productive WFPS is compared with a reference WFPS in Section 2.4 showing that the printing accuracy deteriorates with a factor of 2.3 when the productivity is increased by a factor of 2. Furthermore, the derived linearized model of the dot positioning error is inverted to use it for error budgeting. Via linear programming the specified variances can be redistributed while keeping the total dot positioning error equal or setting it to a desired value. The method also shows which trade-offs can be made to balance the variations for product design.

Chapter 3

Productivity Analysis of a Wide Format Printing System

In this chapter, the influence of printer design parameters on the printer productivity, defined as the amount of printed surface area per unit of time, is investigated. The presented work in this chapter is based on [5].

3.1 Introduction

Hardly any results have been published on increasing the productivity of WFPS, and to be more specific, increasing the productivity in a cost-efficient way. Most publications are concerned with print quality regarding the jetting mechanism, ink composition and print media. In [85], a productivity model is presented that is targeted at design parameters regarding heat management. Mechanical design parameters are not addressed, as is the focus of this chapter.

Two questions that arise in this respect are:

- (i) How do printer design parameters relate to productivity?
- (ii) Which design parameters should be adjusted for the productivity of a particular printer configuration to be improved?

To be able to answer these questions, a productivity model is developed. Analysis of the productivity model will provide insight into how to choose the design parameters for printers in the development stage regarding the productivity and the productivity-cost ratio.

3.2 Printing Process

To determine the relation between the design parameters of the printer and the productivity, we create a model of the printing process. A schematic overview of the printing process used to derive the productivity model is shown in Figure 3.1.

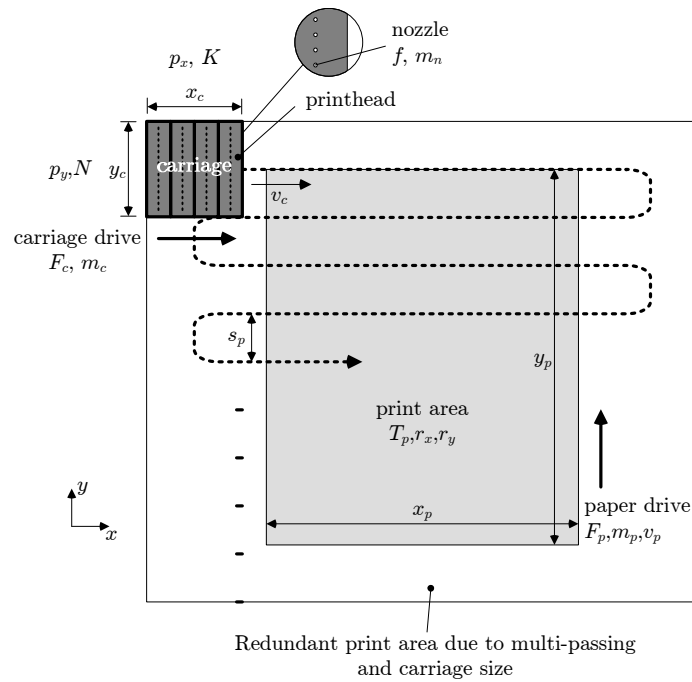


Figure 3.1: A schematic overview of the printing process used to derive a productivity model.

We assume that only one full page is printed and no maintenance is necessary during that print. First, a swath is done which is a movement of the carriage from one side to the other, then it turns simultaneous with the necessary paper translation. This process continues until the whole print area is covered with ink. A list of variable definitions is shown in Table 3.1.

Table 3.1: Variable definitions belonging to Chapter 3.

Var.	Unit	Description
a	[m/s ²]	Acceleration
b	[-]	Binary variable determining whether bidirectional printing is used ($b = 1$) or monodirectional printing ($b = 0$).
C	[€]	Total cost of production of a printing system
c_n	[€]	Cost per nozzle, partial cost of C depending on N
c_r	[€]	Remaining cost not depending on N
D	[-]	Amount of dot locations on the print area
f	[Hz]	Jet frequency, the amount of ink drops a nozzle fires per second
F_c	[N]	Maximum force that the carriage drive can generate
F_p	[N]	Maximum force that the print medium drive can generate
K	[-]	Amount of colors that can be printed in case N nozzles are available for every color
m_c	[kg]	Total mass of the carriage
m_{cr}	[kg]	Remaining carriage (drive) mass independent of N
m_n	[kg]	Mass per nozzle, partial mass of m_c depending on N
m_p	[kg]	Total mass of the print medium
m_{pr}	[kg]	Remaining mass not depending on the print medium mass including the print medium drive mass
N	[-]	Amount of nozzles of each color
P	[1/s]	Productivity, the amount of prints produced per unit of time
P_0	[1/s]	Productivity of an ideal printer (having a printing efficiency equal to 100%, i.e. no efficiency loss due to carriage reversal and print medium transport)
p_x	[-]	Multi-pass in x -direction, amount of swaths necessary to obtain the required resolution in x -direction (see Figure 3.2)
p_y	[-]	Multi-pass in y -direction
r_x	[1/m]	Printing resolution in x -direction
r_y	[1/m]	Printing resolution in y -direction
S	[-]	Amount of swaths required to fill in the whole print area
s_p	[m]	Step-size of the print area after each swath
t	[s]	Time
T_p	[kg/m ²]	Type of paper
Δt_c	[s]	Print time correction due to startup and finalizing of a print job such that the initial/final carriage speed v_c is 0.
Δt_p	[s]	Duration of a print medium step
Δt_s	[s]	Duration of a swath which includes one pass of the carriage, a carriage turn and a paper step
v	m/s	Speed
v_c	m/s	Speed of the carriage during printing
v_p	m/s	Maximum speed of the paper drive
x	[m]	Distance
x_c	[m]	Carriage width
x_p	[m]	Print area width
y_c	[m]	Carriage height
y_p	[m]	Print area height

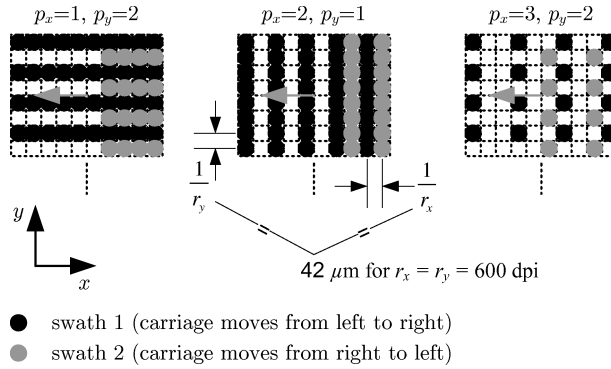


Figure 3.2: Three examples showing the principle of the print strategy "multi-pass". A small area of the print is shown which is being covered with ink. Left figure: multi-pass in y -direction, middle figure: multi-pass in x -direction, right figure: combination of both multi-pass in x -direction and in y -direction. The amount of passes (swaths) required is equal to $p_x \times p_y$ which is 2, 2, and 6 respectively for the given examples.

3.3 Productivity Model

The productivity P_0 of an ideal printer, where all nozzles N jet with jet frequency f without any interruptions such as reversing the carriage, is computed by:

$$P_0 = \frac{fN}{D} \quad (3.1)$$

$$D = r_x x_p r_y y_p \quad (3.2)$$

in which (r_x, r_y) are the printing resolutions and $x_p y_p$ is the print area. The productivity P_0 is the total amount of dots to be placed on the print area. In reality, it is impossible to achieve a productivity P_0 in any printing system because of the nonzero carriage size and the limited actuator power. The carriage width increases the traveling distance of the carriage and the carriage height increases the redundant print area in combination with multi-pass. The limited actuator power results in a nonzero reversal duration. On the basis of Figure 3.1, we can obtain an expression for the productivity P by computing the necessary amount of swaths S , computing the duration of a swath Δt_s and correcting for startup

and finalization Δt_c :

$$P = \frac{1}{\Delta t_s S + \Delta t_c} \quad (3.3)$$

$$\Delta t_c = \frac{2m_c v_c}{F_c} - \max\left(\frac{2m_c v_c}{F_c}, \Delta t_p\right) \quad (3.4)$$

$$\Delta t_s = \frac{x_p + x_c}{v_c} + \max\left(\frac{2m_c v_c}{F_c}, \Delta t_p\right) \quad (3.5)$$

$$S = (2 - b) \left(\text{floor}\left(\frac{y_p}{s_p}\right) + p_x p_y \right) \quad (3.6)$$

$$\Delta t_p = \text{traj}\left(s_p, v_p, \frac{F_p}{m_p}\right) \quad (3.7)$$

$$v_c = \frac{f p_x}{r_x} \quad (3.8)$$

$$m_c = N K m_n + m_{cr} \quad (3.9)$$

$$m_p = T_p x_p y_p + m_{pr} \quad (3.10)$$

$$s_p = \frac{y_c}{p_x p_y} \quad (3.11)$$

$$y_c = \frac{N p_y}{r_y} \quad (3.12)$$

with $t = \text{traj}(x, v, a)$ defined as:

$$t = \begin{cases} \frac{x}{v} + \frac{v}{a} & \text{if } \frac{x}{v} - \frac{v}{a} \geq 0 \\ 2\sqrt{\frac{x}{a}} & \text{if } \frac{x}{v} - \frac{v}{a} < 0 \end{cases} \quad (3.13)$$

which is the duration of a displacement using a second order setpoint. Of course, higher order setpoints can be used in the model as well. (The operator "floor" rounds its argument to the nearest integer towards $-\infty$.)

3.4 Cost Model

In the previous section, we have only considered the productivity, however cost is equally important. This is easily shown by the following reasoning. If the productivity is increased by a factor of 2, the cost of production is not allowed to increase by a higher amount than a factor of 2. If this condition is not satisfied, it would be more cost effective to buy two slower printers instead of one fast printer. We propose the following cost model:

$$C = N K c_n + c_r \quad (3.14)$$

in which N is the amount of nozzles per color, K is the amount of colors, c_n is the cost per nozzle and c_r is the remaining cost not depending on N . Compared to the

productivity model, (3.14) is a highly simplified model. Obviously, the cost model can be adapted to specific configurations and can be more complex, however, we only want to explain the procedure. Only N and K are taken into account and the rest of the parameters are concealed in c_n and c_r . With a model for P and C , the optimal configuration can be determined by searching the maximum of the ratio P/C .

3.5 Print Process Analysis

Productivity Analysis

The productivity model, presented in the previous section, is implemented using Matlab [28]. It contains 18 design parameters which can be chosen independently. The influence of several design parameters is studied and will be discussed next.

Main Productivity Parameters f and N

The two main parameters to increase the productivity are the jet frequency f and the number of nozzles N . In Figure 3.3 the productivity is shown as a function of $f \in [10^3, 10^7]$ Hz and $N \in [10, 1.98 \cdot 10^4]$ where $1.98 \cdot 10^4$ matches with the print medium height y_p . The independent design parameters are chosen as shown in Table 3.2. The other parameters in Table 3.1 depend on these parameters. For this particular configuration, the carriage reversal force F_c is dominant over the maximum force for paper translation F_p , so F_p will not be present in the results.

Table 3.2: Independent design parameters

f	$\in [10^3, 10^7]$ Hz	N	$\in [10, 1.98 \cdot 10^4]$
x_p	= 0.84 m (= A0 width)	p_x	= 1 (no multi-pass in x)
y_p	= 1.188 m (= A0 height)	p_y	= 1 (no multi-pass in y)
v_p	= 1 m/s	b	= 1 (bidirectional printing)
F_p	= 100 N	K	= 1 (single color)
T_p	= 0.1 kg/m ²	m_n	= 2 g
m_{pr}	= 0.5 kg	m_{cr}	= 1 kg
r_x	= $2.36 \cdot 10^4$ 1/m (= 600 dpi)	F_c	= 100 N
r_y	= $2.36 \cdot 10^4$ 1/m (= 600 dpi)	x_c	= 0.1 m

If we substitute (3.4) to (3.12) into (3.3) assuming $\frac{x_p+x_c}{v_c} \gg \frac{2m_c v_c}{F_c}$ (printing duration \gg reversal duration) we obtain:

$$P = \frac{fN}{(x_p + x_c)(y_p + y_c)r_x r_y} \quad (3.15)$$

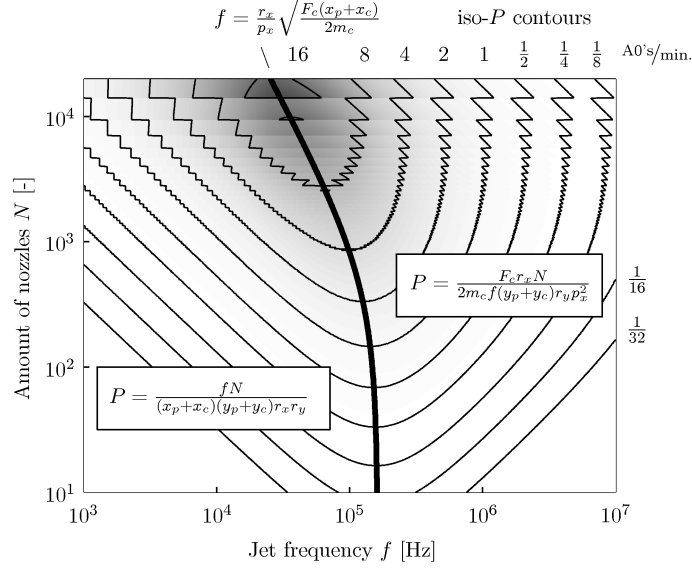


Figure 3.3: Iso-Productivity (Iso- P) contours in $A0's/min.$ as a function of the jet frequency f and the amount of nozzles N . Two areas are shown with an approximation of the productivity for each area. In the left area, the printing duration is dominant (printing efficiency $> 50\%$), and in the right area, the reversal duration is dominant.

which is an approximation for the productivity at the left side of the black line in Figure 3.3. For $\frac{x_p+x_c}{v_c} \ll \frac{2m_c v_c}{F_c}$ (printing duration \ll reversal duration) we obtain:

$$P = \frac{F_c r_x N}{2m_c f (y_p + y_c) r_y p_x^2} \quad (3.16)$$

which is an approximation for the productivity at the right side of the black line. The floor-operator is also neglected, it only produces the sawteeth shaped iso- P contours for high nozzle amounts visible in Figure 3.3. Comparing (3.15) to (3.1), the productivity P approximates P_0 for low jet frequencies resulting in a high printing efficiency, i.e. the printing duration is dominant over the reversal duration. If the reversal duration becomes dominant, the approximation of the productivity (3.16) applies. Important observations from this equation are: the productivity drops with increasing f , the productivity drops with p_x^2 , the productivity depends on the ratio r_x/r_y representing an asymmetric print raster.

The cross section of the two approximations (3.15) and (3.16) is the separation between the two areas where the printing duration and the reversal duration are equally dominant:

$$f = \frac{r_x}{p_x} \sqrt{\frac{F_c (x_p + x_c)}{2m_c}} \quad (3.17)$$

For a higher productive WFPS, we want the printing duration to be dominant otherwise too much efficiency is lost. The point (f, N) must approach the border (3.17) in Figure 3.3 when increasing productivity, so we have to aim at:

- (i) increasing the actuator force F_c ,
- (ii) decreasing the carriage mass m_c ,
- (iii) avoiding the use of multi-pass in x -direction, and
- (iv) increasing the printing resolution in x -direction r_x ,

to avoid too much efficiency loss. The carriage width x_c could be increased to shift the border, however the printing efficiency gain is deteriorated by a productivity decrease as shown by (3.15).

Carriage Width x_c and Height y_c

The carriage height can cause redundant carriage movement area which is the area around the print area where the carriage must pass while printing onto the print medium. The size of this redundant area depends both on the amount of multi-passes and the carriage height relative to the print area height. The redundant area is decreased by:

- (i) decreasing the amount of multi-passes in x -direction and y -direction,
- (ii) choosing y_c such that y_p/y_c is an integer, and
- (iii) it is possible to start with the next print when the current print is not finished yet. This will overcome the problem of redundant area at the top and bottom of the print area.

On the other hand, x_c increases the swath length $x_p + x_c$, which can not be avoided in any way, causing redundant print area on the left and right side of the print area instead of on the top and bottom of the print area. To conclude, staggering printheads in y -direction is preferred over staggering in x -direction.

Multi-pass p_x and p_y

The use of multi-pass in x -direction needs to be avoided for higher productive systems, because the carriage speed increases by a factor p_x and the amount of dots printed per swath decreases by a factor p_x . So, if the reversal duration approaches the printing duration, multi-pass in x -direction dramatically reduces the productivity. On the other hand, p_y is less of a problem, as it can only cause extra redundant carriage movement area in combination with the carriage height y_c , as previously mentioned. Therefore, multi-pass in y -direction is preferred over multi-pass in x -direction. The only advantage of multi-pass in x -direction is that it increases reliability by camouflaging nozzle failures because every line is built up by several nozzles.

Productivity/Cost Analysis

A way to include cost of production in the consideration of which configuration to choose is to divide the productivity (3.3) by the cost (3.14). In this simple example of the cost model we made the cost linear-dependent on the amount of nozzles, $c_n = \text{€ } 2$, plus a constant value for all other cost, $c_r = \text{€ } 10000$. The result of P/C is shown in Figure 3.4. We see an optimum emerge which can be seen as the optimum choice of f and N in terms of productivity and cost of production. However, this optimum depends on a lot of design parameters, and is thus only valid for this particular example.

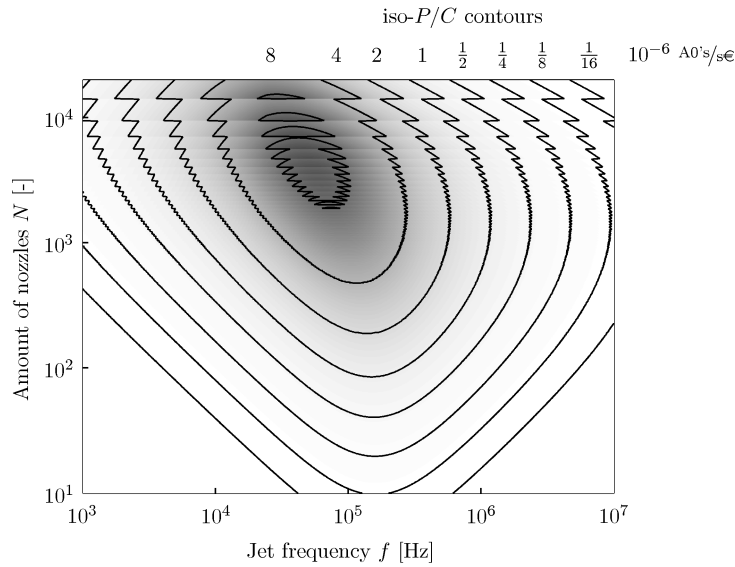


Figure 3.4: Iso- P/C contours in 10^{-6} A0's/s€

3.6 Conclusions

Both a productivity and a cost model for scanning inkjet printing systems have been proposed. These models provide insight in how the productivity and cost depend on the design parameters of a printer configuration:

- (i) A higher jet frequency can result in a lower productivity.
- (ii) x_c and y_c should be minimized regarding productivity however increasing y_c is less problematic than increasing x_c .
- (iii) Using asymmetric rasters (increasing r_x/r_y) results in a higher productivity for higher productive WFPS.
- (iv) Multi-pass in x -direction decreases the productivity dramatically.

Chapter 4

Concept Exploration

In the previous chapters, the influence of printhead design parameters and tolerances on productivity and printing accuracy has been investigated. An important conclusion is that a higher productivity deteriorates both printing accuracy and printing efficiency with the existing designs. In this chapter, an exploration of concepts other than scaling conventional WFPS is done. A concept exploration of alternatives to scaling conventional WFPS is given following the design methodology as presented in Section 1.4.

4.1 Concepts for Improving Printing Accuracy

For WFPS the printing resolution is typically 600 dpi resulting in a pitch of $42\ \mu\text{m}$. A dot positioning accuracy of $10\ \mu\text{m}$ is required to obtain a desired print quality as determined from visual inspection of printed samples. The dot positioning accuracy is defined as the positioning accuracy of a dot relative to the dots in its neighborhood. As an example, suppose that all dots on a print are shifted by 1 mm in the same direction, then this would not deteriorate print quality, hence, absolute dot positioning accuracy is not required to obtain acceptable print quality.

Maintaining or improving print quality is the main target for higher productive WFPS. Print quality is a subjective assessment by a human of how good a printed image looks. Unfortunately, due to the subjective nature, a systematic way to assess a printed image does not exist. However, individual properties that have an effect on the print quality can be measured, such as: printing accuracy,

color density variations, image noise level, color banding, printing resolution, ink composition, print medium composition, print solidity, environmental conditions, human perception, nominal viewing distance, lightning conditions, etc..

Printing accuracy has the most influence on print quality because many properties are correlated with printing accuracy such as color density variations, image noise level, and color banding. Therefore, our main focus lies on improving printing accuracy. When keeping existing designs, manufacturing tolerances have to be tightened to improve the printing accuracy. This makes the design more expensive. In the next sections, concepts are described which are an alternative to tightening manufacturing tolerances.

4.1.1 Control of the Carriage-Print Medium Distance

Table 2.1 showed that an increase of the nozzle-paper distance h results in a sensitivity increase to the variations $\Delta\theta_2$ and $\Delta\varphi_2$ in paper translation direction and to the variations $\Delta\theta_1$, $\Delta\varphi_1$, Δv_c , and Δv_j in carriage translation direction. The nozzle-paper distance amplifies these variations' sensitivity because the ink droplets have to travel over a larger distance. In Figure 4.1, the variation of the nozzle-paper distance for an arbitrary location of the carriage $h(x, y)$ is shown.

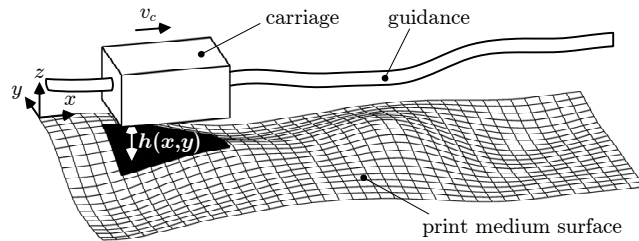


Figure 4.1: Position dependent nozzle-paper distance variations deteriorate printing accuracy.

Print medium surface variations and guidance height variations are both in the order of $100 \mu\text{m}$. Because the carriage may never touch the print medium surface during the whole lifetime of WFPS, a safe minimum nozzle-paper distance of about 1 mm is chosen for conventional WFPS.

By measuring and controlling the DOF's z , φ_x , and φ_y of the carriage, the nominal nozzle-paper distance can be reduced to about $200 \mu\text{m}$ which decreases the sensitivity to variations depending on h as shown in Table 2.1 by a factor 5. Furthermore, the variation Δh can also be decreased. For this concept, multi-variable control of the carriage has been investigated in [55] and has shown to be feasible. Elaboration on this work asks for a carriage suspension design and a non-contact, low-cost sensor design which measures the nozzle-paper distance.

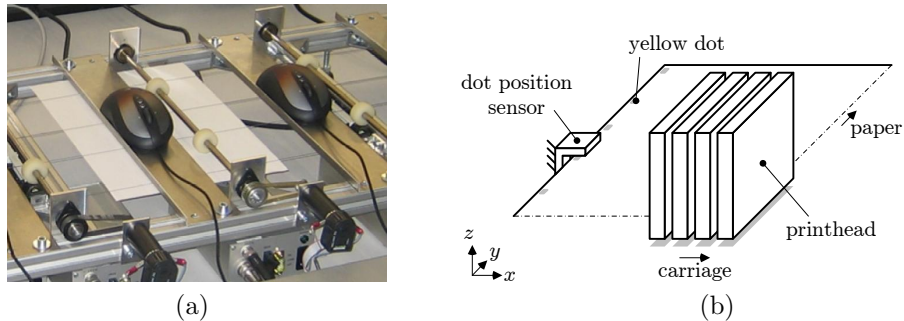


Figure 4.2: (a): paper position measurement via an optical mouse sensor (picture from [13]), (b): marker based paper displacement

4.1.2 Direct Paper Translation Measurement

After each swath of the carriage, the paper shifts over a specified distance. This has to be done in short time because after the carriage has reversed the paper should have translated accurately. The displacement in conventional WFPS is estimated using encoder information from the paper drive. Paper positioning accuracy is deteriorated due to:

- (i) the presence of coulomb friction while shifting the paper,
- (ii) parasitic dynamics due to reversal of the carriage, and
- (iii) time-variant behavior of the paper.

By directly measuring the displacement of the paper with an accurate sensor, paper positioning accuracy can be improved. The displacement error can be controlled by both the paper drive or an extra motor adjusting the carriage position in paper transport direction. Possible sensors are an optical mouse sensor, as is also used for paper feedback control in [13], or printing a marker on the side of the paper (e.g. a yellow dot) and measuring it using an image sensor as shown in Figure 4.2.

4.1.3 Carriage Reversal Vibration Suppression

In conventional WFPS, the reaction force onto the printer frame caused by reversing the carriage results in parasitic dynamics. The low frequency oscillation of the printer frame is not directly a problem for the printing accuracy regarding carriage positioning because jetting is done position dependent using a linear encoder. A linear encoder consists of a strip with equally spaced slits which are detected via a LED and a light sensitive sensor. This strip is stiffly connected to the printer frame so position based jet timing is accurate with respect to the printer frame where the paper is lying on. The paper is kept still at the printer frame by Coulomb friction during printing. However, during carriage reversal,

the paper shifts. While shifting the paper, it can easily shift sideways because the Coulomb friction coefficient is equal in x and y direction. Due to the parasitic dynamics of the printer frame induced by reversing the carriage, sideway shifting can occur resulting in misalignment of the paper with respect to the previous swath, hence print accuracy is deteriorated. Moreover, multipass printing (see Figure 3.2) is commonly used to obtain the desired print resolution. Misalignment of two swaths of $10\ \mu\text{m}$ results in light density variations which are well visible. The dots are simply printed partly on top of each other leaving more unprinted area on the print medium surface as shown in Figure 4.3.

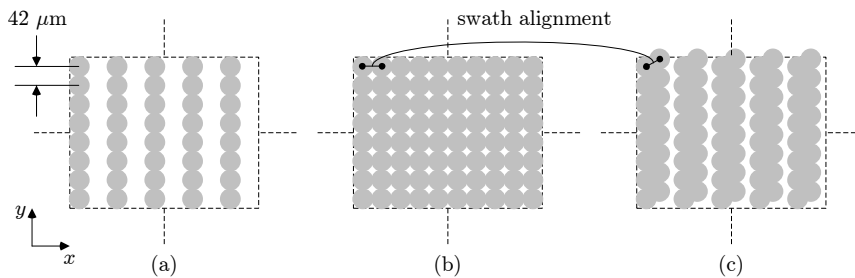


Figure 4.3: Part of the printed image. Two swaths are used to obtain the full resolution of 600×600 dpi, (a) swath 1: resolution 300×600 dpi (b) swath 2: no swath misalignment (c) swath 2: swath misalignment resulting in a lighter average color.

As a solution to this, the effects of the reaction force caused by reversing the carriage can be minimized by counteracting this force by another mass moving in the opposite direction. Possible concepts are:

- (i) pushing against another freely translating mass during carriage reversal. This concept can be implemented using a much heavier contra mass compared to the carriage, e.g. a factor 10 larger results in a factor 10 lower speed for the large balance mass,
- (ii) attaching a balance mass on the other side of the belt, see Figure 4.4. This concept doubles the required drive power. A possibility is to add printheads to the balance mass resulting in two identical carriages moving in opposite direction. The challenge is then to accurately align the printheads of both carriages.

4.1.4 Active Printhead Alignment

For higher productive WFPS, x , y , and v_c are larger resulting in a worse printing accuracy (see Table 2.1). Especially rotation $\Delta\theta_3$ around the z -axis of the carriage is increased as shown in Table 2.2. This variation has a large influence on the printing accuracy in paper transport direction.

A commonly used method is to adjust jet-timing of all nozzles which can be

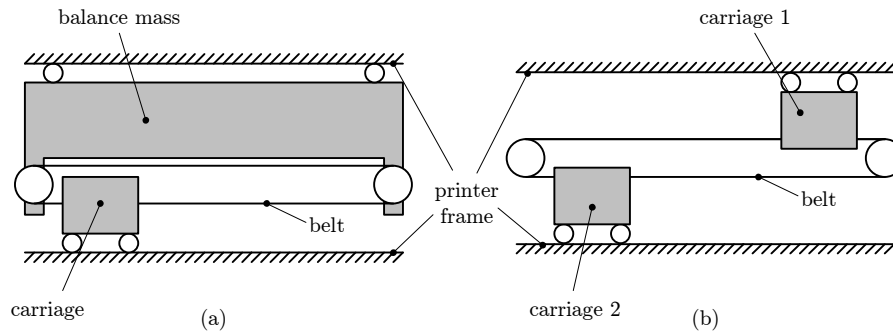


Figure 4.4: (a): concept including a balance mass to prevent oscillations of the printer frame, (b): concept with two carriages connected to the same belt moving in opposite directions

perfectly calibrated by printing patterns, scanning the print and extracting jet-timing corrections from the scanned image, see e.g. [25, 31]. However, mutual printhead alignment can not be compensated for with subpixel accuracy by jet-timing calibration, only shifting of the image with pixel resolution is possible. Subpixel accuracy is defined as an accuracy being higher than the pitch of the printed dots on the paper. The described jet timing calibration procedure can not provide subpixel printhead alignment accuracy.

The nozzles are 'connected' to the paper via a long path: nozzles \rightarrow printhead \rightarrow carriage \rightarrow guidance \rightarrow printer frame \rightarrow paper. In conventional designs, the entire path has to be made very accurate to prevent unacceptable misalignments of the fixed printheads. With increasing performance requirements for the print quality and productivity, the amount of printheads will increase and the printhead alignment accuracy requirements will increase. Both aspects will dramatically complicate printhead alignment. Solving the alignment problem using tight manufacturing tolerances is expensive and is therefore not preferred. To be able to regulate the printhead misalignment caused by the whole path between nozzle and paper, we search for a solution in the mechatronic domain.

Often, calibration tools are used for aligning printheads during assembly. This method can compensate for static errors in the printhead and carriage; misalignment due to e.g. guidance inaccuracies, thermal variations and parasitic dynamics are not dealt with. As an example in [16], a printhead alignment procedure for WFPS is proposed, however, the proposed method only aligns the printheads with respect to the carriage. Manufacturing tolerances and vibrations of the guidance can not be compensated for.

In the reported work [40, 66], a 2-stage alignment method is shown using a charge-coupled device (CCD) sensor for coarse alignment and an electrostatic actuator to bend the trajectory of the ink drops for fine alignment. Although a precision of $2 \mu\text{m}$ can be obtained with this method, practical printing speeds can not be

achieved due to the CCD-video system limitations.

As an alternative, the alignment error can be regulated with respect to a reference which is 'connected' to the print medium surface. This can be done for the carriage (see Figure 4.5(a)) or even for each printhead separately (see Figure 4.5(b)). The latter can provide a printhead alignment accuracy close to the sensor accuracy while manufacturing tolerances can be loosened because these imperfections are measured and regulated. This concept has the potential to be an order more accurate than what is achieved with manufacturing tolerances in conventional WFPS.

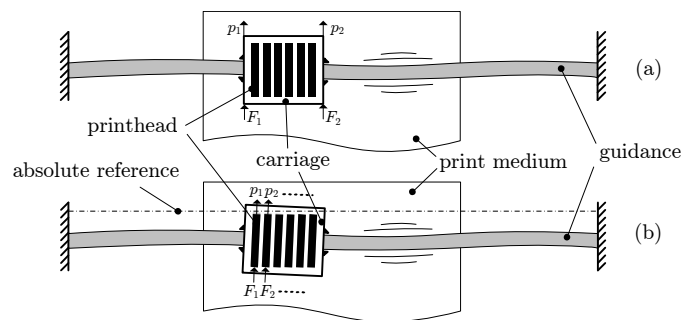


Figure 4.5: Active printhead alignment concept. (a): alignment of the carriage relative to the printer frame, (b): alignment of each printhead with respect to the printer frame.

Another feature which is possible with this concept is to add a redundant printhead which can take over the task of another printhead with temporarily malfunctioning nozzles resulting in a higher robustness to this problem. This concept also enables the concept of more than one carriages in a printer as shown in Figure 4.4(b) because the alignment error is measured with respect to the printer frame for all carriages or printheads.

When considering the improvement of printhead alignment to obtain a better print quality, the concept of actively aligning all printheads individually is the most promising and will be investigated. The concept will be presented in Part II. Challenges are to design a short stroke actuator and sensor being low-cost and robust for a temperature varying environment. An experimental setup has been built to determine the feasibility of the concept.

4.2 Concepts for Improving Printing Efficiency

Printing efficiency decreases for higher productive WFPS due to an increase of carriage dimensions and reversal time as shown in Chapter 3. The following two concepts address this decrease in printing efficiency.

4.2.1 Printhead Staggering in y -Direction

Staggering of printheads in paper transport direction is preferred above staggering of printheads in carriage movement direction because the width of the carriage decreases as concluded in Chapter 3. An additional advantage to this is that the guidance can become shorter such that the carriage mounting becomes more stiff and WFPS become more compact. A comparison of staggering printheads in both directions is shown in Figure 4.6. It is estimated that a printing efficiency gain of 10%-20% can be obtained, however, printhead alignment becomes more difficult requiring an active control solution as described in Section 4.1.4.

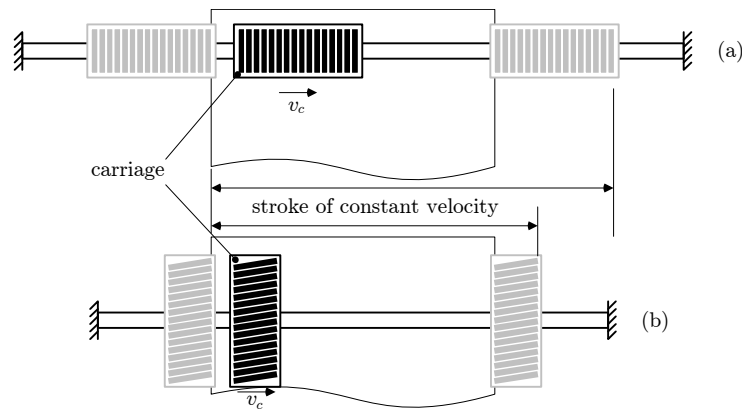


Figure 4.6: Staggering concepts of 16 printheads, (a) printhead staggering in carriage movement direction. (b) printhead staggering in paper transport direction.

4.2.2 Energy Buffered Reversal

Another way to improve printing efficiency is by reducing the reversal time. For higher productive WFPS this is required, else it can occur that much time is used for reversing the carriage instead of printing. This could be done by scaling the drive in conventional WFPS, which, however, is expensive. An alternative is to use an energy buffer to store the kinetic energy of the carriage and return it such that the carriage moves in the other direction, e.g. by using a spring or a magnet. An example of such a concept is shown in Figure 4.7.

Printing occurs when the carriage moves across the paper with a constant speed, while the clutch is not engaged. If printing is ready for that particular swath, the carriage has to be reversed. In conventional printers this is done by using an electromotor. In the concept shown in Figure 4.7, a clutch is engaged such that a spring is connected to the carriage via a belt. The carriage slows down while it stores kinetic energy into the spring. After that, it accelerates again due to the tensioned spring until the carriage is reversed. Then, the carriage moves with a constant speed in the other direction to print the next swath.

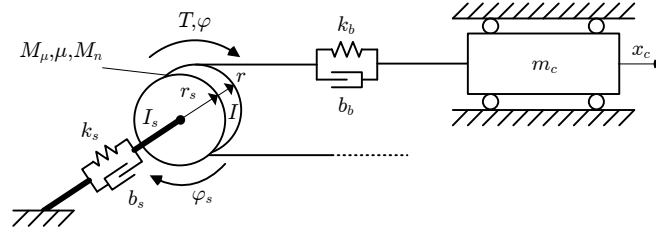


Figure 4.7: Model of a drive assistance where a clutch connects a spring to the drive during carriage reversal.

Advantages are that this concept is easily scalable and it requires only a small additional motor to compensate for friction acting on the carriage to keep it at a constant speed. The brute reversal force will be delivered by the spring and not by the electromotor as is the case for conventional WFPS. To obtain a shorter reversal time, the stiffness of the energy buffer can be simply increased. This concept will be investigated because it is easily scalable for higher productive WFPS compared to scaling existing designs. In Part III, this concept will be presented. An experimental setup has been built to determine the feasibility of the concept.

Part II

Active Printhead Alignment

Chapter 5

Printhead Position Sensor

This chapter is based on [6] and describes the design of a low-cost printhead position sensor to be used for active printhead alignment. A string is tensioned along the guidance, serving as an absolute alignment reference. By using an optical non-contact sensor the printhead position can be measured accurately with respect to the printer frame while being robust for parasitic dynamics and thermal variations.

5.1 Introduction

To obtain a good printing accuracy, printheads have to be aligned:

- (i) mutually,
- (ii) relative to the print medium, and
- (iii) relative to previous swaths.

When increasing productivity, tightening of the manufacturing tolerances becomes more difficult and expensive as explained in Chapter 2. At some point, innovative alternative designs become lucrative to achieve the required print quality.

The method presented in this chapter does not depend on tight manufacturing tolerances to obtain a good printing accuracy. The alignment error of all printheads is measured and actively controlled. Dot positioning errors in the carriage movement direction can be compensated for by regulating the jet timing with sub-resolution accuracy. However, in the paper transport direction, jet timing can not compensate for dot positioning errors. A low-cost short stroke actuator

and sensor has been developed to enable regulation of the printhead misalignment in paper transport direction.

In this chapter, we present the design of the printhead position sensor. From experience, a maximum misalignment of printheads relative to each other of 10 μm is considered to be the required specification for accurate printing which follows from experience. Because other sources such as thermal drift and servo errors determine the printhead alignment accuracy, we aim at a sensor accuracy of about 1 μm . The sensor should measure the printhead position with respect to an absolute reference along the guidance which is in the order of 1 m long as shown in Figure 4.5. An absolute reference is defined as a reference where all printheads will be aligned to. The operating environment temperature range is in the range of 10 °C to about 50 °C. The sensor should be compact, cheap and non-contact to establish a lucrative printhead regulation device.

5.2 A String as an Absolute Reference

Measuring and regulating the position of each nozzle individually is infeasible because this would require 1000s of sensor-actuator systems. If only the position of the carriage is measured, then we can only compensate for errors caused by the carriage guidance. Hence, measuring the position of each printhead is the most logical choice. This can be done relative to each other, however, carriage guidance errors are not included then, which have a large contribution to the printing accuracy. From this reasoning we can conclude that we want to develop an absolute position measurement and regulation for each printhead with respect to the printer frame where the paper lies on.

Considering the required accuracy of 1 μm , we need a reference with a non-repetitive straightness of at most 1 μm . Straightness is defined as the deviation in the orthogonal directions when moving along the reference. An obvious choice would be to place a laser beam parallel to the guidance and align the printheads by measuring the location of the laser with an optical sensor. Unfortunately, this approach is not feasible for the given application because the laser beam will refract due to air density variations caused by thermal variations of the air which are present because the printheads contain ink with a temperature of 130°C.

The proposed solution to obtain an absolute reference which is robust to thermal variations is a tensioned string in parallel with the guidance and to measure the printhead position with respect to this string. An overview of this concept is shown in Figure 5.1. Each printhead is equipped with a sensor that measures the position of the string and a short stroke actuation mechanism that provides misalignment regulation. Because the string is tensioned, only relatively high string harmonics are present above 200 Hz, analogous to a guitar string. These harmonics can be filtered such that alignment errors with frequency content below the first string harmonic can be compensated for. Temperature variations

will cause only little drift of the harmonic frequencies. By designing the filter which removes the harmonics robust for this drift, an absolute reference without vibrations is obtained under temperature variations.

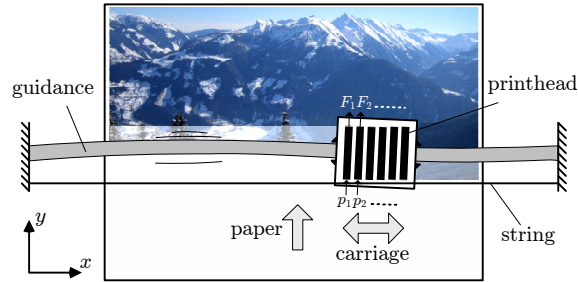


Figure 5.1: Active printhead alignment for WFPS where a string is used as an absolute reference.

5.3 Alignment Sensor Design

In this section, we describe the design of a string position sensor composed of a charge coupled device (CCD) sensor and two light emitting diodes (LEDs) which has been chosen to be used for the experimental setup because it is low-cost, accurate enough and it provides freedom of choice for the string's material. Other alignment sensor principles which have been investigated are described in Appendix B including magnetic, inductive and other optical sensors.

The developed sensor, consisting of a CCD and two LEDs, measures two shadow positions of the string, see Figure 5.2. These shadows enable a triangular measurement resulting in an accurate position reconstruction of the string. A similar approach is used in [74] for edge detection of a paper. Two LEDs are used because a shadow position can be determined much more accurate than a shadow width, which would have to be measured when only a single LED would be used.

The developed sensor is actually a 2D sensor, however, for this application only a 1D sensor is required. If two sensors are placed onto the same rigid body, a 4D sensor is obtained which can measure the rigid body's position in four dimensions relative to a string which can be of interest for other applications.

5.3.1 Sensor Dimensioning

The size of the sensor should be minimized because space in the carriage is limited and for each printhead a sensor has to be added. Therefore, we could minimize h_l or $h_l w_l$ (see Figure 5.2) while satisfying constraints on the LED distance w_l , the

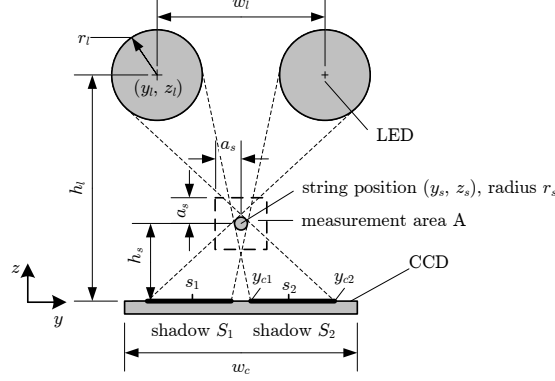


Figure 5.2: The optical sensor contains two LEDs and a CCD array of 128 pixels with a resolution of 400 dpi (TAOS TSL1401R). Two shadows are detected by the CCD when the LEDs emit light. These shadow positions are mapped to the string position.

LED radius r_l , the LED height h_l , the string height h_s , the measurement range a_s , the string radius r_s and the CCD width w_c which are indicated in Figure 5.2. We can divide the constraints in geometric constraints and shadow constraints:

- *geometric constraints*: all objects may never hit each other:

$$w_l > 2r_l \quad (5.1a)$$

$$h_l > h_s + a_s + r_s + r_l \quad (5.1b)$$

$$h_s > a_s + r_s \quad (5.1c)$$

- *shadow constraints*: both shadows may not overlap and should fall completely onto the CCD for all string position $(y_s, z_s) \in A$, see (5.2) and Figure 5.2:

$$\{S_1 \cap S_2 = \emptyset; S_1, S_2 \subset C\} \quad \forall (y_s, z_s) \in A \quad (5.2)$$

where C is the CCD surface. The intersection point y_{ci} at the CCD of a tangent line of two circles, a LED at position (y_l, z_l) and a string at position (y_s, z_s) , can be computed as follows:

$$y_{ci} = y_s + \frac{z_s d + \sigma_s^i r_s}{c} \quad (5.3)$$

$$c = \frac{(z_l - z_s)b - (y_l - y_s)(\sigma_l^i r_l - \sigma_s^i r_s)}{a}$$

$$d = \frac{-(y_l - y_s)b - (z_l - z_s)(\sigma_l^i r_l - \sigma_s^i r_s)}{a}$$

$$a = (z_l - z_s)^2 + (y_l - y_s)^2, b = \sqrt{a - (\sigma_l^i r_l - \sigma_s^i r_s)^2}$$

with auxiliary variables $\sigma_s^1 = \sigma_l^1 = 1$ and $\sigma_s^2 = \sigma_l^2 = -1$.

The constraints above are nonlinear inequalities. A genetic algorithm [38] implemented by the Genetic Algorithm and Direct Search Toolbox of Matlab [62] is used to solve the problem:

$$\min_x f(x), \quad x \subseteq X \quad (5.4)$$

where

$$f(x) = h_l^2 + N_c(x) \cdot 10^{10} \quad (5.5)$$

with parameter set $x = \{w_l, r_l, h_l, h_s, a_s, r_s, w_c\}$, X the parameter space and $N_c(x)$ the amount of inequalities that are not satisfied. For our prototype, we predefine the parameters of x for some available construction parts: $r_l = 1.5$ mm, $r_s = 0.25$ mm, $w_c = 8$ mm. Furthermore, the maximum amplitude of the string is a summation of the vibration amplitude and the desired measurement range. The desired measurement range in the application is about 300 μm which includes all tolerances from the carriage guidance to the sensor mounted onto the printhead. Furthermore, an upper bound of the vibration amplitude is estimated at 300 μm . Added together, the required total measurement distance a_s becomes 0.6 mm. Optimization of (5.4) results in: $w_l = 6.1$ mm, $h_l = 7.9$ mm, $h_s = 1.9$ mm

5.3.2 Sensor Setup

The string position is measured by using 2 light emitting diodes (LEDs) and a CCD sensor (TAOS TSL1401R 128x1 linear sensor array with hold). The string position can be determined by means of optical triangulation which is a proven concept to obtain an accurate position measurement, see [18, 51, 74].

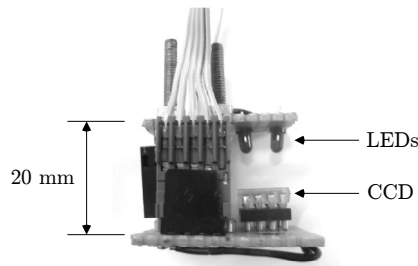


Figure 5.3: First sensor prototype with two LEDs and a CCD.

The first sensor prototype is shown in Figure 5.3. A TMS320F2812 DSP is used for driving the TAOS TSL1401R CCD sensor and processing the sensor signal. A

typical shadow image is shown in Figure 5.4. The shadow image is contaminated with white noise coming from the electrical circuitry of the CCD. The resolution is 400 ppi, equal to a pitch of $63.5 \mu\text{m}$. To obtain a subpixel accuracy of $1 \mu\text{m}$, interpolation is required [22, 51] instead of simply using the two peak locations.

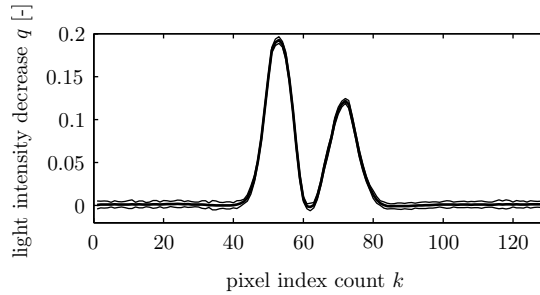


Figure 5.4: Typical shadow image captured by the CCD sensor. The mean values of 1000 samples measured at a sampling rate of 2 kHz are shown together with the $\pm 2\sigma$ bounds.

A schematic view of the sensor used in the experiments presented in Chapter 7 is shown in Figure 5.5. To make the sensor insensitive to ambient light, most sides are covered and the inner surface is painted matt black. For the experimental setup these measures have shown to be sufficient. Alternative methods to become more robust to light disturbances are light modulation and covering the CCD sensor with an optical band-pass filter.

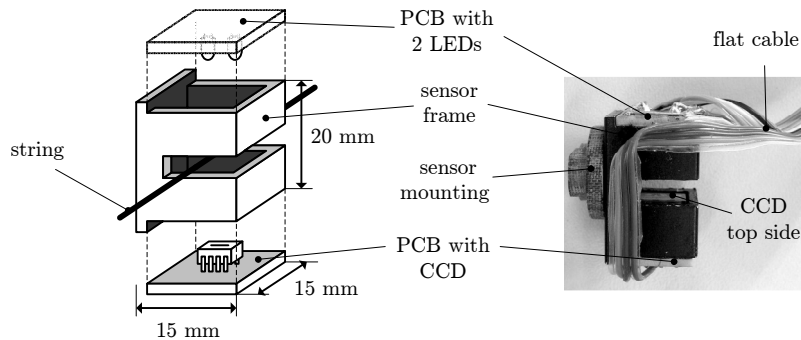


Figure 5.5: Schematic view and picture of the string position sensor which is used in the experiments presented in Chapter 7.

5.3.3 Shadow Center Determination

The challenge is to estimate an unbiased measure of the shadow center with a low variance in time. A second requirement is that the algorithm should be not too complex due to the targeted sampling rate in the order of 10^3 Hz which is

common for motion systems. A number of curve-fitting and non-curve fitting methods are compared in [22], however these algorithm are not suitable for our application because they are either not accurate enough or too complex. Below, two peak estimation algorithms are presented which have been designed and are suitable for our application: the split area algorithm and the extended weighted average algorithm.

Split Area Algorithm

The **Split area algorithm** splits the area above the threshold value hq_{p_i} into two equal parts as shown in Figure 5.6. p_i is the pixel position with the largest light intensity decrease q and s_i represents the shadow center of peak i in the pixel domain where $i \in \{1, 2\}$ is the peak index. We make the sampled data continuous in the pixel domain using a first order interpolation:

$$q(y) = (y - k)q_{k+1} + (k + 1 - y)q_k \quad (5.6)$$

where $y \in C$ is the continuous location on the surface of the image area C , and $k = \text{floor}(y)$ which rounds y to the nearest integer towards minus infinity. The selected shadow $E \subset C$ is defined as the closed subset:

$$E := \{p_i, y \in E \mid q(y) \geq hq_{p_i}\} \quad (5.7)$$

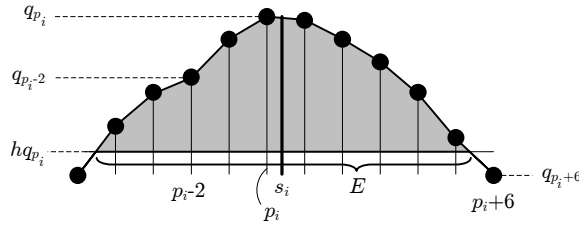


Figure 5.6: Visualization of the split area algorithm.

From splitting the surface area we obtain the shadow center-of-area from:

$$s_i \in E : \int_{y \leq s_i} (q(y) - hq_{p_i}) dy = \int_{y > s_i} (q(y) - hq_{p_i}) dy \quad (5.8)$$

The standard deviation $\sqrt{E\{(s_i - E\{s_i\})^2\}}$ lies within 0.4 to 1.5 μm for each position in the measurement area A as measured in experiments. This standard deviation will vary with position: if the string is close to the CCD and has the same y position than a LED resulting in a high peak, then the standard deviation is about 0.5 μm . In Figure 5.7 two shadow center estimations are shown for the 1000 samples shown in Figure 5.4. The estimation error is a broadband noise signal. The standard deviations are 0.45 μm and 0.78 μm respectively.

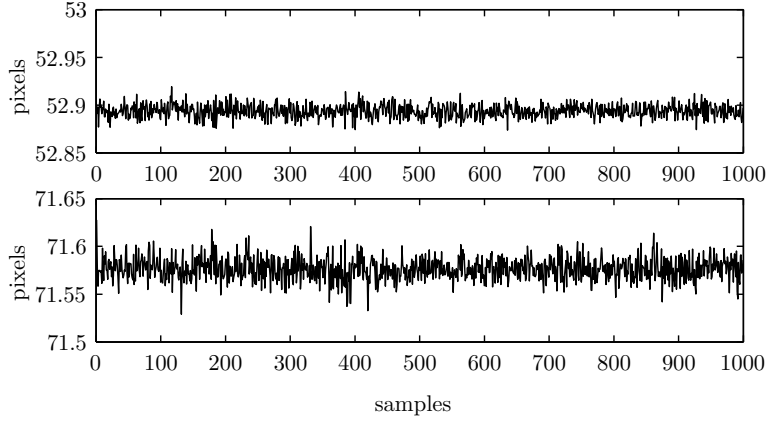


Figure 5.7: Shadow center estimation of two shadows with standard deviations of 0.0071 and 0.0123 pixels corresponding to 0.45 and 0.78 μm respectively.

Extended Weighted Average Algorithm

Experiments showed that the split area algorithm was too computationally expensive for the hardware-platform used so a more efficient algorithm was developed inspired by the same algorithm in combination with the weighted average method. An illustration is shown in Figure 5.8.

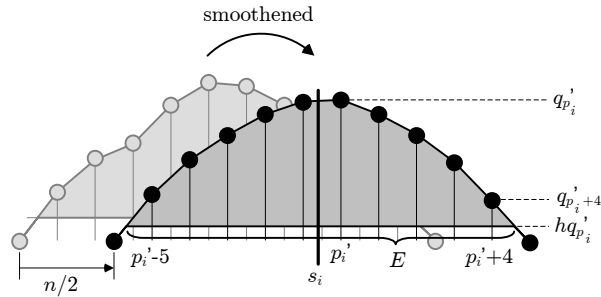


Figure 5.8: Visualisation of the extended weighted average algorithm.

The raw image data \underline{q} is smoothed using a recursive n -point moving average method:

$$q'_k = \sum_{i=k-n+1}^k q_k, \quad k = n, \dots, 128 \quad (5.9)$$

$n = 5$ is used for implementation and the CCD contains 128 pixels. Due to this algorithm all shadow peaks shift by $n/2$ which does not matter because it does

Table 5.1: A comparison between peak estimation algorithms to compute the peak center for peaks of width m . The data from Figure 5.4 is used to compute the standard deviation of both peaks.

	floating point multipli- cations/divisions	standard deviations for peak 1 and peak 2
split area algorithm	$3m + 6$	$0.45 \mu\text{m}, 0.78 \mu\text{m}$
extended weighted average algorithm	$m + 1$	$0.43 \mu\text{m}, 0.81 \mu\text{m}$

not influence the standard deviation of the peak estimates p'_1 and p'_2 . Smoothing decreases the variance of the position measurement.

Define the closed subset $E \subset [n, 128]$:

$$E := \{k, p'_i \in E \mid q'_k \geq hq'_{p'_i}\} \quad (5.10)$$

where h is a fraction of the peak amplitude ($h = 0.5$ is used for implementation). The final peak position estimate p'_i becomes:

$$p'_i = \frac{\sum_{k \in E} k(q'_k - hq'_{p'_i})}{\sum_{k \in E} (q'_k - hq'_{p'_i})} \quad (5.11)$$

An essential property of the extended weighted average algorithm is that the addition of a pixel with a value near $hq'_{p'_i}$ will not cause a discontinuity if it is just below or just above $hq'_{p'_i}$. If a normal weighted average method would be used, leaving out $hq'_{p'_i}$ in (5.11) would result in a discontinuity causing a dramatic increase of the position estimation variance. The algorithm above is implemented on a TMS320F2812 DSP with a sampling rate of 5 kHz, where the split area algorithm only reached 2 kHz. The obtained variance with the new algorithm remains about the same. In Table 5.1, some properties are shown of both algorithms. The data is also smoothed for the split area algorithm to obtain a fair comparison.

5.3.4 Calibration Procedure

We want to determine a unique mapping $\{s_1, s_2\} \rightarrow \{y_s, z_s\}$. A parametric model will not be accurate enough because the light composition at the CCD array is quite complex, including LED geometry, reflections and light refraction. However, the total light composition will be constant if the geometry and the surroundings of the sensor are kept the same. Hence, we can determine a unique mapping which can be captured in a calibration table.

To obtain this mapping, we first move the string at predefined positions (measurement grid) denoted by the crosses in Figure 5.9(b). The string position is

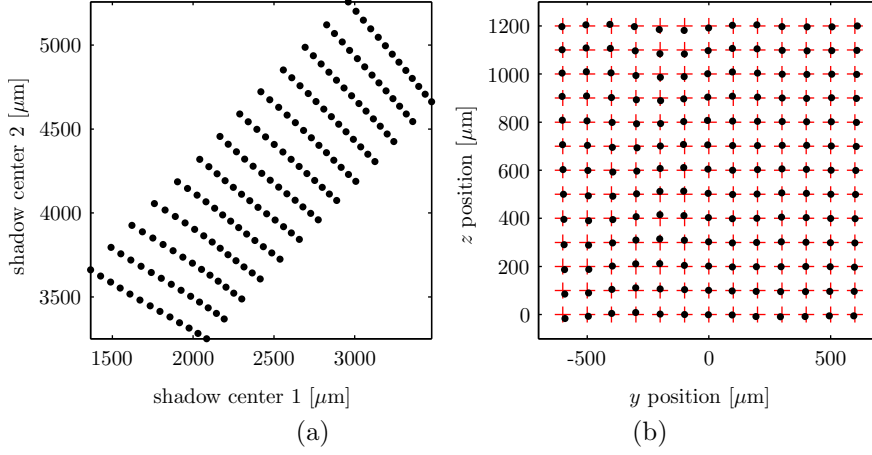


Figure 5.9: (a): Shadow centers for all measurement positions, (b): measurement positions (crosses), transformed shadow centers fitted onto the measurement positions (dots).

measured by using an xy -table with an accuracy of $0.1 \mu\text{m}$ in a conditioned room. The determined shadow centers belonging to all points in the measurement grid are shown in Figure 5.9(a). We want to map these shadow centers to the positions of the string in y and z in the measurement grid. Position $(0,0)$ in the measurement grid is located between the two LEDs about 1 mm above the CCD. This transformation is a mapping from a quadrilateral to a rectangle which includes scaling, rotation, skewing and translation, i.e. a perspective transformation [95]:

$$y = \frac{p_1 s_1 + p_2 s_2 + p_3}{p_7 s_1 + p_8 s_2 + 1} \quad (5.12)$$

$$z = \frac{p_4 s_1 + p_5 s_2 + p_6}{p_7 s_1 + p_8 s_2 + 1} \quad (5.13)$$

in which p_1, \dots, p_8 are the unknown parameters of the perspective transformation. For a given data set $\{y, z, s_1, s_2\}$ we can solve the 8 parameters from (5.12) and (5.13):

$$A\underline{p} = \underline{b} \quad (5.14)$$

$$\text{where } A = \begin{bmatrix} s_1 & s_2 & 0 & 0 & 1 & 0 & -s_1 y & -s_2 y \\ 0 & 0 & s_1 & s_2 & 0 & 1 & -s_1 z & -s_2 z \end{bmatrix}, \underline{b} = \begin{bmatrix} y \\ z \end{bmatrix}$$

The perspective transformation coefficients \underline{p} are computed analytically by using the method of least squares:

$$\underline{p} = (A^T A)^{-1} A^T \underline{b} \quad (5.15)$$

If we compare the transformed shadow centers with the corresponding string locations in the measurement grid visible in Figure 5.9(b), we see a deviation in y as shown in Figure 5.10 which is put in a lookup table for correction.

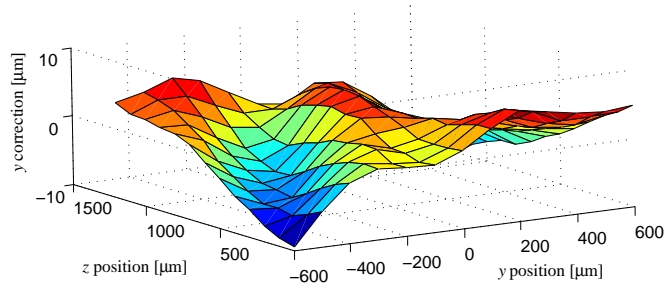


Figure 5.10: Correction lookup table for the measurement area.

For validation, 39 measurements are made where the positions are randomly selected in the measurement area as shown in Figure 5.11. For each point the two shadow centers are transformed to the y and z position of the string using the perspective transformation and after that, the position is corrected with the correction lookup table using bilinear interpolation. The estimated y position is compared with the measured y position. In Figure 5.12 the position estimation error is shown. A similar procedure can be done for the z position, however, in this work we only consider the y position.

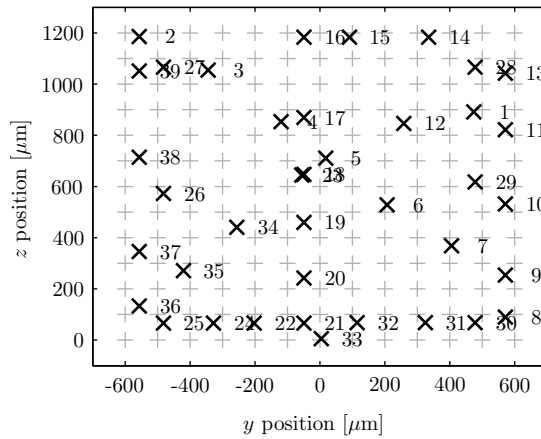


Figure 5.11: String positions used for validation.

5.3.5 Robustness to Temperature Variations

Due to temperature variations, the sensor will expand. A sensor material with a low thermal expansion coefficient, e.g. ceramic, can be chosen such that this

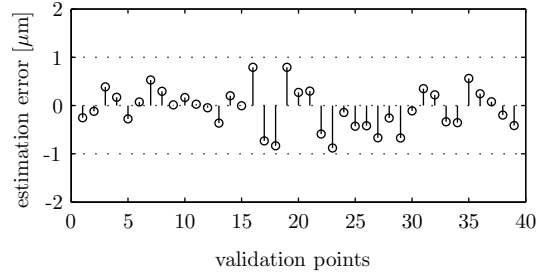


Figure 5.12: Difference between the estimated y position and the measured y position. The error is smaller than $1 \mu\text{m}$ and has a standard deviation of $0.4 \mu\text{m}$.

expansion is negligible or a material with a large thermal conductivity, for example aluminum such that it will have a uniform temperature which can be accurately measured and compensated for.

Furthermore, also due to temperature variations, the sensitivity of the CCD or the intensity of the emitted light by the LEDs can vary. The result is a slight offset in the measured intensity. However, the shape of the shadow remains the same so the same shadow centers will be estimated. In Chapter 6, a more detailed analysis is carried out to investigate the thermal effects.

For the experiments in Chapter 7, the sensor shown in Figure 5.5 is used which has a aluminum housing in combination with a mounting made of PF (Phenol Formaldehyde) which has a low thermal conductivity to obtain a thermal bridge between the hot printhead and relatively cold sensor housing.

5.3.6 Cost Indication

An indication of the cost of one sensor if it would be implemented in an actual product is shown in Table 5.2. Assumed is that a DSP, costing $\text{€}9.00$ in a final product, has enough processing power to handle three sensors considering the required signal processing (peak estimation, mapping and filtering) described.

Table 5.2: Cost estimation per sensor.

DSP	$\text{€}3.00$
LEDs	$\text{€}0.50$
CCD	$\text{€}1.50$
Construction	$\text{€}2.00$
Total:	$\text{€}7.00$

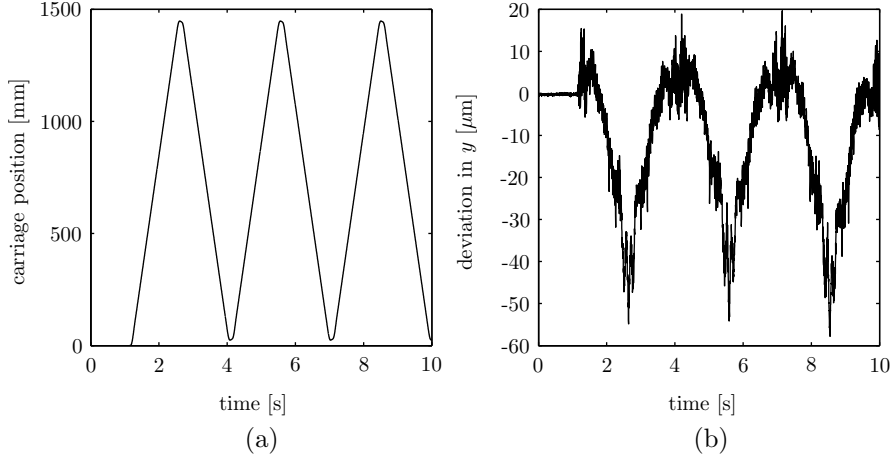


Figure 5.13: Experiment (a): carriage movement, (b): guidance deviation in paper transport direction y of a fixed point on the carriage.

5.4 Measurement Signal Properties

5.4.1 Guidance properties

The carriage guidance in WFPS is usually made of an extruded aluminium profile and therefore its shape contains low spatial frequencies. As an example, suppose that the shape of the guidance is a one period sine over a distance of 1 m with an amplitude of $100 \mu\text{m}$ and the carriage moves with 1 m/s , then, the measured position oscillation is 1 Hz. The vibration frequency of the carriage guidance depends on the stiffness of the guidance and the mass of the carriage. The oscillation frequency will be in the order of 10^1 Hz for a carriage of a few kg. In Figure 5.13, an example of a guidance measurement is shown. More than 95 % of the signal power content is located below 10 Hz as shown in Figure 5.14.

5.4.2 String properties

The fundamental frequency of a string is:

$$f_s = \frac{1}{2L} \sqrt{\frac{T}{m}} \quad (5.16)$$

in Hz with L the length of the string in m, m the string mass per unit of length in kg/m and T the tension of the string in kg/ms^2 . For the k th harmonic the string vibration frequency is kf_s . Due to temperature variations, wear, dirt, and creep the fundamental frequency will drift, which has to be taken into account.

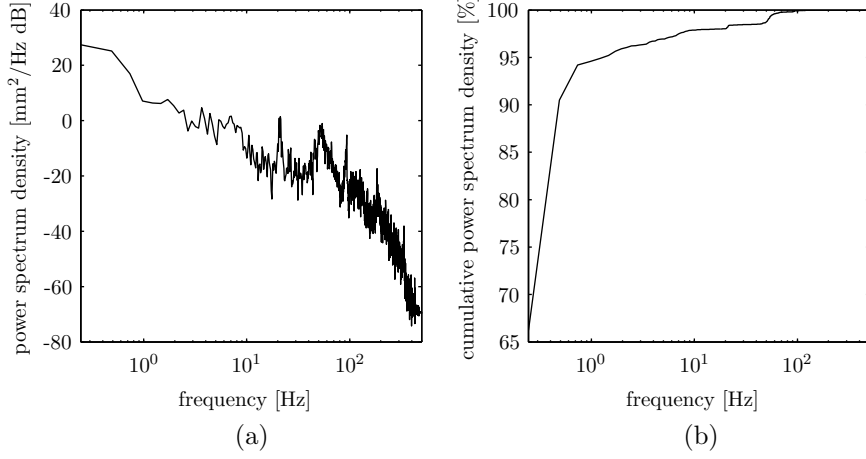


Figure 5.14: (a): power spectrum of Figure 5.13(b), (b): cumulative power spectrum.

The string is tensioned such that it is approximately straight under temperature and tension variations. It is easy to derive that the deflection z_g of the string due to its mass is:

$$z_g\left(\frac{1}{2}L\right) = \frac{\rho g L^2}{8\sigma} \quad (5.17)$$

For a string length $L = 1.5$ m, string density $\rho = 1150$ kg/m^2 , gravity constant $g = 9.81$ m/s^2 and tension $\sigma = 400$ MPa we obtain $z_g\left(\frac{1}{2}L\right) = 8$ μm . This deflection is constant and perpendicular to the measurement direction, so it will not influence the accuracy of the sensor. For homogeneous solid core strings also holds:

$$m = \frac{1}{4}\rho\pi d^2 \quad (5.18)$$

$$\sigma = \frac{4T}{\pi d^2} \quad (5.19)$$

where ρ is the mass density in kg/m^3 , d is the diameter of the string, and σ is the string tension in N/m^2 . From (5.16), (5.18), and (5.19) follows:

$$f_s = \frac{1}{2L}\sqrt{\frac{\sigma}{\rho}} \quad (5.20)$$

ρ is a material property and σ is limited for each material by the yield stress. Together, ρ and σ determine the maximum possible fundamental frequency f_1 for a string length L , see Table 5.3. This is independent of the string diameter as long as holds $d \ll L$.

Material	steel	nylon	okuma "feel the power" platinum 0.5 mm copolymer
Yield stress (50%UTS) σ_{yield} [MPa]	1300	375	412
Ultimate tensile strength UTS [MPa]	2600	750	824
Density ρ [kg/m ³]	7850	1200	1150
Fundamental frequency f_1 [Hz]	203	280	299
Deflection $v(\frac{1}{2}L)$ [μm]	7.4	3.9	3.4
Tension T [N] with $d = 0.5$ mm	255	74	81

Table 5.3: String properties of materials used for guitar strings and fishing lines with $L = 1$ m. The type of steel is a high carbon steel alloy (also called Swedish steel) and the type of nylon is a mono-filament nylon which is a single strand high density extruded nylon.

In WFPS, airflow induced by the carriage movement and printer frame vibrations will excite the string, which in turn will start to oscillate in its eigenfrequencies, especially in the lower eigenfrequencies. It is assumed that the maximum amplitude is about $100 \mu\text{m}$, which will become a problem for the position measurement if they are not removed. We want to reconstruct only the guidance error so we have to remove the high frequency disturbances by using filtering techniques. The standard deviation $\sqrt{E\{(y - E\{y\})^2\}}$ is about $1 \mu\text{m}$ as shown in Figure 5.7, which will not cause any problems. The main challenge is to remove the high frequent string oscillations without distorting the low frequent guidance error information.

5.4.3 Doppler Effect

At both ends, the amplitude of a vibrating string, vibrating only with the fundamental frequency f_1 , is zero and in the middle the amplitude is maximal. However, also higher harmonics are present in the string vibration. The 1st, 2nd, 3rd and 4th eigenmode of a vibrating string are shown in Figure 5.15. The deflection $d(t, x)$ of an ideal string with length L is a function of both time t and position x :

$$d(t, x) = \sum_{k=1}^{\infty} A_k \sin \frac{k\pi x(t)}{L} \sin(2\pi k f_1 t + \varphi_k) \quad (5.21)$$

where A_k and φ_k are the amplitude and phase shift of the k th harmonic respectively. The sensor moves with a constant speed v along the string, $x(t) = vt$, resulting in:

$$d(t) = \sum_{k=1}^{\infty} \frac{1}{2} A_k [\cos(2\pi k (f_1 - \frac{v}{2L})t + \varphi_k) - \cos(2\pi k (f_1 + \frac{v}{2L})t + \varphi_k)] \quad (5.22)$$

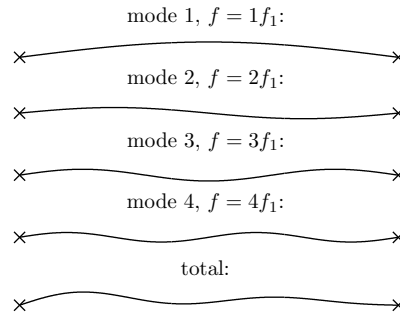


Figure 5.15: The shape of the 1st, 2nd, 3rd and 4th eigenmode of a string and a realization of these modes is shown in the bottom figure.

We see that the frequency of the actual vibration is seen by the sensor as two frequencies shifted by $\pm \frac{v}{2L}$ Hz as shown in Figure 5.16, which is a kind of a doppler effect. For $v = 1$ m/s and $L = 1$ m, the frequency shift is $\pm \frac{1}{2}$ Hz. This requires a robustness to frequency variations of at least $\pm 0.17\%$ for $f_s = 300$ Hz.

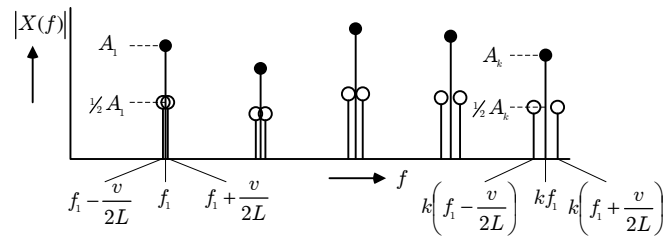


Figure 5.16: Fourier series of a measurement of a vibrating string with a moving sensor showing the doppler effect.

5.5 Harmonics Filter Design

5.5.1 Filter Objective

The objective of the filter system $H(s)$ to be designed (Figure 5.17) is to attenuate n high frequency harmonic distortions in $d(t)$ caused by the string without deteriorating the low frequency guidance error signal $g(t)$. Hence, (5.23) should be minimized such that $y(t)$ resembles $g(t)$:

$$\mathcal{L}\{e(t)\} = (H(j\omega) - 1)\mathcal{L}\{g(t)\} + H(j\omega)\mathcal{L}\{d(t)\} \quad (5.23)$$

where $\mathcal{L}\{\}$ represents the Laplace-operator.

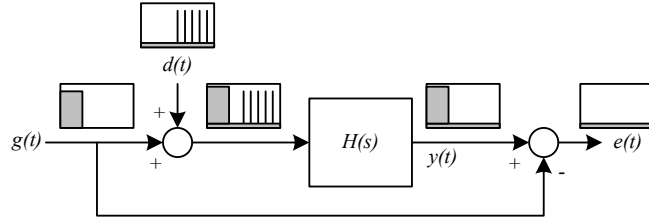


Figure 5.17: An overview of the filter system $H(s)$. The five small graphs show the frequency content of all signals.

Requirements for $H(j\omega) - 1$ are:

$$|H(j\omega) - 1| \leq M_g \quad \forall \quad \omega < 2\pi f_g \quad (5.24)$$

and requirements for $H(j\omega)$ are:

$$|H(j2\pi k f_s)| \leq M_s \quad \text{for } k = 1, 2, 3, \dots \quad (5.25)$$

where M_g is the maximum allowed distortion due to the filtering for all frequency content below f_g and M_s is the minimal disturbance attenuation. Considering $|H - 1| < M_g$ instead of $|H| - 1 < M_g$ is more strict because then the error will be less than M_g regardless a phase difference which is not the case for the latter.

5.5.2 Low pass filter

In order to filter out the string resonances, an intuitive filter choice is a low pass filter. See e.g. [84] for an overview of filters. The phase lag of a FIR (Finite Impulse Response) filter is not beneficial because the disturbances have to be filtered online, so anti-causal shifting is not allowed. In the online filtering case, an IIR (Infinite Impulse Response) filter, and more specifically, an Elliptic filter has superior selectivity. In Figure 5.18, the performance of various orders of Elliptic low pass filters are shown. The pass band ripple is limited to 6 dB to prevent sensor noise amplification and slow transient behavior. Typical requirements for this application are a harmonic attenuation of 40 dB and a maximum distortion of -40 dB at 10 Hz ($|H - 1|(10 \text{ Hz}) < 0.01$). To be able to fulfill these requirements, the minimum cutoff frequency is about 2 kHz, much too high for this application because the material properties of the string limit the fundamental frequency to about 200 Hz for a string length of 1.5 m.

5.5.3 Notch Filter

Considering the shortcomings of a low pass filter the next intuitive filter design is a notch filter with a low order to keep the filter complexity as low as possible.

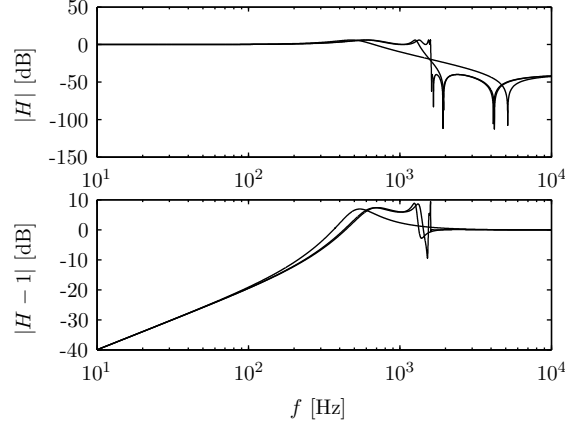


Figure 5.18: Top figure: magnitude of a 2nd order, 4th order and 8th order Elliptic low pass filter with 6 dB pass band ripple. Bottom figure: corresponding magnitude of $H - 1$ representing the maximum distortion of the remaining signal.

However, the filter should be robust to frequency variations of the disturbance. The lowest order notch filter, a 2nd order notch filter, has a frequency robustness of $\pm 0.1\%$ for f_g , f_s , M_g and M_s as specified in the previous section. This is not enough regarding the expected frequency variations, so a higher order notch filter is required to improve the robustness on the expensive of complexity.

Common filter types are Butterworth, Chebyshev and Elliptic filters [84]. The latter has the best selectivity on the expense of ripples in the pass band and the stop band and will therefore be chosen. The computation of the pole zero locations is described in [39], [69]. The transfer function of an Elliptic notch filter with an even amount of poles is written as:

$$H = \prod_{i=1}^m \frac{s^2 + (2\pi f_{zi})^2}{s^2 + 2\zeta_i(2\pi f_{pi})s + (2\pi f_{pi})^2} \quad (5.26)$$

where m is the amount of duplications of a second order notch. Assuming that $f_{zi} \approx f_{pi} \approx f_s \quad \forall i \in \{1, \dots, m\}$ and requiring (5.24) we obtain:

$$\zeta_i \leq \zeta_{max} = \frac{\frac{M_g}{m}}{\sqrt{1 - \left(\frac{M_g}{m}\right)^2}} \frac{f_s^2 - f_g^2}{2f_g f_s} \approx \frac{1}{2m} M_g \frac{f_s}{f_g} \quad (5.27)$$

In Figure 5.19, an Elliptic notch filter with a pass band ripple of 1 dB is shown compared with a 2nd order notch filter. Both filters satisfy (5.24), however, the Elliptic filter has a robustness of $\pm 2.1\%$ and the 2nd order notch has a robustness of $\pm 0.1\%$ considering an attenuation of -40 dB.

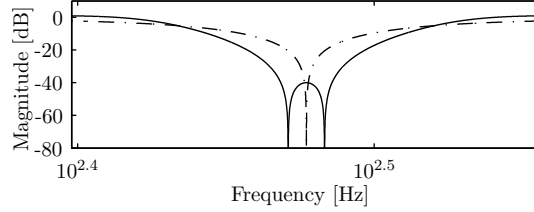


Figure 5.19: 4th order Elliptic notch filter with 1 dB pass band ripple (solid line) compared with a 2nd order notch filter (dash dot line).

5.5.4 Multiband Notch Filter

Because the string vibration contains a number of harmonics, we need to implement several notches located at the excited harmonic frequencies. From (5.27), we obtain the distortion of a single notch at frequency kf_s :

$$M_{gk} \approx 2m\zeta_{max} \frac{f_g}{kf_s} \quad (5.28)$$

For n notches, the damping should be the same to obtain the same frequency robustness for all harmonics to be attenuated. This is desired because the harmonics are directly coupled. The sum of all distortions should be equal to the total allowed distortion M_g regardless the phase:

$$M_g = \sum_{i=1}^n M_{gi} \approx 2m\zeta_{max} \frac{f_g}{f_s} \sum_{i=1}^n \frac{1}{i} \quad (5.29)$$

from which it follows that:

$$\zeta_{max} \approx \frac{1}{2m} \frac{M_g}{\sum_{i=1}^n \frac{1}{i}} \frac{f_s}{f_g} \quad (5.30)$$

Substituting (5.30) into (5.28) we get:

$$M_{gk} \approx \frac{M_g}{k \sum_{i=1}^n \frac{1}{i}} \quad (5.31)$$

M_{gk} is the contribution of a notch at frequency kf_s to the distortion at frequency f_g . This contribution does only depend on the amount of notches and not on the order, the notch type or the frequency difference $\frac{f_s}{f_g}$. The filter width is specified as the lower and upper -3 dB crossing. The width in percentage is equal for all n notches, hence the multi band notch filter can be computed in a straight forward way. An example of a multi band notch filter with notches at 300, 600, 900, 1200, 1500, 1800 Hz is shown in Figure 5.20. In comparison with a single notch as shown in Figure 5.19, the frequency robustness for notches combined has decreased to less than half. Depending on the amount of notches, the total filter order can become too large to be implemented in realtime. In Appendix A and in [8], a method is proposed which solves this problem by reducing filter computations without sacrificing attenuation performance. Notice also the relation with robust high-order repetitive filtering [76].

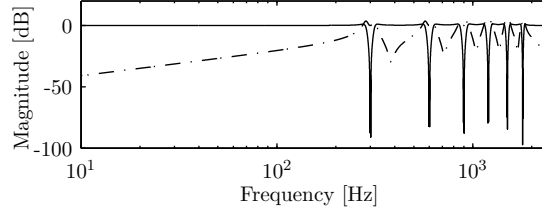


Figure 5.20: Multiband notch filter consisting of 6 Elliptic notches with 1 dB pass band ripple (solid line) having a maximum distortion of $M = -40$ dB at 10 Hz (dash dot line) and a -40 dB $\pm 0.83\%$ frequency robustness.

5.5.5 Simulation

The filter as shown in Figure 5.20 has been implemented in Matlab. For the guidance error g , a 10 Hz cosine with an amplitude of $100 \mu\text{m}$ has been taken. The disturbance signal n is chosen similarly as in (5.22) with frequencies 300, 600, ..., 1800 Hz and 80, 40, 20, 10, 5, $2.5 \mu\text{m}$ respectively such that the maximum amplitude of n is about $100 \mu\text{m}$. The sensor speed v is chosen 1 m/s and the length of the string $L = 1$. In Figure 5.21 the result of this simulation is shown.

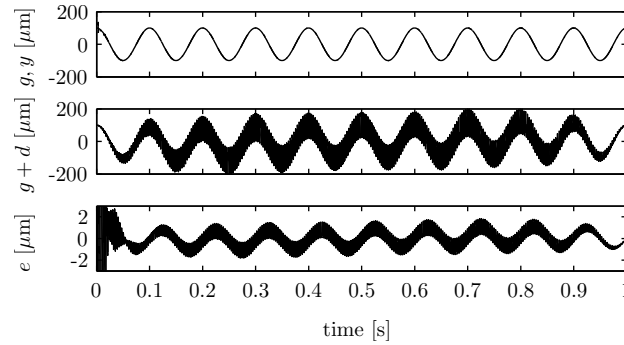


Figure 5.21: Simulation of a moving sensor along a string of 1 m. Top figure: guidance error g , middle figure: measured guidance position, bottom figure: difference between the estimated guidance error and the real guidance error.

The maximum distortion level at 10 Hz due to the filter is $1 \mu\text{m}$ as expected because $M_g = 0.01$. The maximum distortion level of the disturbance signal amplitude is $1 \mu\text{m}$ which is also expected because the maximum amplitude of n is $100 \mu\text{m}$ and $M_s = 0.01$. Furthermore, the settling time of the filter is 0.05 s which is acceptable because this is smaller than the reversal time which is in the order of 0.1 - 0.2 s, i.e., when the carriage starts to reverse, it excites the printer frame. These parasitic dynamics of the printer frame excite the string which is attached to the printer frame.

Chapter 6

Short Stroke Printhead Guidance Mechanism

This chapter is based on [67, 68] and describes the mechatronic design of a short stroke printhead guidance mechanism and its actuator. A dynamic finite element model (FEM) is developed to determine the eigenfrequencies, mode shapes and transfer functions of the printhead guidance mechanism. Furthermore, an experimental setup has been designed and built to validate the concept.

6.1 Mechatronic Concept

A mechatronic solution is proposed, by which each printhead is actuated and controlled in y -direction. A schematic view is shown in Figure 6.1(a). The dynamic principle of the concept is explained by the model shown in Figure 6.1(b). The printhead mass m is connected to the carriage by means of a damper d and a spring k , depending on the guiding mechanism. The carriage at position y_c introduces disturbances on the printhead position y_p . Position y_p will be measured with respect to an absolute reference independent of all disturbing sources as described in Chapter 5, and will be controlled by means of an actuator force F_{act} . The equation of motion can be formulated as:

$$m\ddot{y}_p(t) + d(\dot{y}_p(t) - \dot{y}_c(t)) + k(y_p(t) - y_c(t)) = F_{act}(t) \quad (6.1)$$

It is preferred to keep k and d low, because then disturbances from y_c have minimal influence on the printhead position y_p . Furthermore, a minimal actuator

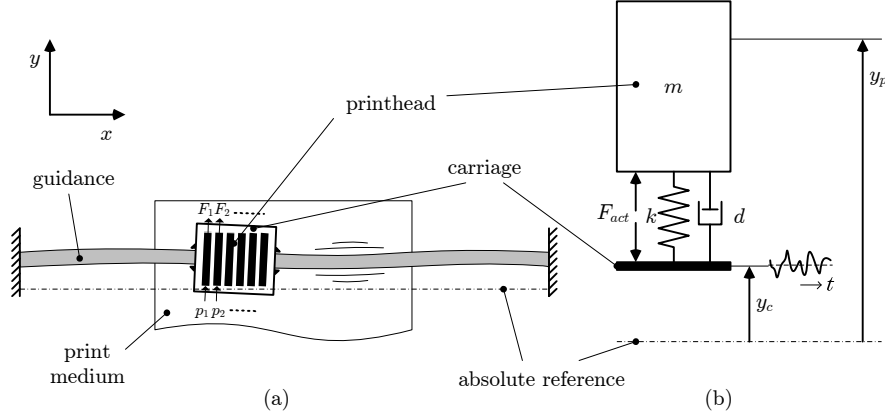


Figure 6.1: (a): active printhead alignment concept, (b): dynamic model of the active printhead alignment concept.

force F_{act} is desired, resulting in a light and compact actuator with low power consumption. In order to compensate for disturbances from y_c which contains:

- (i) guidance deviations in the order of $100 \mu\text{m}$ and an observation frequency below 10 Hz, and
- (ii) guidance vibrations in the order of $10 \mu\text{m}$ with a frequency in the order of 10 Hz.

a minimum bandwidth of about 50-100 Hz is specified for the control system of the actuated printhead to obtain an alignment accuracy below $10 \mu\text{m}$. Vibrations up to this bandwidth will be reduced by the alignment system. Non-repetitive dynamic position errors in x -direction must be prevented in the design since they cannot be compensated by the jet-timing. At last, the system must be able to resist the high temperatures caused by the printheads.

6.1.1 Boundary Conditions

The carriage containing a set of printheads moves in x -direction over a guidance, a $\pm 1.5 \text{ m}$ aluminum extrusion profile. With constant carriage speed v_c , the printheads jet ink on the print medium underneath. By stepwise feeding of the print medium in y -direction, a print is built up in strokes. Properties of the printhead are shown in Table 6.1.

The manufacturing tolerances on the carriage and the printheads mainly result in static misalignments, in the order of a few tens of μm . Dynamic disturbances are caused by the guidance. Despite the polished bearing surfaces, a slight waviness (profile error) will generally exist. An amplitude of max. $100 \mu\text{m}$ and resulting frequencies up to 10 Hz are assumed for $v_c = 1\text{-}2 \text{ m/s}$. Also guidance vibrations will

Table 6.1: Printhead properties

dimensions $l \times w \times h$	$80 \times 20 \times 120$ mm
uniform mass m	0.15 kg
material	ceramic
coefficient of thermal expansion (CTE) α	$5 \mu\text{m}/\text{mK}$
ink temperature	$130 \text{ }^\circ\text{C}$

occur during printing where the eigenfrequencies can change with the position of the carriage. In current WFPS, the dominant vibration frequency is in the order of 10^1 Hz. Although the printheads may be mutually aligned in case of guidance vibrations, the misalignment with respect to the paper will be visible on the print.

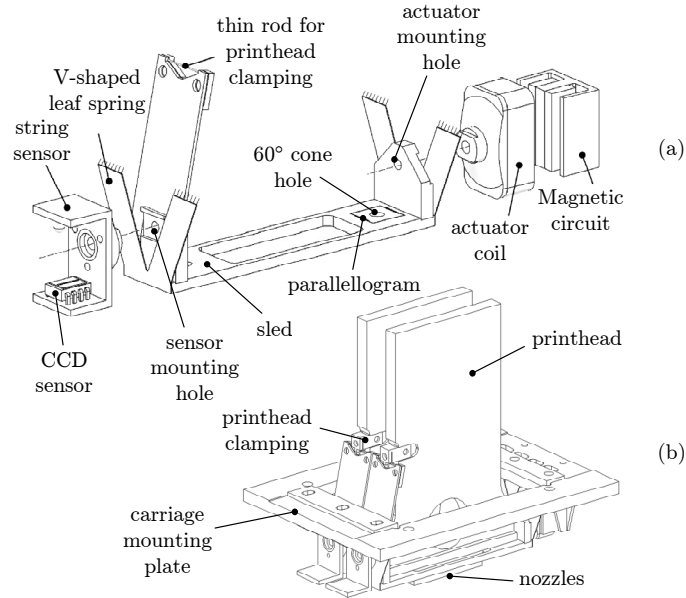


Figure 6.2: (a): An exploded view of the alignment mechanism. (b): assembly of the alignment mechanism.

6.2 Overview of the Printhead Alignment Mechanism

The design of the developed alignment mechanism containing the short stroke guidance, the voice coil actuator and the string position sensor is shown in Figure 6.2 and Figure 6.3. Detailed information about the design of the alignment mechanism can be found in [68]. The alignment mechanism is compact such

that several printheads can be staggered in the carriage. The compactness of the carriage is essential for the productivity of the printer [5].

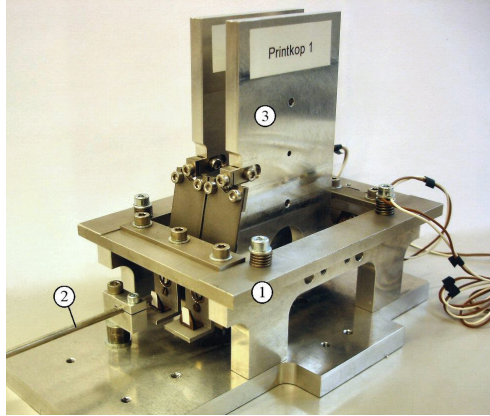


Figure 6.3: Picture of the alignment mechanism setup: (1) carriage, (2) fiber optic sensor (Philtec D64-EQ), and (3) printhead dummies.

A total stroke of $300 \mu\text{m}$ in y -direction is required which can be consumed by the carriage guidance deviation and vibrations, carriage manufacturing tolerances and printhead manufacturing tolerances. To obtain a good print quality with a resolution of 600 dpi, the printhead alignment accuracy should be less than $10 \mu\text{m}$, as determined from visual inspection of printed samples.

6.3 Design of the Guiding Mechanism

The printhead needs to follow an accurate linear movement, for which several principles are explained in [27, 53, 88]. Some examples of short stroke actuation mechanisms can be found in [33, 48]. Five of the six Degrees of Freedom (DOF) of the printhead need to be fixed. Only the y -translation must be free for a small linear movement. A parallel leaf spring mechanism as shown in Figure 6.4 is particular suitable for this purpose. The principle is based on elastic elements, with the advantages of no hysteresis, no wear and no play. In order to prevent the printhead from being over-determined, one leaf spring is given an elastic hinge, releasing its rotational constraint around the y -axis.

6.3.1 Leaf Spring Characteristics

During printing, acceleration levels for a_x up to 50 m/s^2 can be expected in x -direction mainly due to reversal of the carriage. From linear beam theory we can compute the deviation in x -direction $\delta(p)$ where p represents the mid leaf spring position with respect to the nozzle axis in m. An inertial force $F_i = ma_x$ will act on the center of mass of the printhead h_{cm} (see also Figure 6.4). The resulting moments M_A , M_B and forces F_A , F_B on the leaf spring ends will cause

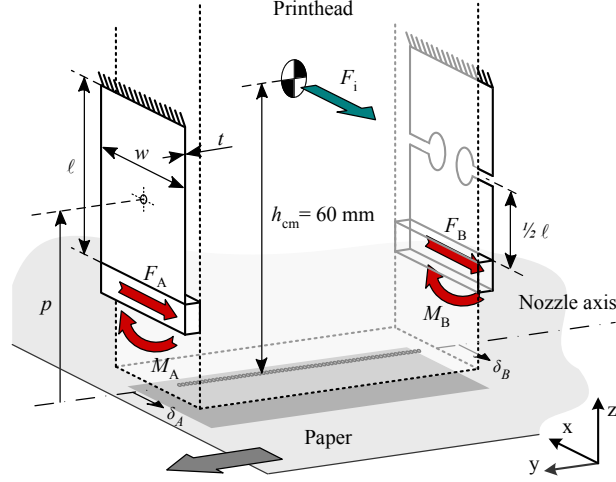


Figure 6.4: Leaf spring mechanism and printhead mounting.

a deflection of the printhead and its nozzle axis in x -direction, directly resulting in dynamic dot-positioning errors. Expressions for the nozzle deflections δ_A , δ_B at both sides of the printhead are given by (6.2) and (6.3), which are based on standard formulas from linear beam theory [37]:

$$\delta_A = \frac{F_A \ell^3}{3EI_y} - \frac{M_A \ell^2}{2EI_y} + \varphi_y (p - \ell/2) \quad (6.2)$$

$$\delta_B = 2 \frac{F_B (\ell/2)^3}{3EI_y} + \varphi_y p \quad (6.3)$$

$$\varphi_y = \frac{F_A \ell^2}{2EI_y} - \frac{M_A \ell}{EI_y} \quad (6.4)$$

Herein, E is the Young's modulus in Pa, I_y the area moment of inertia of the leaf spring in m^4 and ℓ is the length of the leaf spring. The printhead rotation φ_y is determined by the full leaf spring. Assuming $M_A = F_i (h_{cm} - p + \ell/2) - M_B$, $M_B = F_B \ell/2$ and $F_A = F_B = F_i/2$, then both (6.2) and (6.3) can be simplified to

$$\delta(p) = \frac{ma_x \left(\frac{1}{24} \ell^3 + (p^2 - h_{cm} p) \ell \right)}{EI_y}. \quad (6.5)$$

Thus, in the configuration as in Figure 6.4, all the nozzles will deflect equally, regardless of p . In Figure 6.5, the nozzle deflection $\delta(p)$ is plotted. A set of steel leaf springs with dimensions $\ell \times w \times t = 25 \times 20 \times 0.25$ mm is considered, resulting from a compromise between a low translation stiffness, a high in-plane

leaf spring stiffness and the limited space around the printhead. The nozzle deflection appears equal to zero for $p \approx 0$ and $p \approx 0.06$ m.

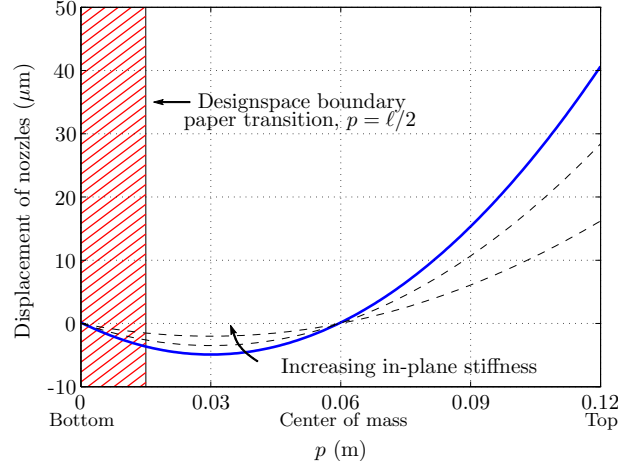


Figure 6.5: Nozzle displacement of printhead loaded with 50 m/s^2 .

Also important is the nozzle position sensitivity for temperature gradients and thermo-mechanical effects in the printhead, which decreases when the leaf springs are mounted close to the nozzle axis ($p \rightarrow 0$). However, the paper under the printhead as in Figure 6.4 bounds the position of the leaf springs by $p \geq \ell/2$. In this case, a nozzle deflection of several micrometers will remain. A further reduction can be achieved by: (i) a further increase of the in-plane stiffness, (ii) optimizing the leaf spring geometry. Although most common, the first option will consequently lead to a higher power dissipation of the actuator. Only t and ℓ of the leaf springs can be varied, influencing the translation stiffness by $(t/\ell)^3$.

In the second approach, the nozzle displacements are reduced by forcing the printhead to rotate around its nozzle axis. This can be explained by a 2D FEM-model made with Marc/Mentat [75], as shown in Figure 6.6. Three different leaf spring geometries are examined for the load case where $M_A = 0.40 \text{ Nm}$ and $F_A = 3.75 \text{ N}$ are applied at the bottom of the leaf spring, which holds for $p = \ell/2$.

With the standard leaf spring (Figure 6.6(a)), the printhead rotates around the leaf spring's center, resulting in an x -displacement at the nozzle axis. The trapezoid (Figure 6.6(b)) shows less deflection, because the deformation will mainly concentrate in the narrower part of the leaf spring, lowering the center of rotation. With the V-form leaf spring (Figure 6.6(c)), the center of rotation is moved directly under the leaf spring where the arms of the V-form cross, and coincides with the nozzle axis. When the leaf springs deform under the inertial loads from the printhead, the nozzles will stand still. Because the nozzles are less sensitive for y -rotations than x -translations, the V-form will result in a better dot-positioning. In Section 6.5.2 it will be shown that the V-form also suppresses the modal displacements of the nozzles at the lowest eigenfrequency excited by

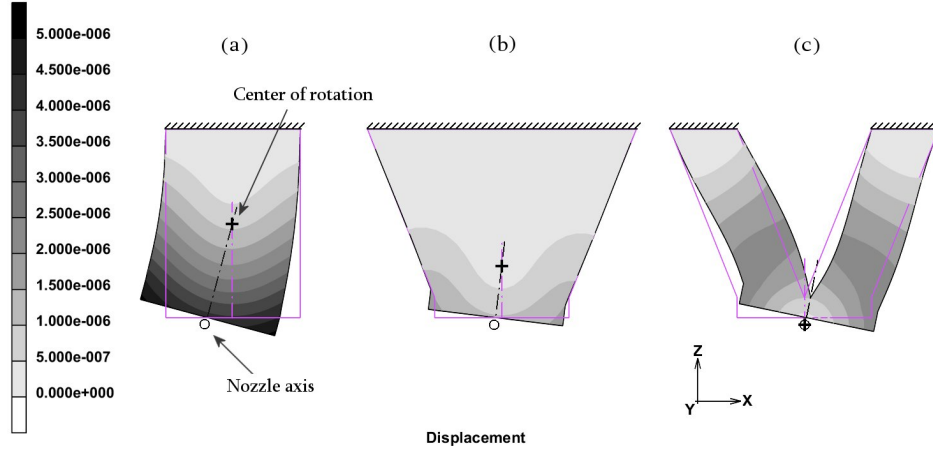


Figure 6.6: Deformation of different leaf spring geometries under load. Thickness t and length ℓ are kept constant.

reversal of the carriage. However, the usage of two V-form leaf springs results in an over-determined DOF of the sled, i.e. rotation around the nozzle axis. This over-determined DOF should be released at the nozzle axis.

6.3.2 Sled Design

From a dynamic point of view, fixing the leaf spring directly to the printhead as in Figure 6.4 is attractive because of the minimal mass and high guiding stiffness. However, easy and proper fixing of the leaf springs is difficult when the printhead must be detachable for replacement. A total of 12 DOFs should be fixed, 6 per leaf spring end. Also microslip should be taken care of at the attachment points, because of the many heating cycles and the difference in coefficient of thermal expansion (CTE) between the printhead body and leaf springs. Considering these facts, a light and stiff sled for mounting on the printhead is applied as an alternative. An open design for easy printhead detachment is realized by fixing both the actuator and sensor to the sled. The applied stainless steel material (AISI 420) prevents corrosion on essential contact surfaces. A relative low CTE of $10 \mu\text{m}/\text{mK}$ will keep the difference in expansion with the ceramic printhead small. Furthermore, a symmetrical design will minimize positioning errors due to thermo-mechanical effects. A detailed overview of the printhead fixation and the sled design is given in Figure 6.7.

The printhead must be fixed to the sled in all 6 DOFs, preferably close to the nozzle axis since accuracy is only required there. This is achieved by two balls, pressed in the underside of the printhead, and resting in conical center holes made in the bottom plate of the sled, where each ball fixes 3 DOFs. One DOF

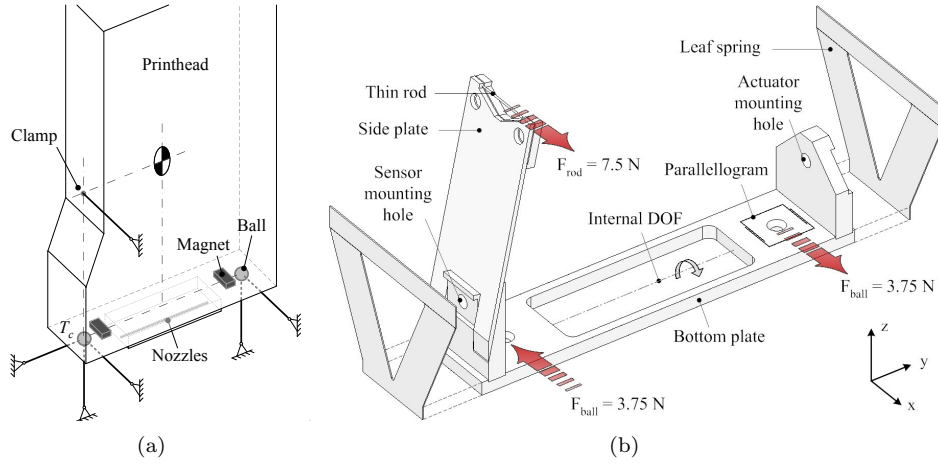


Figure 6.7: (a): Printhead fixation in all DOFs, (b): acting forces on the sled design.

(in y -direction) should be released, for free expansion of the printhead during heating. Therefore, a small parallelogram around the center hole is made (see Figure 6.8(a)). Finally, the rotation around the y -axis, which DOF is less important, is fixed by clamping the printhead to a thin rod at the center of mass. In this way, a printhead suspension is created with minimal hysteresis. For accurate printhead positioning, the printhead position sensor is mounted near the thermal center T_c of the printhead with respect to the sled.

During reversal, the balls in the printhead will apply a sideways inertial load F_{ball} of 3.75 N onto the sled (see Figure 6.7). A preload force is needed to fix the balls in the conical center holes (standard apex angle 60°). Therefore, magnets will be glued next to each ball, attracting the printhead to the bottom plate. Like normal iron, AISI 420 stainless steel has good ferromagnetic properties. A comparison of commonly used magnet materials is shown in Table 6.2. High printhead temperatures up to 130°C should be regarded, otherwise a permanent loss of magnetization could occur. A safe choice is Samarium-Cobalt (SmCo), which also minimizes volume and weight due to its relative high strength. The applied magnets provide an attracting force of 8 N total.

Table 6.2: An overview of some commonly used permanent magnets [26, 43].

magnetic material	remanence B_r (T)	coercivity H_c (kA/m)	thermal stability		curie temp. ($^{\circ}$ C)	max. op. temp. ($^{\circ}$ C)	relative cost
			$B_r/^{\circ}$ C	$H_c/^{\circ}$ C			
Ferrite	≤ 0.4	250	-0.2 %	+0.4 %	450	300	1
SmCo	1,0 - 1,1	700	-0.03 %	-0.2 %	750	250	20
Alnico	1,0 - 1,2	100	-0.02 %	-0.03 %	850	450	6
NdFeB	1,2 - 1,3	850	-0.11 %	-0.6 %	310	80 - 150	10

The bottom plate allows for torsion around the y -axis in order to eliminate the over-determination caused by the two leaf springs. In theory, the bottom plate has more internal DOFs, but the dominant dynamics are not affected since the eigenfrequencies are sufficiently high, as will be shown later.

The carriage in WFPS will in general contain several printheads. For a high productivity of WFPS, the printheads should be arranged closely spaced. For this purpose, the sleds are staggered alternately with 1 mm in y -direction as in Figure 6.8(b). In this way, the V-form leaf springs do not take in much space. In order to keep the printheads in-line, the printhead joints of the staggered sleds are shifted back.

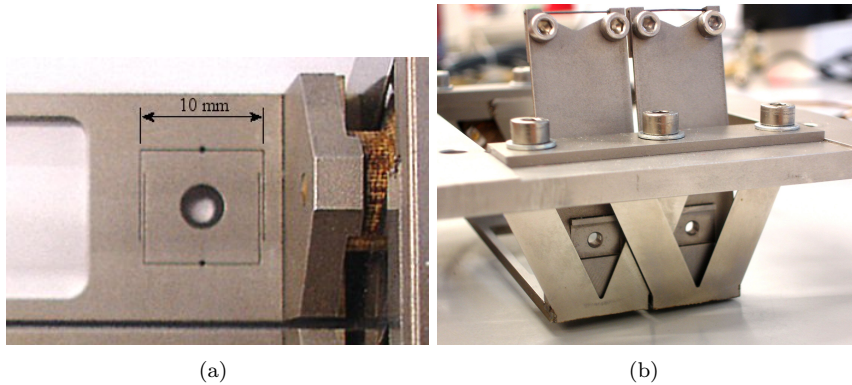


Figure 6.8: (a): Parallelogram for thermal expansion of the printhead, made by wire EDM, (b): staggering of the sleds for minimal spacing.

6.3.3 Fabrication

Most of the sled components can be made by common manufacturing processes, which are inexpensive in mass production. However, the parallelogram in the bottom plate is quite complex for which wire EDM (Electrical Discharge Machining) must be used. This is an expensive process, but cost can be saved by stacking the 3 mm thin bottom plates in production. All components of the sled, including the leaf springs, are welded together to prevent microslip in the system. High precision can be obtained by using laser welding, where the heat supply during welding is minimal.

The total cost of a single unit is shown in Table 6.3. This extra cost is compensated by relaxation of the manufacturing tolerances of the rest of the construction. By assuming that

- (i) the costs are proportional to the printing accuracy reduction factor,
- (ii) the costs of the printer frame, guidance, carriage, printheads that determine the alignment accuracy are €500,-,
- (iii) the active printhead alignment concept improves the alignment accuracy by a factor of 5,
- (iv) the WFPS contains 8 printheads

then a printer with a printhead alignment accuracy improvement of a factor 5 costs €2500,- when scaling conventional WFPS and €500,- + $8 \times €27,- = €716,-$. Reasoning the other way around by keeping the printhead alignment accuracy equal, the costs of the printer construction can be reduced by a factor of 5 to €100,-. Adding the costs for the active alignment mechanism results in €316,- which is lower than €500,- of the conventional WFPS.

Table 6.3: Cost of production overview.

sled, leaf springs, actuator	€20,-
sensor (see Table 5.2)	€7,-
total:	€27,-

6.3.4 Stiffness, Linearity and Hysteresis

In Table 6.4 the guiding stiffness of the leaf spring mechanism is shown, emphasizing the low stiffness in sled movement direction k_y compared to the other directions. The measured value is a bit lower, which is likely due to the finite stiffness of the joints. Also a small hysteresis is noticed (Figure 6.9), which is about $\pm 1.5 \mu\text{m}$ ($\pm 0.3\%$ full range). The linearity of the guiding mechanism has been found to be $\pm 1.6\%$ full-scale. No discontinuities are measured when the sled is moved through the neutral position, which means that the internal stresses in unloaded state are minimal.

Table 6.4: Guiding stiffness of the leaf spring mechanism (at center of mass printhead).

Parameter	Modeled	Measured
Stiffness k_x	425 kN/m	-
Stiffness k_y	7 kN/m	6.0 kN/m
Stiffness k_z	1100 kN/m	-

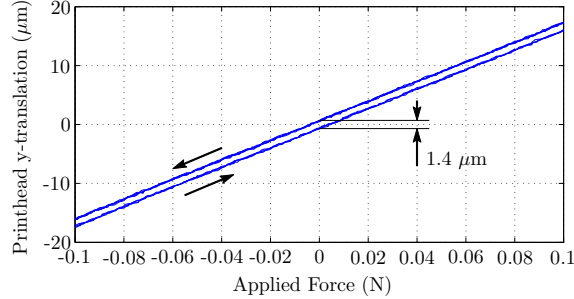


Figure 6.9: Hysteresis of the sled around neutral position (full range -250 to 250 μm , 5 cycles).

6.4 Actuator Design

6.4.1 Actuator Specification

A linear voice coil actuator will be used for actuating the printhead. This type of actuator is fast, works contact-free and has no cogging forces, which makes the actuator attractive for high precision positioning applications. A low-cost voice coil actuator, meant for high temperature environments, is designed with the help of FEM. The required actuator force F_{act} is determined by simplifying (6.1) to:

$$m\ddot{y}_p(t) + k_y y_p(t) = k_y y_c(t) - F_{act}(t) \quad (6.6)$$

where the damping d of the leaf spring guiding mechanism is neglected. In the desired situation when $y_p(t) \simeq \dot{y}_p(t) \simeq 0$, the actuator only needs to cancel the disturbance from the carriage $k_y y_c(t)$, by which the right hand side approximates 0. The inertial term $m\ddot{y}_p(t)$ could become nonzero due to printer frame oscillations, however, because of the high mass of the printer frame, the acceleration amplitude is low and the disturbing force on the printhead is negligible compared with the leaf spring force. Suppose that a printer frame disturbance of 40 Hz (frequency just below the bandwidth of the printhead alignment controller) with an amplitude of 10 μm is present, then the amplitude of the inertial force $m|\ddot{y}_p(t)|$ is $0.15 \cdot 10 \cdot 10^{-6} (2\pi 40)^2 \approx 0.1$ N. The maximum force delivered by the actuator to compensate for the stiffness of the leaf springs is computed by:

$$\max F_{act} \approx k_y \max |y_c| \quad (6.7)$$

which results in 1 N for $\max |y_c| = 150 \mu\text{m}$. Neodymium Iron Boron (NdFeB) based magnets are often applied in powerful and compact actuator designs. However, the heat generation in the printhead and coil may lead to too high ambient temperatures for the magnet (Table 6.2). For the same considerations as mentioned in the sled design, SmCo magnets will also be used in the actuator. Fur-

Table 6.5: Parameters used for the magnetostatic FEM-model made with ANSYS.

magnetic remanence B_r	1 T
magnetic coercivity H_c	700 kA/m
magnetic saturation	2 T
air relative permeability μ_r	1
air-gap mean magnetic flux density B_{gap}	0.33 T
air-gap maximum magnetic flux density	0.44 T
current density in the coil J	5 A/m ²
coil volume V_c	600 mm ³
yoke height h_y	13.5 mm

thermore, an advantage of SmCo magnets is the better thermal stability, providing a nearly steady force constant over a wide temperature range.

6.4.2 Simulation

Using a magnetostatic FEM-model made with ANSYS [42], a rectangular actuator is designed, as shown in Figure 6.10. The final dimensions are the result of some iterative calculations, in order to achieve the highest ratio of generated force per actuator volume. An optimum is found when the thickness of the magnet and the air-gap are equal. The coil is made 1 mm wider than the magnets, to obtain a steady force constant over the total stroke of 300 μm .

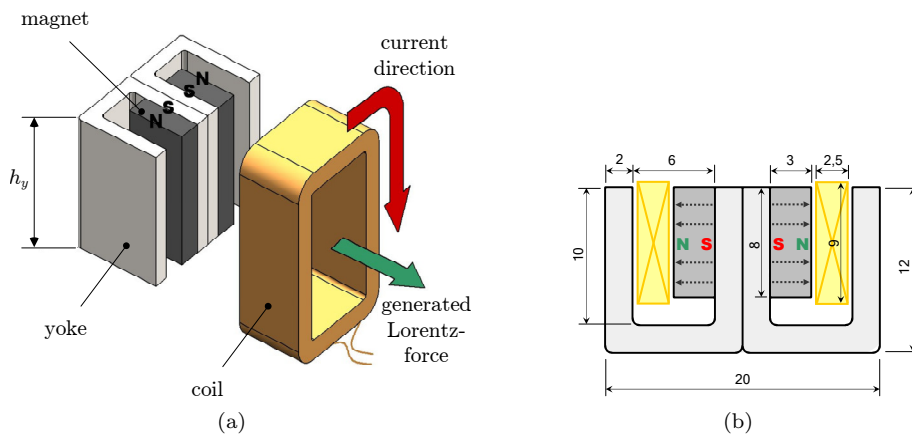


Figure 6.10: Exploded view of the designed actuator (a) and the dimensions in mm (b)

Figure 6.11 shows the FEM-model of the magnetic circuit. Because of the symmetry, modeling only half of the actuator is sufficient. The parameters used are shown in Table 6.5. The yoke is modeled using a typical B-H curve of iron.

Assuming a static situation, the force generated by the actuator becomes:

$$F_{act} = B_{gap}IL_w = B_{gap}V_cJ \quad (6.8)$$

where I is the supplied current in A, L_w and V_c are the wire length in m and coil volume in m^3 within the magnetic field respectively, and J the current density in the coil in A/m^2 . A safe value for J is about $5 \text{ A}/\text{m}^2$, for preventing excessive heat generation in the coil during continuous operation. Reluctance forces, counteracting the magnetic field, can be neglected since they become only significant at current density levels of $10 \text{ A}/\text{m}^2$ and higher.

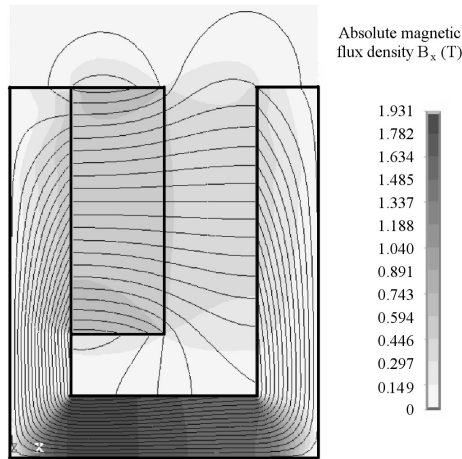


Figure 6.11: Magnetic flux lines and flux density in one side of the magnetic circuit.

6.4.3 Testing the Prototype Actuator

For robustness, the actuator built for the experimental setup is made a bit more powerful than required. The yoke height h_y has been chosen 22 mm. A thermoset coil base is glued to the coil for mounting the coil to the sled.

Several static as well as dynamic measurements are performed to examine the quality of the actuator. The general specifications of the actuator are given in Table 6.6, and the dynamic response is shown in Figure 6.12. For the dynamic measurement, the yoke has been attached to a frictionless linear guide. The coil, connected to the fixed world, is supplied with a random noise current, while the yoke position x is being measured. The generated output force is determined using $F_{out} = m\ddot{x}$, where m is the moving mass of the linear guide including the yoke. The sampling frequency was taken 4096 Hz.

A static gain exists between I_{in} and F_{out} for a wide range of frequencies. The force constant is found 3.85 N/A (11.7 dB). In the specified bandwidth range of the printhead controller (50-100 Hz), the maximum phase loss is less than 3° after removing the sampling delay¹. Therefore, the influence of the actuator on the dynamic performance of the printhead controller will be minimal. The small remaining phase loss is expected to be caused by the effect of Eddy currents in the actuator yoke.

Table 6.6: General actuator specifications (measured at 20°C).

Number of coil windings N	± 250
Cross section A	$\pm 24 \text{ mm}^2$
Wire diameter (copper)	0.25 mm
Coil resistance R_c	7.45 Ω
Self-induction L in yoke	3.06 mH
Mean B in air-gap	0.34 T
Coil mass (incl. cap)	11.6 g
Maximum force constant	3.85 N/A
Deviation force constant (300 μm stroke)	$\leq 1\%$
Max. continuous force F ($J = 5 \text{ A/mm}^2$)	1.85 N

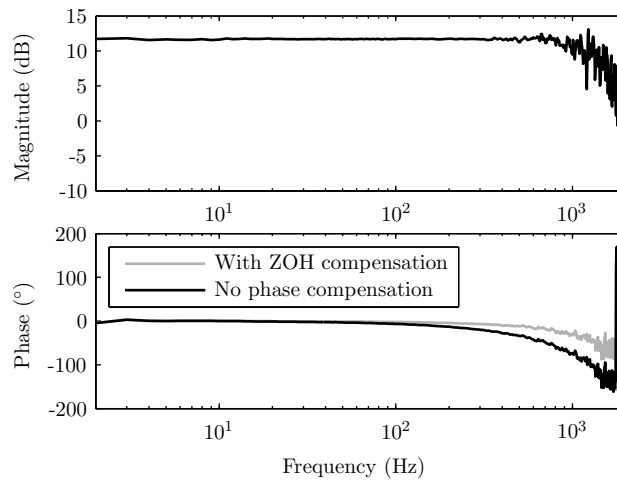


Figure 6.12: Dynamic behavior of the actuator, $H = \frac{F_{out}}{I_{in}}$ in N/A.

¹The DAC's zero-order hold used in the experimental setup causes a lagging effect on I_{in} .

6.5 Eigenmode Analysis

During the mechanical design, the dynamic performance of the printhead guiding mechanism is investigated, using eigenmode analyses and transfer functions determined by FEM calculations. An important benefit of this approach is that the dynamic behavior of the design is well understood before realization. Furthermore, a bandwidth estimate for the design can be determined, and necessary steps can be taken early in the design process for improving the performance.

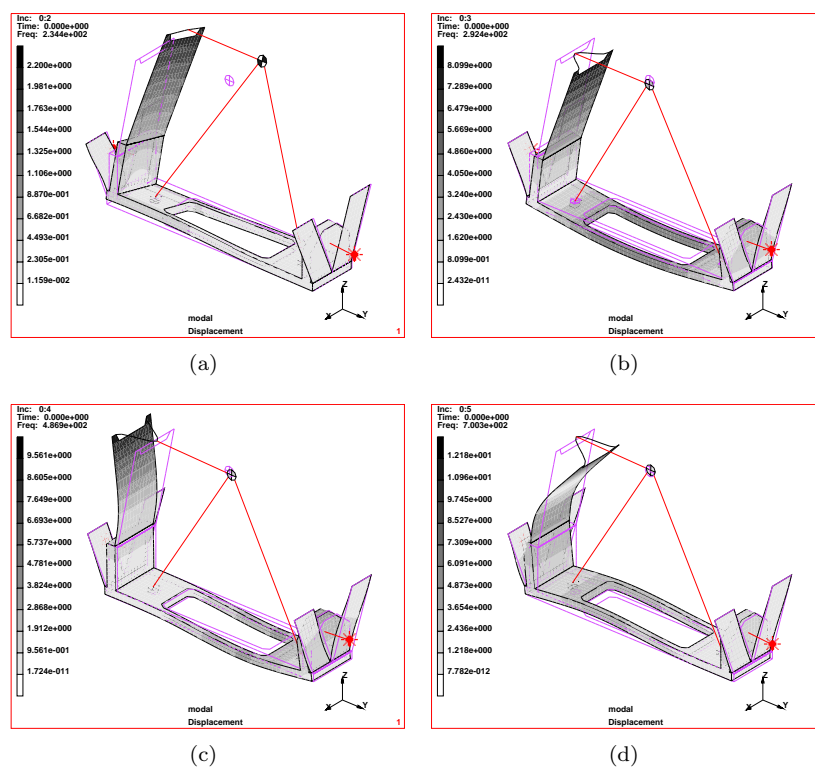


Figure 6.13: (a) to (d): The 2nd to 5th eigenmode of the sled including printhead.

6.5.1 FEM Model Description

The model is composed of 3D solids (sled) and shell elements (leaf springs), which are connected with transition elements. To simulate the free moving carriage, the leaf spring ends are fixed in all DOFs except for the x -direction, and a total mass of 3 kg is added here. The printhead, the sensor and the actuator coil, are modeled as point-masses. They are connected to the sled by means of rigid body elements.

6.5.2 Eigenfrequencies and Mode Shapes

In Table 6.7 the resulting eigenfrequencies of the system below 2 kHz are shown. The rigid body mode in x -direction is omitted. The 1st eigenmode can be described by the sled translating in the leaf spring guiding, like a simple mass-spring system. A large gap exists between the 1st and 2nd eigenfrequency which is, as designed, due to the relative low translational stiffness (for low actuator power) combined with a high stiffness for all other DOFs.

Table 6.7: Calculated eigenfrequencies of the guiding system.

Mode#	Freq. (Hz)	Mode shape description
1	28.3	Sled movement in leaf spring guiding
2	234.4	Printhead rotation around nozzle axis
3	292.4	1 st bending mode of sled
4	486.9	2 nd bending mode of sled
5	700.3	3 rd bending mode of sled
6	1051.0	S-curving of bottom plate (xy -plane)
7	1664.7	Sled movement in x -direction
8	1794.2	Torsion mode of side plate

Of more interest are the 2nd to 5th eigenmodes as shown in Figure 6.13. The printhead's center of mass is marked with a ' \oplus ' sign. The 2nd eigenmode shows modal displacements in x -direction, in contradiction to the other depicted eigenmodes, which mainly occur in the yz -plane. As a consequence, the carriage drive which provides the movement in x -direction over the guidance, will excite the 2nd eigenmode, for example by carriage reversal. However, the precautions taken by the introduced V-form leaf spring force a printhead rotation around the nozzle axis in this eigenmode, thereby minimizing the displacement of the nozzles.

The other three eigenmodes occur from bending of the thin sled design. Despite the relative high printhead mass, the eigenfrequencies are high, mainly by fixing the printhead joints (ball supports) close to the leaf springs, where the sled stiffness is high.

6.5.3 Transfer Functions

With the modal displacements $U = \{U_{in}, U_{out}\}$ and eigenfrequencies $\{\omega_1 \dots \omega_n\}$ from FEM, a state space model can be constructed in modal form [32]:

$$\dot{\underline{x}}(t) = A\underline{x}(t) + B\underline{u}(t) \quad , \quad \underline{y}(t) = C\underline{x}(t) + D\underline{u}(t) \quad (6.9)$$

in which

$$A = \begin{bmatrix} O^{n \times n} & I^{n \times n} \\ -K^{n \times n} & -D_a^{n \times n} \end{bmatrix}, \quad (6.10)$$

$$B = \begin{bmatrix} O^{n \times m} \\ U_{in}^{n \times m} \end{bmatrix}, \quad (6.11)$$

$$C = [(U_{out}^T)^{k \times n} \quad O^{k \times n}], \quad (6.12)$$

$$D = [O^{k \times m}], \quad (6.13)$$

and \underline{x} is a column $2n \times 1$ with the positions and velocities of the nodes, \underline{u} is a column $m \times 1$ with m inputs, and \underline{y} is a column $k \times 1$ with k outputs. The mass matrix is scaled to unity. Matrices K and D_a are the stiffness and damping matrix divided by the mass matrix, which are both diagonal, with respectively $\{\omega_1^2 \dots \omega_n^2\}$ and $2\zeta_i \omega_i$ on their diagonal axes. Finally, ζ_i represent the modal damping factor for each eigenmode i . In Matlab [63], frequency response functions (FRF) are derived from the state space model and simulations in the time domain are performed.

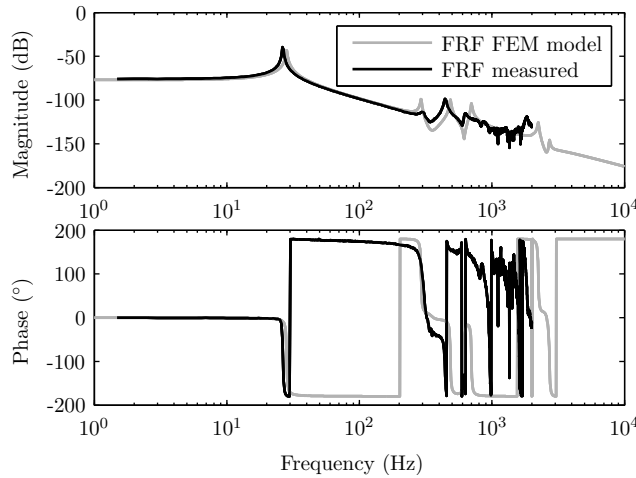


Figure 6.14: FRF of the sled design including printhead $H = \frac{y_p}{F_{act}}$ in m/N.

In the FRF analysis, the input \underline{u} is the actuator node and the output \underline{y} is the sensor pick-up position, which both are directed in y -direction. A modal damping of 1% ($\zeta = 0.01$) is assumed for all modes. In Figure 6.14, the modeled FRF of the guiding mechanism is shown. The mass-spring behavior is clearly visible. The stiffness is dominating before the 1st eigenfrequency (slope 0), and the mass beyond that frequency (slope -2). The 2nd eigenmode (234.4 Hz) is absent, which implies that none of the considered modal displacements are in y -direction. Theoretically, the

actuator and sensor cannot excite the system or measure displacements other than in y -direction respectively. Around the 3^{rd} mode, the phase drops through -180° without returning, which will limit the attainable bandwidth of the controller. However, due to the -2 slope between 40 and 200 Hz, the bandwidth specification of 50-100 Hz should not be a problem in the controller design.

Also, an FRF measurement has been performed on the prototype, in the same way as described for the actuator design. The results show a strong similarity with the FEM model. The amplitudes and slopes match, and the eigenmodes only differ about 10 % in frequency. However, the 4^{th} mode is strongly present in the measured FRF, whereas the 3^{rd} and 5^{th} modes are more damped. The latter is probably due to coulomb friction in the ball contacts, which was not considered in the model.

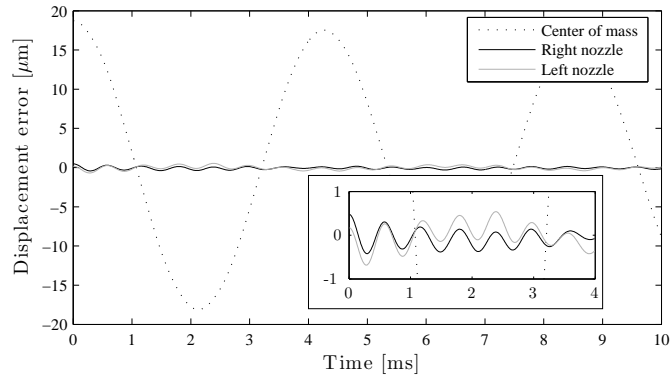


Figure 6.15: Modeled transient response of nozzles when reversing the carriage.

The state space model is also used to simulate the time response of the printhead position for a reversing carriage. The input acceleration ($a_x = 5 \text{ m/s}^2$) is simulated by applying a force on the leaf spring ends. The outputs of the model, the nozzle positions and the printhead's center of mass with respect to the carriage are shown in Figure 6.15. The V-form leaf spring is found to be effective in suppressing the nozzle displacements. The maximum deflection is $< 1 \mu\text{m}$, which is a factor 20 less than the deflection of the center of mass.

6.6 Thermal Analysis

Temperature measurements have been carried out on the experimental setup to examine the effects of a heated printhead in the new design. The test setup is shown in Figure 6.16.

First, a measurement under steady state conditions has been performed where the printheads are heated to $60 \text{ }^\circ\text{C}$. In the second measurement, a constant airflow

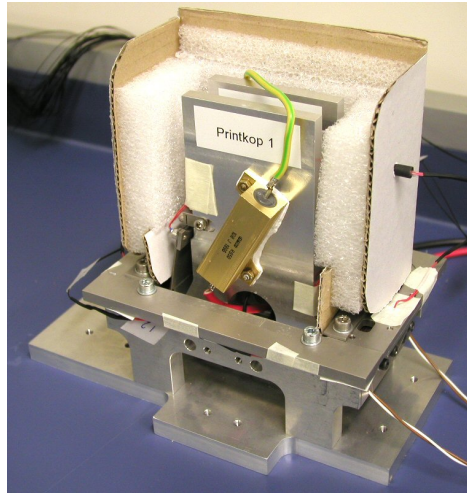


Figure 6.16: The testing setup with an isolating box opened.

of $1 \pm 0.1 \text{ m/s}$ is guided along the setup in x -direction by using an air fan to simulate working conditions when the carriage is moving over the guiding rail. Because convection is dominant over radiation, the temperature values can be scaled linearly to the case that the printheads are $130 \text{ }^\circ\text{C}$. This scaling is important for the CCD location which may not exceed $70 \text{ }^\circ\text{C}$ to operate properly.

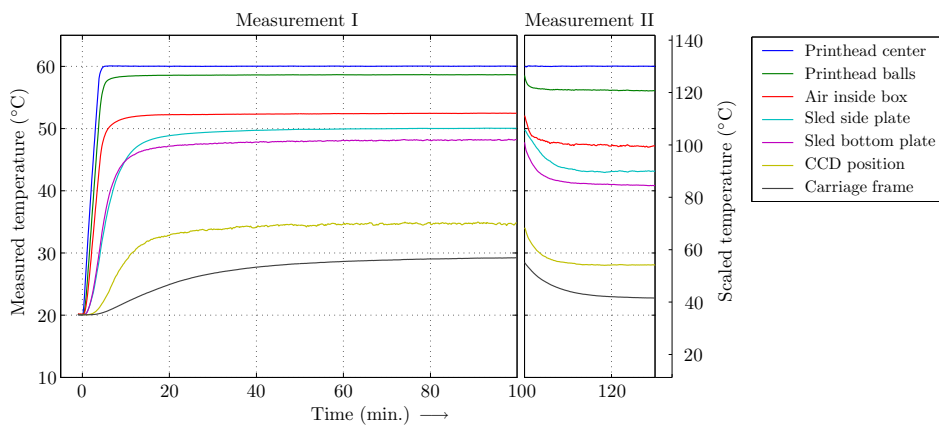


Figure 6.17: Temperature measurements: (I) is measured under still air conditions, whereas in (II) a 1 m/s wind flow is guided along the setup. The legend order corresponds to the temperature level.

In the second measurement, the wind flow of 1 m/s causes a forced heat convection. This is most interesting at the sensor position and the carriage, where the thermal shrinkage will cause positioning errors of the printhead. The scaled temperature drop ΔT for all components except the dummy is about $15 \text{ }^\circ\text{C}$ as shown

in Figure 6.17. An indication of the thermal drift is given by

$$\Delta p = \Delta T \alpha d \quad (6.14)$$

where d is the distance between the considered components, and α the CTE. For the x -, y - and z -direction the thermal drifts are estimated in Table 6.8.

Table 6.8: Estimated thermal drift Δp of the printhead in x -, y - and z -direction.)

Dir.	Caused by	Distance d [mm]	CTE α [$\mu\text{m}/\text{mK}$]	Δp [μm]	
x	Carriage	Printhead \rightarrow printhead:	max. 140	12 (Steel)	25.2
y	Sensor mount	CCD $\rightarrow T_c$ printhead:	25	20 (Mean)	7.5
z	Leaf springs	Bottom plate \rightarrow carriage:	25	12 (Steel)	4.5

The thermal drifts in y - and z -direction are within the specifications and besides, all the printheads in the carriage will have about the same drift by which the alignment error will be even less. Drift in x -direction can be compensated for by adjusting the jet-timing. Based on the experiments on the design, it is expected that the printhead alignment errors also can be kept within the specifications under high temperature printing conditions.

Chapter 7

Active Printhead Alignment Implementation

This chapter is based on [9, 11] and shows the system identification, controller design and experimental results of the experimental setup described in Chapter 6. The chapter is concluded with a discussion on the active printhead alignment concept.

7.1 Experimental Setup

In Figure 7.1, the experimental setup is shown. It consists of the alignment mechanism, the amplifier, the string tension device and data acquisition devices. In Figure 7.2, the alignment mechanism is shown containing two printheads staggered beside of each other in the carriage. At the frontside, where the string passes the alignment mechanism, two sensors can be mounted.

In WFPS, the carriage follows the shape of the guidance which can be seen as a disturbance acting on the printheads. For the active printhead alignment method, the trajectory of each printhead is a fixed distance with respect to the string which is a regulation problem. For the sake of simplicity, in this work we do the opposite: the carriage is fixed to the printer frame (table) and the deviation of the guidance is seen as the trajectory to be followed which is a tracking problem. This difference is illustrated in Figure 7.3.

The main difference with the regulation problem is that inertial forces are present for the tracking problem leading to higher actuation forces. For the controller design this does not matter because the system dynamics remain the same.

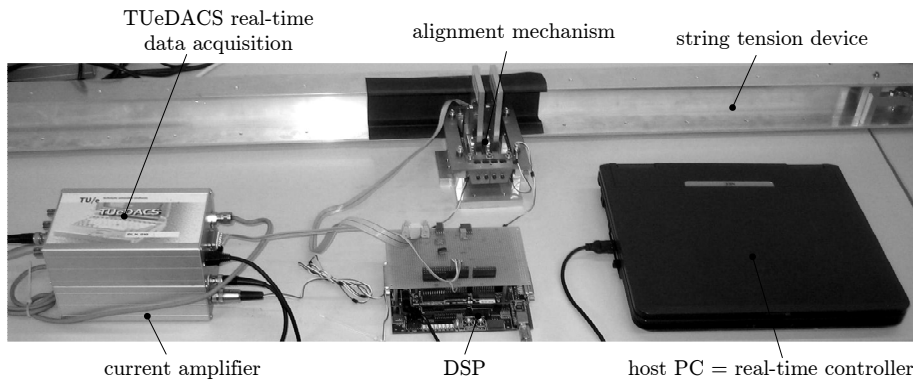


Figure 7.1: Picture of the complete setup including, the alignment mechanism, the amplifier, the string tension device and data acquisition devices.

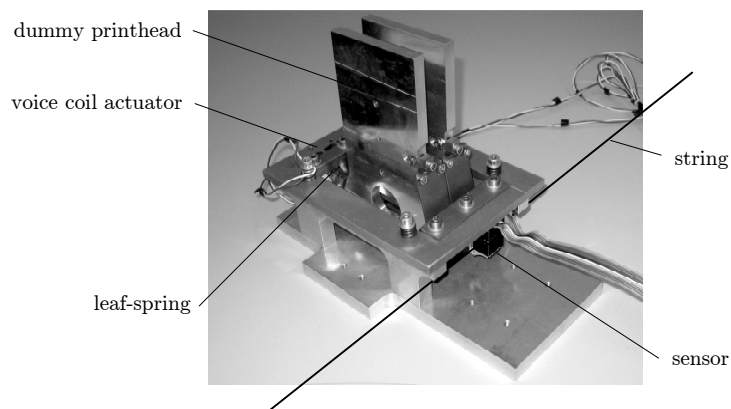


Figure 7.2: The experimental setup of the alignment mechanism.

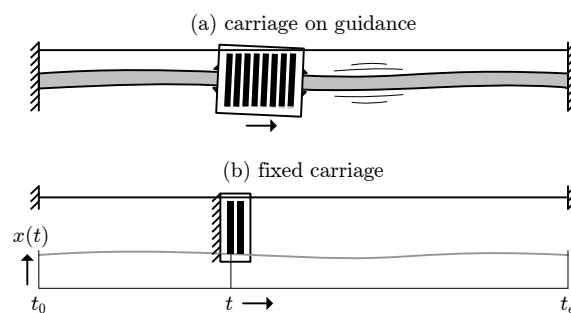


Figure 7.3: The actual situation in a printer is shown in (a). For proof-of-concept, the setup as shown in (b) is used. The carriage stands still and must follow a certain trajectory representing the printhead's misalignment.

First the alignment mechanism will be identified which is used to design a feedback controller for. Finally, closed loop experiments are carried out to assess the printhead alignment performance.

7.2 System Identification

In Figure 7.4, the frequency response function is shown including the string position sensor as described in Chapter 5. The plant's input is a voltage signal driving the current amplifier which is proportional to the force generated by the voice coil actuator and the plant's output is the string position sensor measurement.

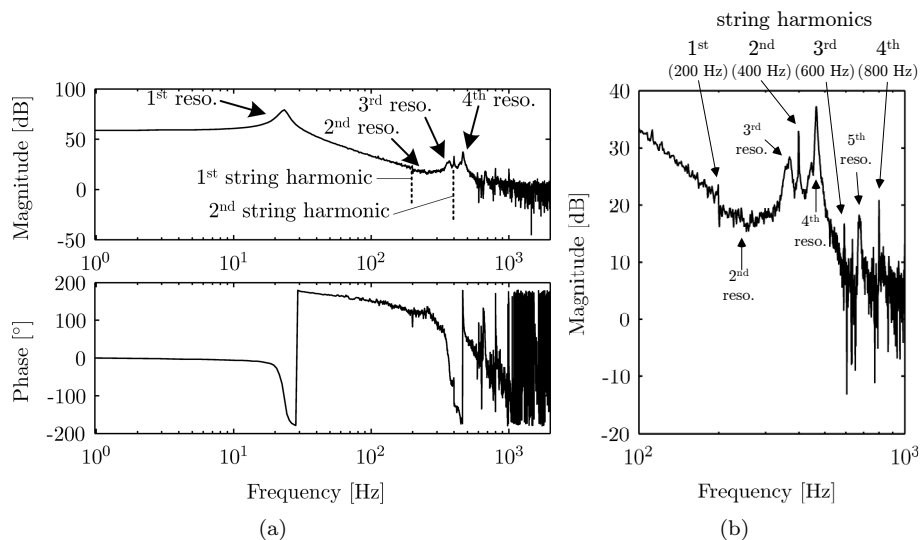


Figure 7.4: (a) Bode plot of the frequency response function (FRF) of the alignment mechanism $P(j\omega)$ in $\mu\text{m}/\text{V}$. The four lowest resonances are indicated. Furthermore, string harmonics are also visible, because the string is excited by the actuator via the air and/or the printer frame. These harmonics are visible because no harmonics filter was included yet for the plant FRF measurement, (b) magnitude plot of Figure 7.4(a) zoomed in.

The system can be approximated by a mass-spring-damper system with a resonance frequency at 28 Hz and some eigenmodes above 200 Hz. Also, the string harmonics are slightly visible which indicate that the string is excited by the actuator via the air and/or printer frame. Furthermore, the closed loop system contains a total time delay of 3.5 samples which is about 0.9 ms at a sampling frequency of 4000 Hz. The time delay is mainly caused by the sensor. First the light intensity is captured during one sample, the next sample the data is copied to the memory of the DSP where it is being processed to compute the string's po-

sition. In total the sensor causes about 2.5 samples delay. The remaining sample of time delay is caused by two D/A conversions. A time delay of 0.9 ms limits the bandwidth in the current setup to about 50 Hz (frequency where there is 15° phase loss due to time delay). If the string position computations and the motion controller would be integrated into a single DSP, or if another sensor with less time delay would be used and/or a higher sampling frequency would be used, then a bandwidth of 100 Hz could be easily obtained. A higher bandwidth results in a higher gain at lower frequencies, which results in a better disturbance attenuation.

7.3 Controller Design

The control scheme with a feedback controller $C_{fb}(s)$ and a feedforward controller $C_{ff}(s)$ is shown in Figure 7.5. A feedback controller is designed to attenuate disturbances at low frequencies, e.g. guidance and printer frame vibrations. Furthermore, a feedforward controller is designed which compensates for static disturbances which act on the system while the carriage moves across the guidance, e.g. the guidance deviation and manufacturing tolerances of the carriage.

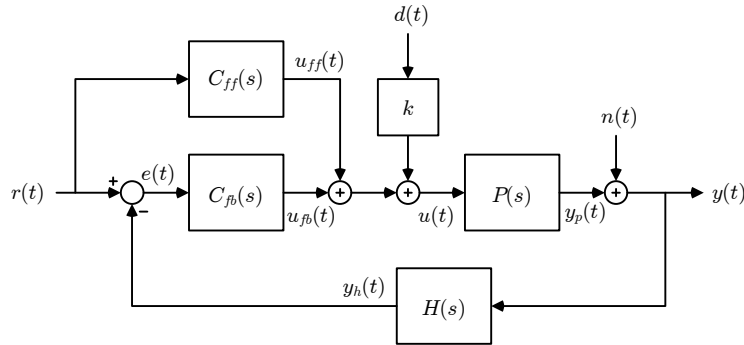


Figure 7.5: Control scheme for the alignment mechanism containing a feedback controller $C_{fb}(s)$, a feedforward controller $C_{ff}(s)$ and a harmonics filter $H(s)$. The string vibrations, sensor noise and guidance vibrations are modeled as disturbance $d(t)$.

The signal $r(t)$ is the reference in μm , $e(t)$ is the error in μm , $u_{fb}(t)$ and $u_{ff}(t)$ are the feedback and feedforward controller output in V respectively, $u(t)$ is the total control effort in V, $y_p(t)$ is the printhead position in μm , $y(t)$ is the measured string position in μm , $y_h(t)$ is the output in μm of the harmonics filter $H(s)$, $n(t)$ is the disturbance containing string oscillations and sensor noise in μm , and $d(t)$ is the guidance position in μm . The guidance position is an input disturbance which acts on the printhead via the leaf spring stiffness $k_y = 6 \cdot 10^{-3} \text{ N}/\mu\text{m}$. The scaled stiffness becomes $k = \frac{k_y}{k_{amp}k_{motor}} = \frac{6 \cdot 10^{-3}}{1.0 \cdot 3.85} = 1.6 \cdot 10^{-3} \text{ V}/\mu\text{m}$ where k_{amp} is the amplifier constant in A/V and k_{motor} is the motor constant in N/A.

7.3.1 Feedback Controller

The feedback controller will be designed for the system dynamics $P(s)$ merged with the harmonics filter $H(s)$ which is also located in the control loop. The feedback controller is tuned using an optimization aided loop shaping tool (see Appendix C, [7]). The advantage of loop shaping is that the measured open loop FRF can be used directly to design a controller. Matlab/Simulink in combination with a TUEdACS Qad interface is used to do closed loop experiments, see [90]. The realtime application is generated with RTW and runs on the host PC with RTAI Linux [61].

The designed controller is shown in Figure 7.6 and consists of:

- (i) a lead filter to obtain phase lead around the cross-over frequency (50 Hz), noted as bandwidth,
- (ii) a notch filter to suppress the resonance around 461 Hz,
- (iii) a low pass filter to reduce the disturbance amplification above the bandwidth, and
- (iv) a slant notch filter to increase disturbance attenuation below the bandwidth.

The parameters of these filters are shown in Table 7.1.

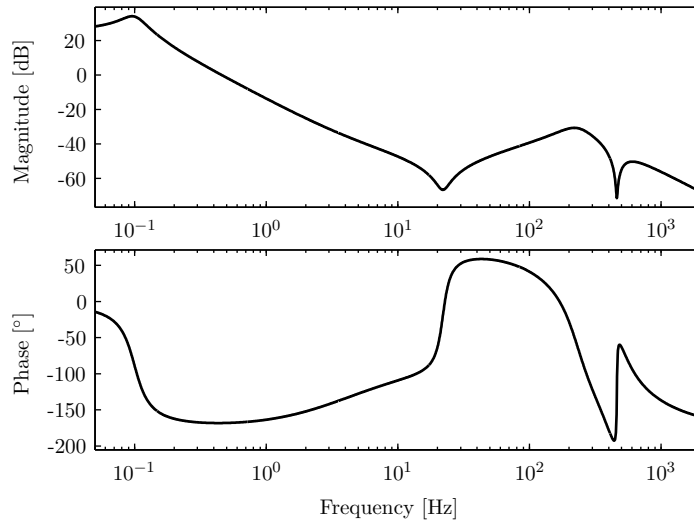


Figure 7.6: Bode plot of the controller containing a lead filter, a low pass filter, a notch filter and a slant notch filter to increase gain for low frequencies.

A slant notch is used instead of an integrator because the location of the first resonance is close to the bandwidth frequency resulting in poor disturbance attenuation with an integrator. Conversely, the slant notch causes less phase lag near the bandwidth and increases the gain much faster such that better distur-

Table 7.1: Controller parameters

Filter	Parameters
Gain	20
Lead filter	pole 300 Hz, zero 4 Hz
Notch filter	poles 461 Hz, damping 0.3, zeros 461 Hz, damping 0.01
Low pass filter	poles 230 Hz, damping 0.3
Slant notch	poles 0.1 Hz, damping 0.2, zeros 22 Hz, damping 0.1

bance attenuation is obtained below the bandwidth. An alternative to using a slant notch is using a double integrator, however, servo errors due to e.g. when reaching the end stroke of the printhead guidance will blow up the controller output very fast. Experiments showed that the system becomes unstable when an end stroke is reached.

The bode plot of the loop gain $H(j\omega)C_{fb}(j\omega)P(j\omega)$ is shown in Figure 7.7 showing that the bandwidth is 50 Hz. The bode plot of the sensitivity function $(1 + H(j\omega)C_{fb}(j\omega)P(j\omega))^{-1}$ is shown in Figure 7.8(a) showing that the maximum sensitivity magnitude or modulus margin is about 7 dB. The Nyquist plot is shown in Figure 7.8(b). The open loop passes the point -1 on the right side, hence, given the fact that the open loop system is stable, the closed loop system is robustly stable. The gain and phase margin are 6.4 dB and 42° respectively.

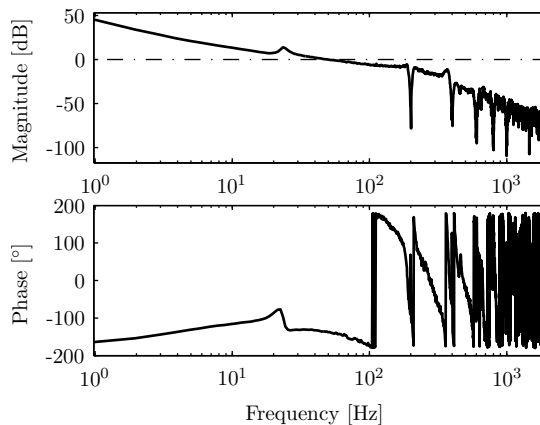


Figure 7.7: Bode plot of the loop gain of the system. The loop gain crosses the 0 dB line at 50 Hz which is denoted as the bandwidth of the closed loop system.

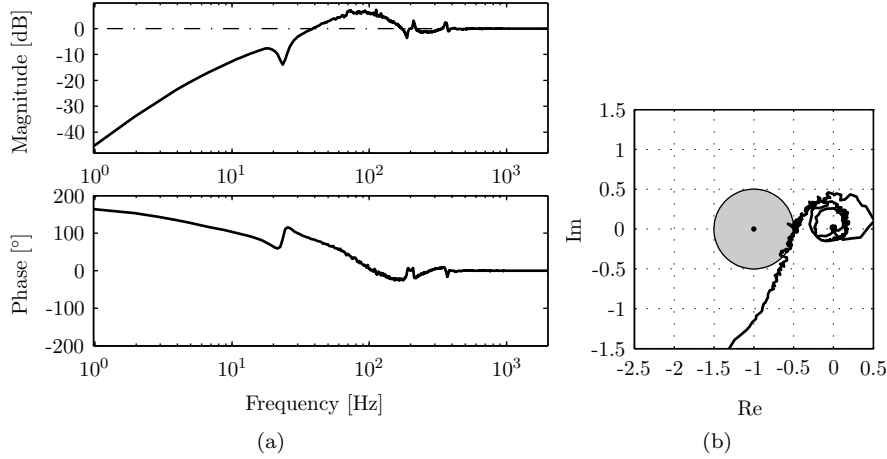


Figure 7.8: (a) Bode plot of the sensitivity function (b) Nyquist plot

7.3.2 Disturbance Rejection

According to Figure 7.5, the sensitivity for disturbances $d(t)$ can be described by

$$\frac{\mathcal{L}\{y_h(t)\}}{\mathcal{L}\{d(t)\}} = \frac{kP(s)H(s)}{1 + C_{fb}(s)P(s)H(s)} \quad (7.1)$$

In Figure 7.9, the sensitivity of the printhead position to disturbances (7.1) is shown. It shows a maximum sensitivity to disturbances around 22 Hz caused by the poles of the slant notch, however, the slant notch provides a better disturbance attenuation at lower frequencies. With less time delay in the loop, the bandwidth could be increased which would improve the disturbance rejection around a frequency of 22 Hz. Suppose that the printhead would be fixed to the carriage, Figure 7.9 would be a horizontal line at 0 dB, hence, this figure shows the improvement in disturbance rejection due the active printhead alignment method.

7.3.3 Feedforward Control

No parametric feedforward, such as position, velocity and acceleration feedforward, is used because for the regulation problem in WFPS the trajectory is equal to zero. Nevertheless, the disturbance signal $d(t)$ acting on the system contains repetitive disturbances. These repetitive disturbances can be removed by using e.g. Iterative Learning Control (ILC). For more information about ILC, see e.g. [64]. The alignment mechanism is especially suited for this techniques because

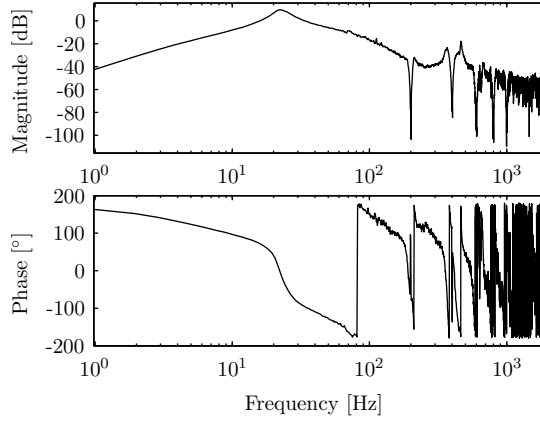


Figure 7.9: Sensitivity for disturbances $d(t)$ from the carriage with a feedback controller.

most disturbances are of static nature, e.g. the non-straightness of the guidance, and the carriage will repeat the same movement over and over.

The goal is that each printhead should move along a straight line with respect to the printer frame, hence printheads will not move in y -direction. The carriage will move with respect to the printheads in y -direction which results in bending the leaf springs that attach the printheads to the carriage. In theory, the resulting feedforward obtained via ILC resembles only a stiffness feedforward which compensates for bending of the leaf springs. In practice, also parasitic dynamics are taken into account. In Figure 7.10, the repetitive and non-repetitive disturbances are shown for a 10 Hz sine with an amplitude of $50 \mu\text{m}$ between 0.5 s and 2.5 s as a reference.

The maximum amplitude of the repetitive disturbance is $13 \mu\text{m}$ which can be removed by ILC. In Figure 7.11(a), the convergence of ILC is shown. A robustness-filter with a cut-off frequency of 150 Hz is used. The learned feedforward signal is shown in Figure 7.11(b). The standard deviation of the error converges to about $1 \mu\text{m}$ which matches with the standard deviation of the non-repetitive error as shown in Figure 7.10.

In Figure 7.12, the power spectral density is shown of the error signal before and after applying ILC. Below the cut-off frequency of the robustness filter the error is decreased significantly. The remaining error is a broadband noisy signal with some spikes caused by the harmonics filter. These spikes are required for robustness to string harmonics. If some harmonics would be present, these spikes would be less deep, however, they will not dominate the error signal.

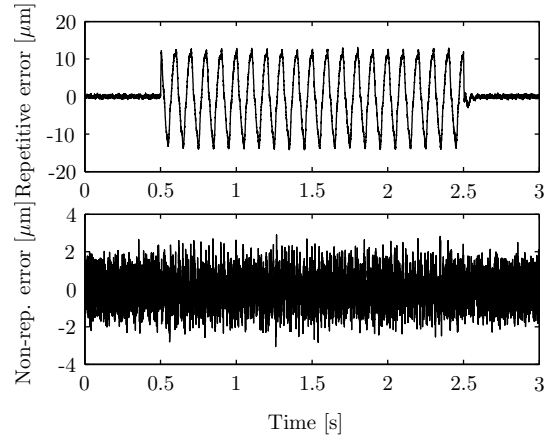


Figure 7.10: Top figure: repetitive error (average of 10 measurements), bottom figure: difference of one measurement compared to the repetitive error.

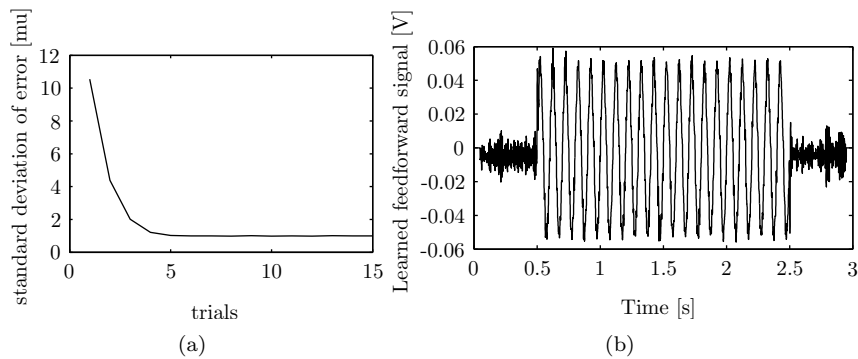


Figure 7.11: (a) Convergence of ILC, (b) Learned feedforward signal.

7.4 Experimental Results

In this section, the tracking performance of the alignment mechanism is shown. Furthermore, the system is exposed to disturbances to show the disturbance attenuation ability.

7.4.1 Tracking

In Figure 7.13, a measurement is shown where a 10 Hz sine is tracked using a feedback controller in combination with ILC. As can be seen, the tracking accuracy is about $2 \mu\text{m}$ where the remaining error is mainly non-repetitive. The

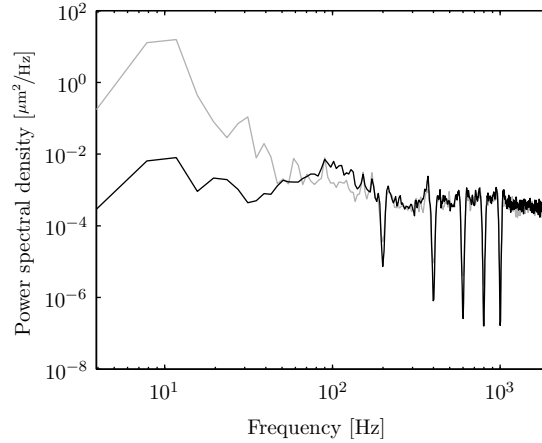


Figure 7.12: Power spectral density of the error signal with only a feedback controller (grey line) and with ILC feedforward (black line).

corresponding power spectral density is shown in Figure 7.12.

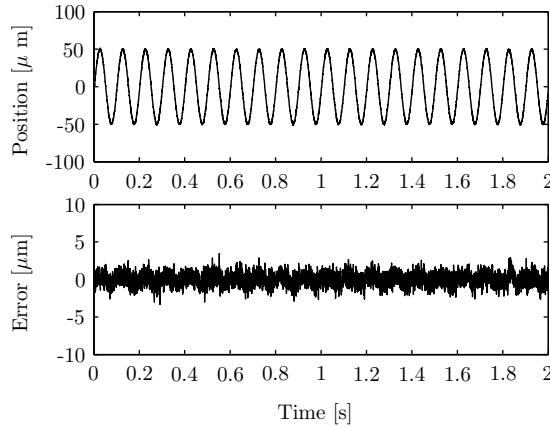


Figure 7.13: Experiment where a 10 Hz sine is tracked using feedback control in combination with ILC.

The magnitude of the sensitivity function as shown in Figure 7.8(a) is about -15 dB at 10 Hz which would result in a servo error of 10 μm for a reference with an amplitude of 50 μm . This agrees with the repetitive error as shown in Figure 7.10. The ratio of the servo error and the position reference as shown in Figure 7.13 is about a factor of 25 \approx -30 dB, hence, the addition of ILC results in 15 dB reduction of the servo error for the given reference.

7.4.2 Tracking under Influence of Disturbances

Due to external disturbances acting on the printer or parasitic dynamics due to for instance the moving or reversing carriage, a disturbance force can act on the carriage. To address this, the carriage is excited with an impulse disturbance using a hammer which is regarded as the worst-case disturbance. The results are shown in Figure 7.14.

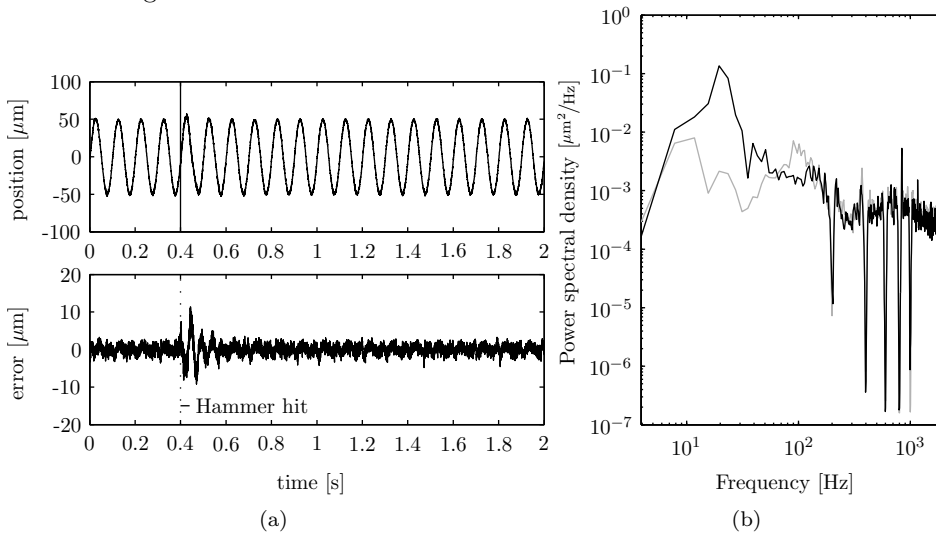


Figure 7.14: (a) Response of the alignment mechanism for an impulse disturbance at $t = 0.4$ s, (b) power spectral density of the error signal (black line) showing a peak around 22 Hz, the first eigenmode of the printhead. The grey line is the power spectral density without disturbance as shown in Figure 7.13.

A maximum deviation of 11 μm and a settling time of about 0.1 s is observed. The frequency content of the transient dynamics are concentrated around 22 Hz, the first eigenmode of the printhead. In a real printer, during reversing of the carriage the biggest disturbance is expected because carriage (de)acceleration excites printer frame dynamics. While reversing the carriage nothing is printed, so the disturbance shown in Figure 7.14 is not likely to occur during printing.

In Figure 7.15, the string is excited by hitting the string resulting in harmonic vibrations of the string. These harmonic vibrations are visible in Figure 7.16. The 1st, 2nd, and 4th string harmonic dominate the string oscillation. These harmonics are attenuated well by the harmonics filter.

The maximum amplitude of the string oscillation is 15 μm . From experience we know that this amplitude is about the maximum that can be induced by airflow or frame dynamics. The impulse disturbance on the string induces transient dynamics of the harmonics filter which are gone after 0.1 s. The transient response stays below 10 μm after the string hit.

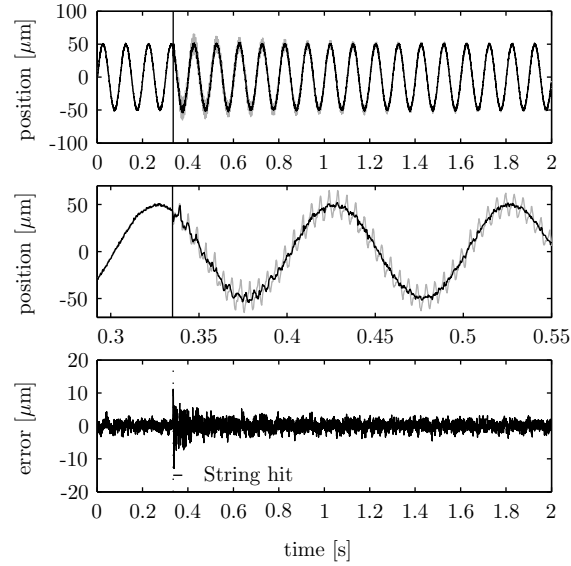


Figure 7.15: Top figure: the printhead follows a sine of 10 Hz while the string is excited, middle figure: zoom of top figure. Black line: harmonics filter output, grey line: sensor measurement. Bottom figure: difference between the harmonics filter output and the trajectory. The transient dynamics of the harmonics filter are gone 0.1 s after the hit, hence the trajectory is tracked well while the harmonics of the string damp slowly.

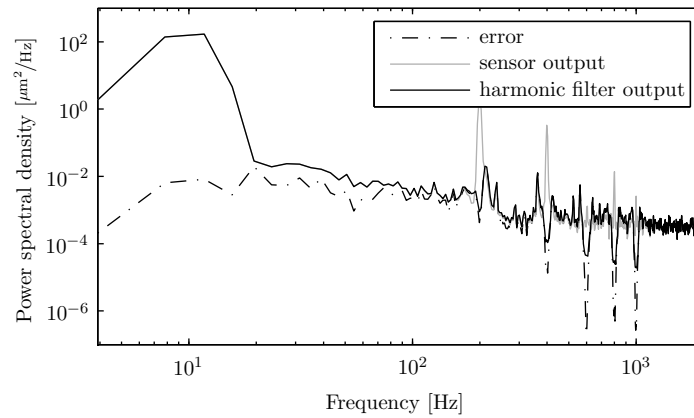


Figure 7.16: Power spectral density of the error, the sensor output and the output of the harmonic filter.

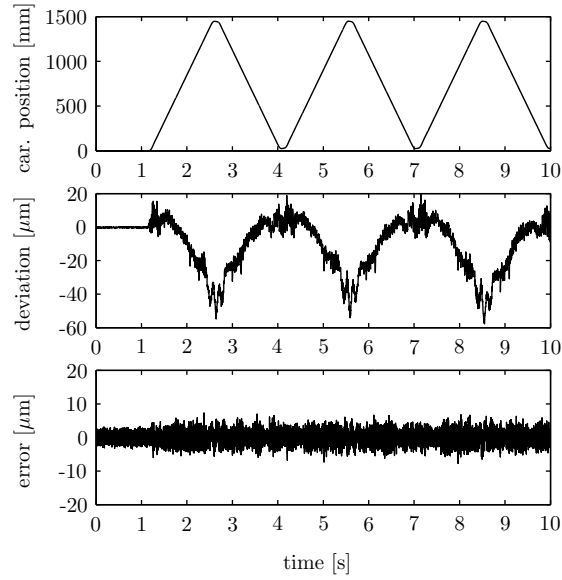
7.4.3 Tracking of a Carriage Trajectory Measured at a WFPS

The experimental setup is also subjected to measurement data from a real WFPS. The carriage in the WFPS moves with 1 m/s across a guidance over a distance of 1.45 m. The position is measured using laser interferometry and quadrangle reflectors placed on the carriage resulting in a 6 DOF measurement of the carriage position. An accuracy below 1 μm is obtained if strict requirements regarding temperature fluctuations of the environment are satisfied. The deviation of the carriage in paper transport direction is used as trajectory for the experimental setup. The feedback controller without feedforward is used to track this trajectory. In Figure 7.17, the results are shown. The maximum absolute error is equal to 7.7 μm and the standard deviation is equal to 1.7 μm .

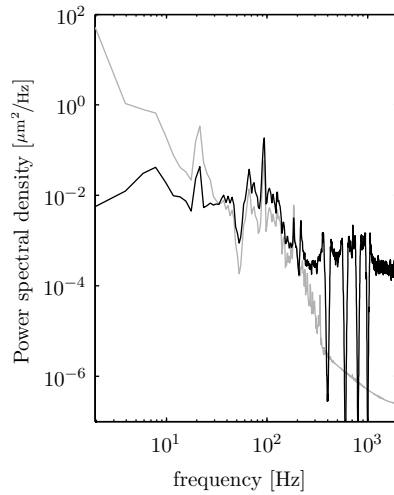
The trajectory shows that an eigenmode with a frequency of 8 Hz is excited during a reversal. Because this frequency is below the bandwidth of the controlled system it is attenuated. At 20 Hz an oscillation is present over the whole trajectory caused by roll bearing eccentricity (speed 1.0 m/s, roll bearing diameter 16 mm: $\frac{1.0}{0.016\pi} = 20$ Hz). Also this disturbance is attenuated well. The main cause of the error is a 90 Hz eigenmode. This eigenmode is also amplified (see Figure 7.8) because it is just above the bandwidth. To attenuate this, a bandwidth above 90 Hz would be desirable.

7.4.4 Error Budget Verification

In Table 7.2, a summation of the expected error budget during printing is shown. For the filter distortion it is assumed that the guidance has a maximum amplitude of 100 μm with an observed frequency of 10 Hz and that the maximum amplitude of all harmonics together is 15 μm with an effective attenuation of 20 dB including transient induced errors. In general, thermal drift will be about the same for all printheads, hence, mutual alignment will be distorted much less. For the thermal gradients it is assumed that during one carriage movement from one side to the other, the difference in thermal drift between all sensor mountings is about 3 °C assuming that the material is aluminum and the sensor-printhead distance is 20 mm. The deviation 3σ of the total error is 8.1 μm which can be considered to be the worst-case error which is within the specification of 10 μm . When disturbances are minimal, the maximum deviation is 2 μm as shown in Figure 7.13.



(a)



(b)

Figure 7.17: (a) Experiment with measurement data from a real WFPS. Top figure: carriage position, middle figure: deviation of the carriage in paper transport direction, bottom figure: tracking error of the printhead, (b) power spectral density of the reference (grey line) and of the error signal (black line).

Table 7.2: Error budget estimation.

Error source	σ [$\mu\mathbf{m}$]
sensor noise	0.8
harmonics filter, signal distortion	1.0
harmonics filter, residual of harmonics	1.5
servo error of fb+ff controller	1.0
thermal drift	1.5
total (assuming uncorrelated white noise)	2.7

7.5 Discussion

A printhead alignment mechanism has been designed and tested. The mechanism, consisting of a leaf spring guided sled with a voice coil actuator and string sensor, is designed by means of FEM simulations. In this approach, the system's dynamic behavior has been examined and optimized.

The design allows for easy printhead replacement, combined with an exact constraint sled connection, by which the minimal hysteresis provides a high reproducibility. Most components can be made by common manufacturing processes, which saves cost. From the improvements of individual printhead positioning, a better print quality of WFPS can be expected with the new printhead alignment system.

By using active control, the accuracy is improved while confining cost of production. The worst-case performance has been determined by exciting the system with disturbances which represent manufacturing tolerances and dynamics of the printhead, printhead mounting, carriage, guidance and printer frame. A maximum error of $8.1 \mu\text{m}$ has shown to be the worst-case performance, where $2 \mu\text{m}$ accuracy is the nominal performance. The worst-case performance is below the specified $10 \mu\text{m}$, hence the concept is feasible.

For this printhead alignment mechanism design, the bandwidth is limited to 50 Hz due to the total amount of time delay of 0.9 ms in the present setup. A faster data-acquisition/signal processing unit for the string position signal will open the way to higher bandwidth and even better performance.

Part III

Energy Buffered Carriage Reversal

Chapter 8

Reversal Mechanism Design

In this chapter, based on [10] and [81], a new design of a carriage drive for WFPS is proposed. The new drive reverses the carriage by buffering the kinetic energy of the carriage resulting in a fast reversal and a high energy efficiency for higher productive WFPS. A spring is used as an energy buffer and a clutch is designed which engages smoothly enabling reversal at arbitrary moments. This way, only a small carriage drive is needed to overcome the friction forces acting on the carriage.

8.1 Introduction

In Chapter 3, the relation between design parameters and productivity was investigated. The two main parameters to increase productivity are the amount of nozzles and the jet frequency of these nozzles which increases the mass and speed of the carriage. As concluded in Chapter 3, this mass and speed increase results in an efficiency decrease. Printing can only be carried out at a constant speed, because the carriage speed affects the jetting behavior and thus the print quality. During reversal of the carriage, nothing can be printed, hence, the reversal time has to be minimized. To achieve this for higher productive WFPS, the power of the conventional drive can be scaled, which is expensive and energy inefficient due to dissipation of kinetic energy during carriage reversal. It would be advantageous to temporarily store the kinetic energy into potential energy and reuse it to accelerate the carriage again in opposite direction as shown in Figure 8.1.

Buffering energy is an active research field including mechanical (springs, fly-wheels) [15, 86], pneumatic [58] and electric [2] concepts. Our research focusses on the use of a mechanical spring, because:

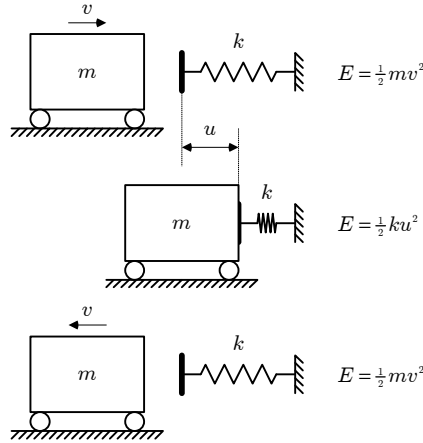


Figure 8.1: The principle of carriage reversal using a mechanical spring as an energy buffer where E is the sum of the kinetic and potential energy.

- (i) it has a small building volume,
- (ii) it has low energy dissipation during reversal and foremost
- (iii) the kinetic energy is reversed as fast as possible which is inherent to the working principle of a spring.

In this chapter, we present a new design to drive the carriage for WFPS. The drive consists of a small motor to overcome frictional forces and a so-called drive-aid. The drive-aid is an integrated design of a spring to buffer the kinetic energy and a clutch to be able to reverse at arbitrary moments. To determine the feasibility of this concept, an experimental setup is designed and built to validate the concept with experiments as presented in Chapter 9.

8.2 Concept Exploration

As a starting-point for the drive-aid, we assume that the carriage mass and speed is doubled with respect to conventional WFPS, i.e. $m_c \approx 5$ kg and $v_c \approx 2$ m/s. From Chapter 3 it follows that it is preferred that printing time should be dominant over reversal time. When requiring a relative reversal time $t_{\%}$ of at most 20 % for a stroke of $x_c = 1$ m, then we obtain a reversal time of 0.1 s. Design consideration for the drive-aid are:

- carriage reversal should be possible at arbitrary moments. This implies the need for a clutch in the design.
- a smooth introduction of forces is preferred over high impact forces to reduce wear and parasitic dynamics.

- the number of additional motors and their power requirement should be kept at a minimum to keep the cost price low.
- the moving mass of the drive-aid should be kept as low as possible which reduces impact forces, reduces required motor power, increases eigenfrequencies.
- simplicity of the construction results in a lower cost price.

While keeping these design considerations in mind, we present a few concepts leading to the concept that is chosen to be worked out.

Concept 1: the first concept is equal to Figure 8.1 made bidirectional. No additional motor is required for this concept (beside of a small carriage drive) at the cost of a fixed stroke and impact forces when engaging the spring.

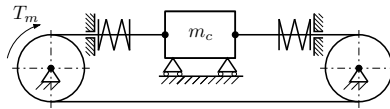


Figure 8.2: Bidirectional fixed-stroke concept.

Concept 2: the second concept is similar to concept 1 except for the varying end stops. The stroke of the carriage is made variable at the cost of two additional motors. These actuators could be for example two spindles which are self-breaking. The disadvantage of impact forces when engaging the spring remain.

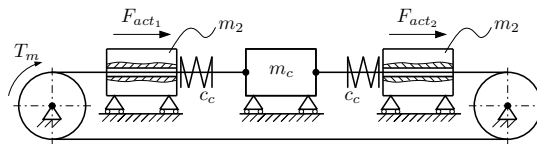


Figure 8.3: Movable end-stops concept.

Concept 3: to reduce the size of concept 2, only one end-stop is used while introducing a bidirectional spring in series with a clearance. During printing, the drive-aid follows the carriage and during carriage reversal, the drive-aid is stopped within the clearance and the spring is engaged consecutively. By choosing the length of the clearance, the required power of the drive-aid motor can be chosen to slow down and speed up the drive-aid. An additional advantage is that the drive-aid is decoupled from the carriage when it is in the clearance such that no disturbances act on the carriage.

Concept 4: in order to decrease the moving mass and volume, concept 3 is made rotationally. The conversion from a translational to a rotational concept introduces a lever which reduces the moment of inertia $J_2 = m_2 r^2$.

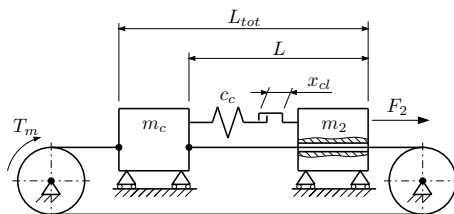


Figure 8.4: Concept with a bidirectional spring in series with a clearance.

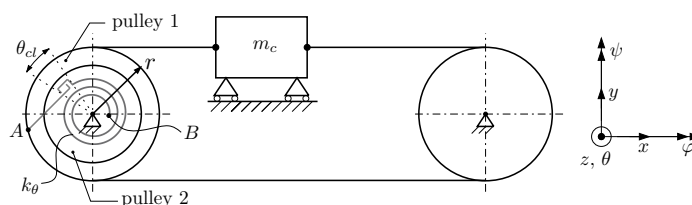


Figure 8.5: Rotational version of concept 3.

Because concept 4 is the most promising, this concept will be worked out. Before presenting the design of the prototype in the next section, first some critical issues will be described.

High Impact Forces

The zero stiffness of the clearance should gradually change into the required stiffness of the drive-aid (felt by the belt). Hence, the spring characteristic has a shape as shown in Figure 8.6.

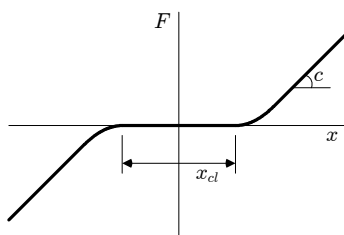


Figure 8.6: The spring characteristic as seen by the belt where the drive-aid is standing still. The zero stiffness part of the cam clearance is smoothly connected to the spring stiffness c felt by the belt to prevent peak forces at the transitions.

Many ways exist to accomplish this which are described in [81]. We choose to use a cam in combination with a cam roller as shown in Figure 8.7.

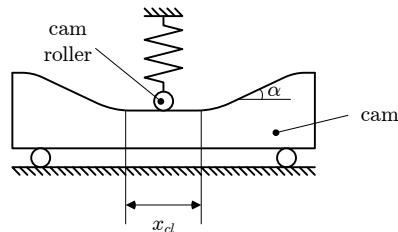


Figure 8.7: Cam and cam roller for gradually introduction of the spring force.

Self-Braking Clutch

To prevent that the additional drive-aid motor of concept 4 has to deliver the reaction force to reverse the carriage, it is preferable to make the clutch self-braking. For a force-locked clutch, the reaction force of the spring could be used to obtain a self-braking clutch. The cam slope angle α in Figure 8.7 can be chosen smaller than $\arctan \mu$ resulting in a self-braking clutch, where μ is the frictional coefficient of the clutch.

Form-Fit vs Force-Locked Clutch

Another way to keep the drive-aid still while reversing the carriage with a small additional motor is to make the clutch form-fit. Disadvantages of a form-fit clutch are however an additional synchronization problem and the introduction of impact forces when engaging the clutch. Both disadvantages makes the drive-aid design more complex, hence, a force-locked clutch design will be implemented.

8.3 Prototype Design

8.3.1 Overview

In Figure 8.8, the concept as presented in Figure 8.5 is illustrated. The drive-aid and the carriage are both driven by a small actuator. The drive-aid motor F_d controls the drive-aid's position and the carriage motor F_c compensates for friction forces acting on the carriage.

In Figure 8.8(a), both the drive-aid and the carriage have a speed of v_c during printing. When the carriage has to reverse direction, the drive-aid is brought to a standstill, shown in Figure 8.8(b), while the carriage is still moving with speed v_c . The drive-aid is brought to a standstill before the cam roller touches the slope of the cam such that the clutch will be engaged with a minimum of sliding to reduce

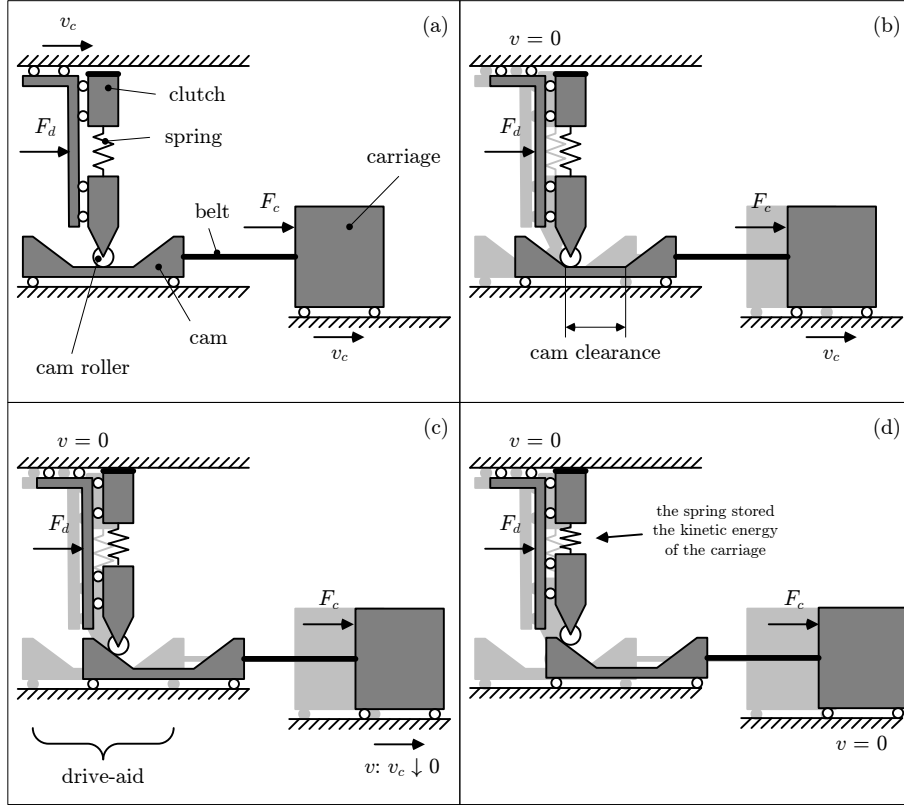


Figure 8.8: Working principle of the drive-aid. The drive-aid is designed rotationally, however, for comprehensibility, the drive-aid is drawn in a translational version. The figures describe half of the reversal process. For the other half, the images are reversed with reversed velocities.

wear. To achieve this with a small motor, the inertia of the drive-aid has to be minimized as much as possible. Next, the cam roller moves up the slope of the cam which engages the clutch and stores the kinetic energy of the carriage into the spring as shown in Figure 8.8(c). The slope of the cam is chosen such that the drive-aid is self-braking, so the reaction force does not have to be provided by the small drive-aid motor. The carriage keeps on slowing down until it comes to a standstill as shown in Figure 8.8(d). At this moment, all kinetic energy has been stored into the spring. Because the roller is still on the slope the inverse movement as described above will occur, eventually resulting in the situation as shown in Figure 8.8(a) with reversed velocities.

For clarity, the trajectory of the drive-aid and the cam clearance, which moves similar as the carriage, are shown in Figure 8.9. The clutch, and thus also the spring, is not engaged while the drive-aid's position stays within the cam clearance.

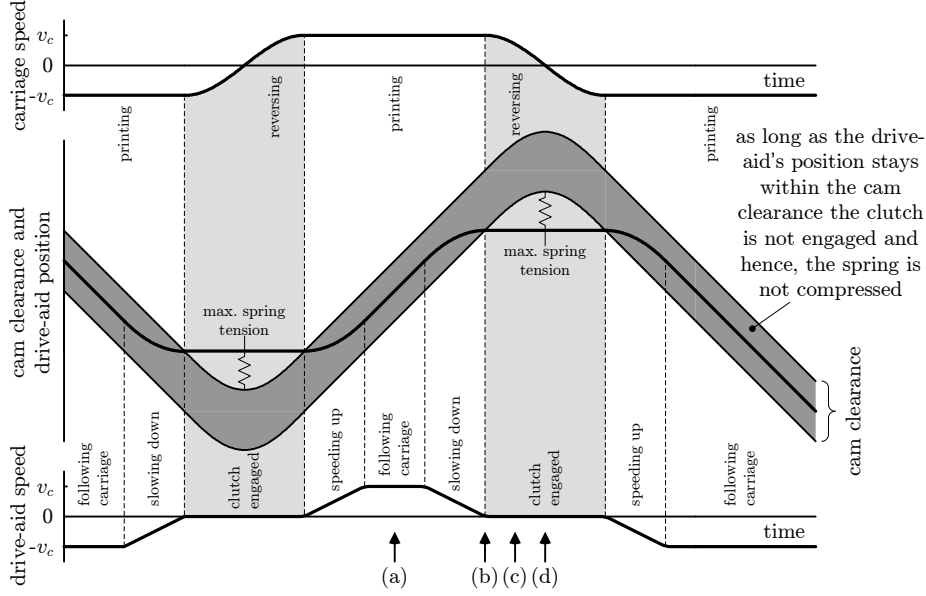


Figure 8.9: Trajectories, speeds and modes of both the drive-aid and the cam clearance. The moments sketched in Figure 8.8 are indicated. Also, the events that the spring tension is maximal are indicated. The carriage reverses with a sine shape which is inherent to a mass-spring system, whereas the drive-aid follows a 3rd order trajectory.

8.3.2 Reversal Time

The cycle time t_{cycle} is defined as the time of a stroke back and forth over a distance x_c :

$$t_{cycle} = 2t_r + 2\frac{x_c}{v_c} \quad (8.1)$$

where t_r is the reversal time in s and x_c is a distance that the carriage travels at a constant speed. The relative reversal time $t_{\%}$ becomes:

$$t_{\%} = \frac{2t_r}{t_{cycle}} = \frac{t_r}{t_r + \frac{x_c}{v_c}} \quad (8.2)$$

When the clutch has just been engaged, the system can be regarded as an undamped mass-spring system with spring stiffness c and mass m_c . The oscillation period T of this system is:

$$T = \frac{2\pi}{\omega} \quad (8.3)$$

where the eigenfrequency of the undamped mass-spring system ω is:

$$\omega = \sqrt{\frac{c}{m_c}} \quad (8.4)$$

Assuming that no other forces act on the system and the clutch is released after reversal at the same position where it has been engaged, the time passed is exactly equal to half the oscillation period. Hence, we can compute the required stiffness of the spring for a given carriage mass and required reversal time using (8.2), (8.3) and (8.4):

$$t_r = \frac{T}{2} = \frac{\pi}{\omega} \quad (8.5)$$

$$c = m_c \frac{\pi^2}{t_r^2} = m_c \left(\pi \frac{v_c}{x_c} \left(\frac{1}{t_{\%}} - 1 \right) \right)^2 \quad (8.6)$$

As an example, for $t_{\%} = 20\%$, $v_c = 2$ m/s, $x_c = 0.61$ m (0.61 m = 24", which is defined as the minimum paper width for WFPS) and $m_c = 5$ kg we obtain a reversal time $t_r = 0.076$ s and a spring stiffness $c = 8488$ N/m. We see that the absolute reversal time t_r only depends on the mass of the carriage and the stiffness of the spring and not on the carriage speed v_c which shows that the scalability regarding the carriage speed is much better than for a conventional carriage drive. That is, in a conventional drive, the kinetic energy to be reversed increases quadratic with the carriage speed resulting in $t_r \sim v_c^2$. Furthermore, regarding the mass of the carriage we have $t_r \sim \sqrt{m_c}$, whereas for a conventional carriage drive holds $t_r \sim m_c$.

8.3.3 Power Requirement

The position of the carriage $x(t)$ during reversal is:

$$x(t) = u \sin \omega t \quad (8.7)$$

$$\dot{x}(t) = u\omega \cos \omega t \quad (8.8)$$

$$\ddot{x}(t) = -u\omega^2 \sin \omega t \quad (8.9)$$

and the maximum spring elongation u becomes:

$$\frac{1}{2}cu^2 = \frac{1}{2}m_cv_c^2 \rightarrow u = \frac{v_c}{\omega} \quad (8.10)$$

From (8.5), (8.9) and (8.10) follows:

$$\max |\ddot{x}(t)| = \frac{\pi v_c}{t_r} \quad (8.11)$$

For the given values above, the maximum carriage acceleration becomes 83 m/s^2 . The maximum force provided by the spring is:

$$\max |F(t)| = m_c \max |\ddot{x}(t)| \quad (8.12)$$

(or $\max |F(t)| = cu$) resulting in 413 N.

The required mechanical power $P_{mech}(t)$ can be computed as follows:

$$P_{mech}(t) = F(t)\dot{x}(t) = m_c\ddot{x}(t)\dot{x}(t) \quad (8.13)$$

The RMS-value of $P_{mech}(t)$ over one cycle becomes:

$$\begin{aligned} P_{mech}^{RMS} &= \sqrt{\frac{1}{t_{cycle}} 2 \int_0^{t_r} P_{mech}(t)^2 dt} \\ &= \pi \sqrt{\frac{1}{8} \frac{m_c v_c^3 (1 - t\%)^2}{x_c \sqrt{t\%}}} \end{aligned} \quad (8.14)$$

assuming no energy loss due to friction. This result is valid for a sine-shaped reversal trajectory. For a second order profile, the result would be:

$$P_{mech,2}^{RMS} = \sqrt{\frac{4}{3} \frac{m_c v_c^3 (1 - t\%)^2}{x_c \sqrt{t\%}}} \quad (8.15)$$

which only differs by a factor of $\frac{P_{mech,2}^{RMS}}{P_{mech}^{RMS}} = \frac{4\sqrt{2}}{\pi\sqrt{3}} \approx 1.04$. We observe that $P_{mech}^{RMS} \sim m_c v_c^3$ which means that the required power increases by a factor of 16 if both the mass and speed of the carriage is doubled. Variables x_c and $t\%$ have to remain equal for the higher productive WFPS, so we cannot use these parameters to decrease P_{mech}^{RMS} .

8.4 Design of a Prototype

For the concept shown in Figure 8.8, a prototype has been designed and built to investigate the feasibility of this concept. The main design challenges are: (i) the design of a torsional spring in combination with an angular clearance, and (ii) the design of a clutch which is engaged electromechanically with a small motor. The concept has been designed rotationally which has the advantages that:

- (i) a lever is introduced which reduces the drive-aid's inertia felt by the belt,
- (ii) all parts share the same rotational axle resulting in a compact design.

In Figure 8.10, Figure 8.11, and Figure 8.12, the drive-aid is assembled in steps. A description of each step is given below:

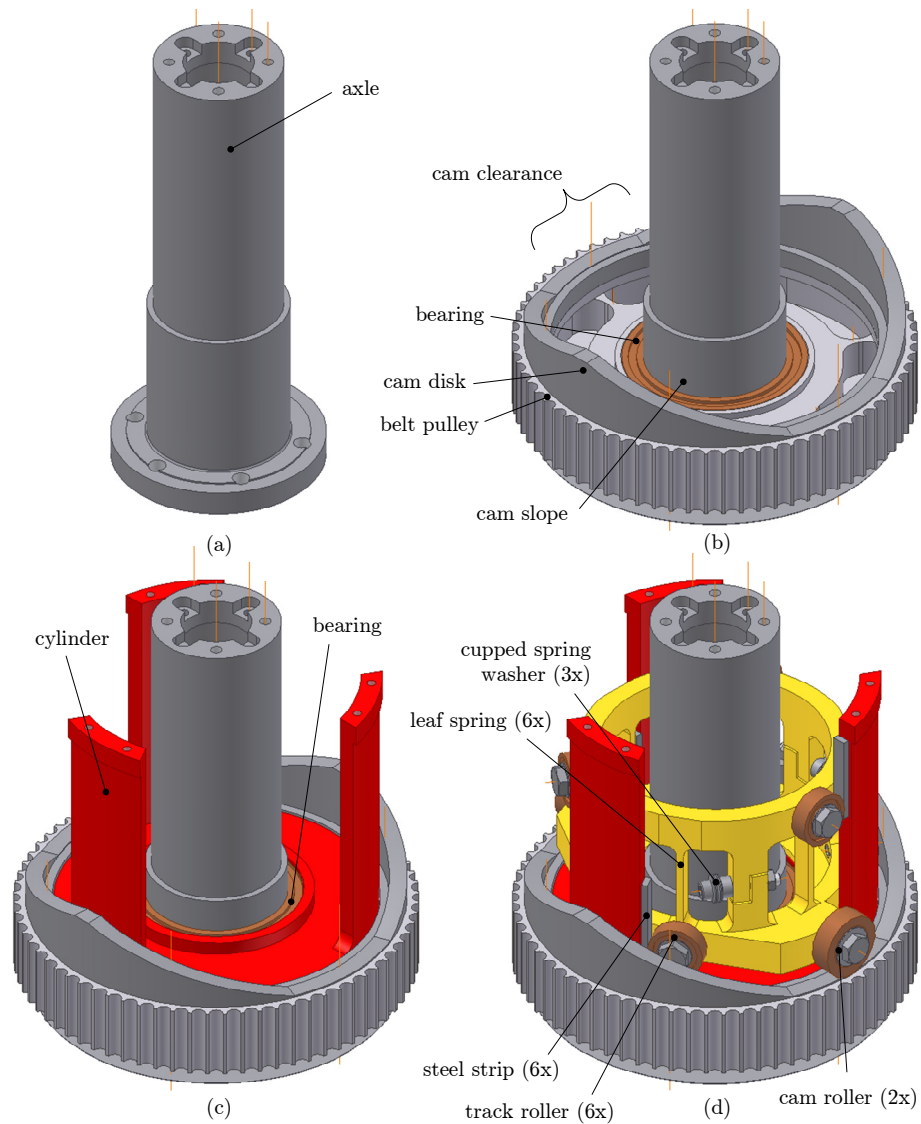


Figure 8.10: (a) The axle functions as the fixed world. It is a cylinder where the drive-aid motor is mounted into. (b) The belt pulley and cam disk are fixed to the axle via an angular contact bearing and a deep groove ball bearing such that it can only rotate around the axle. (c) The cylinder is also fixed to the axle via a deep groove ball bearing. (d) A linear guidance which is statically determined and backlash free is designed which defines the trajectory of the cam rollers when engaging the cam slope while passing on large reaction forces.

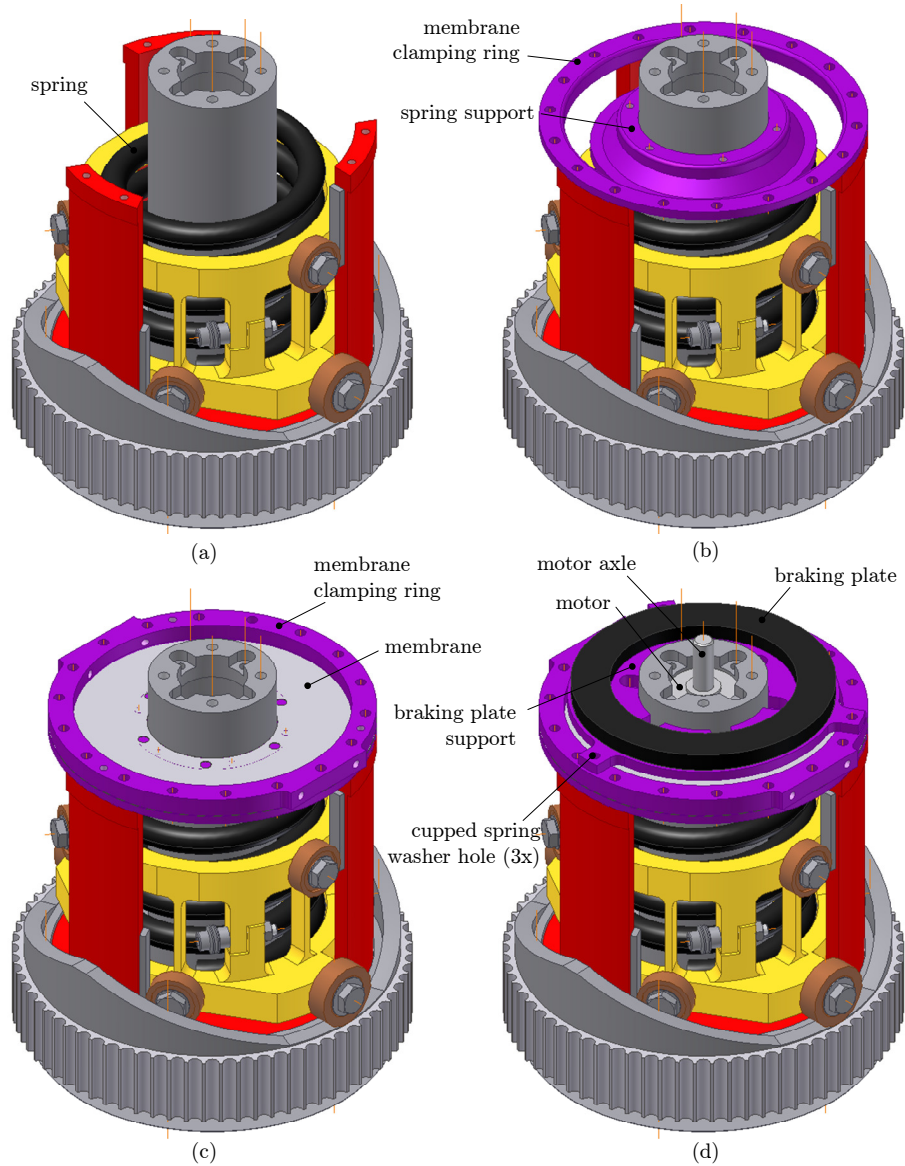


Figure 8.11: (a) A spring is put into the linear guidance. (b) A spring support is placed onto the spring. Furthermore, a membrane clamping ring is mounted onto the cylinder. (c) A membrane with another clamping ring is placed onto the first clamping ring which are bolted (not shown in figure) to the cylinder. (d) The braking plate is mounted onto the membrane via the braking plate support. The clutch gap can be adjusted with 3 cupped spring washers mounted into the cupped spring washer holes. The motor is mounted into the axle.

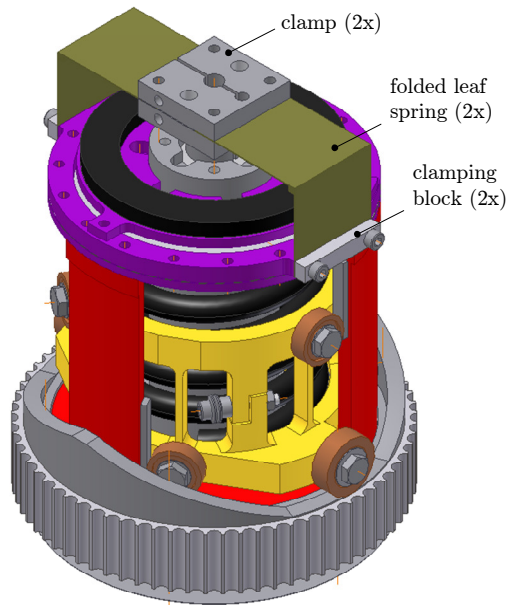


Figure 8.12: A clamp is fixed to the drive-aid motor axle. With two folded leaf springs, the motor torque is passed on to the clamping rings. The extra clamp is used to add an encoder on top.

Axle: in Figure 8.10(a), an axle is shown which is hollow where the drive-aid motor will be placed into. The axle functions as the fixed world and determines the axis of rotation for all rotating parts.

Cam-belt connection: in Figure 8.10(b), a belt pulley is added which is fixed to the axle via an angular contact bearing and a deep groove ball bearing. A gear belt, where the carriage is attached to, is connected to the drive-aid via the belt pulley. Onto the belt pulley, the cam disk is mounted. The cam disk contains a cam clearance for two cam rollers with cam slopes at each side of the cam clearance. The length of the cam clearance is determined by trading off the required power of the drive-aid motor and the compactness of the drive-aid.

Outer part linear guidance: in Figure 8.10(c), a part of the linear guidance is shown. The linear guidance can rotate around the axle using a deep groove ball bearing. The linear guidance is used both to guide the cam rollers such that they stay onto the cam disk and to counteract the reaction force of the reversing carriage.

Inner part linear guidance: in Figure 8.10(d), the moving part of the linear guidance is shown. The linear guidance is statically determined and backlash free. It uses 6 track rollers which are pretensioned using cupped spring

washers. Because the track rollers have to pass on large forces, hardened steel strips are placed at the cylinder.

Spring: in Figure 8.11(a), a spring is put inside the linear guidance which temporarily stores the kinetic energy of the carriage. Furthermore, the reaction force of the spring is used to engage the clutch and provide enough force to make the clutch self-breaking. Using Equation 8.6, the stiffness required for a certain reversal time can be computed.

Membrane support: in Figure 8.11(b), a clamping ring and a spring support is shown where a membrane will be mounted onto.

Membrane: in Figure 8.11(c), the membrane with another clamping ring is shown. The top side of the spring only has to move over a distance of the clutch gap which is a few tens of a mm. The short stroke guidance is provided by a membrane.

braking plate: in Figure 8.11(d), the braking plate is put onto the membrane via the braking plate support. Cupped spring washers are used to determine the initial clutch gap. In the figure the clutch is designed flat, however in the realized prototype the clutch has been made conical to increase the normal force.

Motor connection: in Figure 8.12, the connection of the motor axle to the linear guidance is shown. The motor axle is fixed by using a clamp. The additional clamp can be used to attach an additional encoder. The folded leaf springs provide stiffness around the vertical axis, hence the torque of the drive-aid motor is passed on via a stiff connection to the linear guidance.

In Figure 8.13, the total experimental setup is shown including drive-aid, belt, carriage and carriage-drive. For testing purposes, the carriage is modeled as a rotating mass with equivalent inertia. This way, the experimental setup is more compact and more robust for mistakes during experiments.

In the next chapter, the implementation and experimental results of the reversal mechanism prototype as described in this chapter is presented.

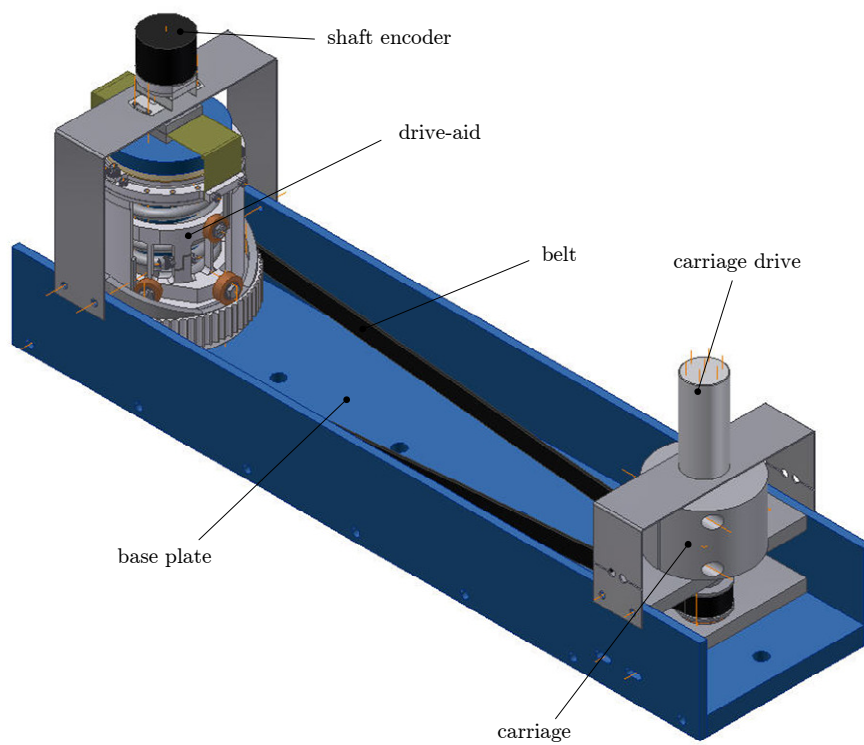


Figure 8.13: The drive-aid mounted onto the total experimental setup. On the right side, another pulley is placed with a motor and a block with an equivalent inertia as a translating mass of 5 kg representing the carriage.

Chapter 9

Reversal Mechanism Implementation

In this chapter, the implementation of the drive-aid is presented including the controller design, the system identification, the motion controller synthesis and the experimental results.

9.1 Experimental Setup

In Figure 9.1, an overview of the experimental setup is shown. The experimental setup consists of a laptop, a TUEDACs AQI data acquisition device [87], two amplifiers and the reversal mechanism containing the drive-aid and the carriage. The laptop's operating system is RTAI-Linux [61] where Matlab/Simulink/RTW [90] is used to build real-time code which runs on the laptop.

In Figure 9.2, a picture is shown of the reversal mechanism. The reversal mechanism consists of a carriage and carriage motor which are designed rotationally where the carriage has an equivalent translating mass of 5 kg felt by the belt. The belt connects the carriage with the drive-aid. The drive-aid contains the spring which buffers the kinetic energy while reversing the carriage.

Two small redesigns have been made to improve the setup. First of all, the achieved friction coefficient of the clutch was much less than expected. Two possible causes are:

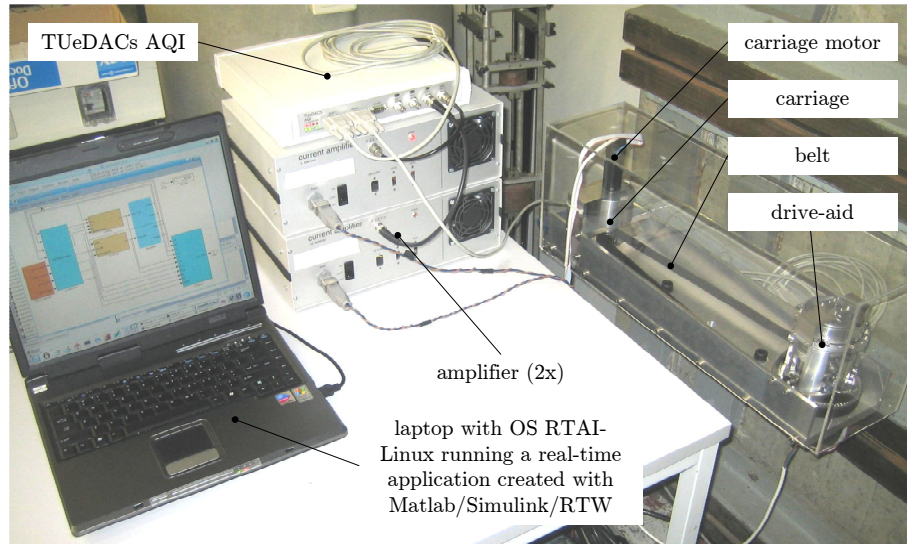


Figure 9.1: The total experimental setup

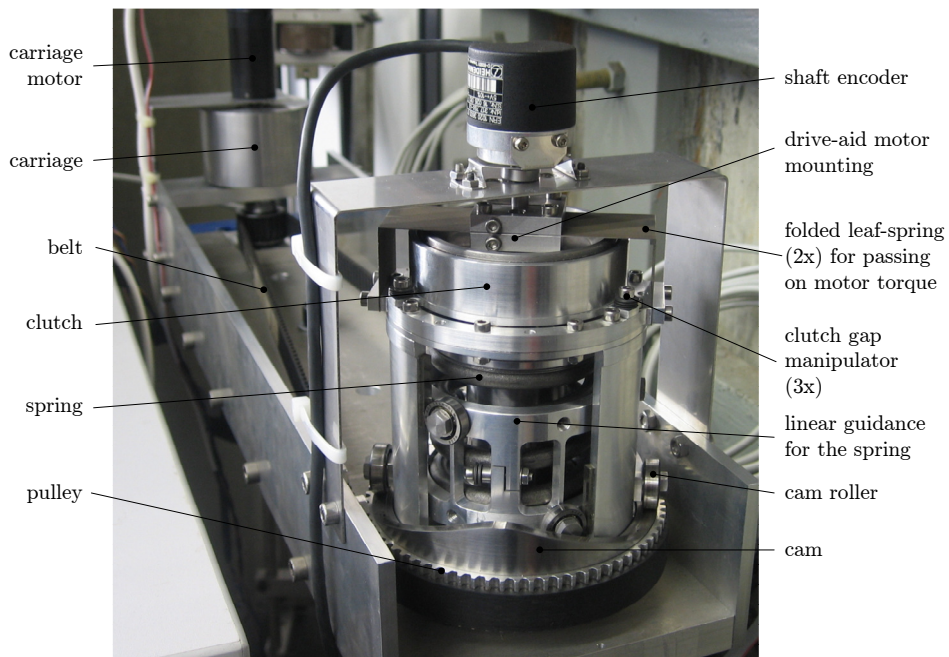


Figure 9.2: A picture of the realized prototype including the additional test setup.

- (i) the specified friction coefficient is achieved after wear in,
- (ii) a thin air film which could not manage to flow away during engaging the clutch decreases the friction coefficient.

To overcome these problems the clutch is designed conical and is equipped with a rubber layer resulting in a self-breaking clutch. Another redesign is done in the mounting of the carriage drive motor. One degree of freedom was not fixed resulting in vibrations of the rotating carriage block. This problem was easily solved by adjusting the folded leaf spring which positions the carriage motor axle.

9.2 Hybrid Controller Design

The angular position of both the carriage and drive-aid are converted to a translation of the belt for comparison. We will use the terms "carriage position" and "drive-aid position" to denote the angular position multiplied by the lever towards the translational position of the belt for the carriage and drive-aid respectively.

In the experimental setup, two motors have to be controlled, the carriage motor and the drive-aid motor. The carriage should be able to reverse at arbitrary times when moving at a constant speed. The supervisory control of both motors consists of 5 modes as shown in Figure 9.3.

A description of each mode is shown below:

mode 0: when initializing an experiment, the initial position of the cam roller with respect to the cam clearance is unknown. The middle of the cam clearance is determined by keeping the drive-aid still by using closed loop position control and supplying a constant torque to the carriage motor for a few seconds in both directions. This way, the cam roller positions itself at both sides of the cam clearance. The position of the carriage at both sides is the position corresponding to the center position for the cam roller. The difference between both positions is defined as the clearance c . The drive-aid and carriage are now aligned correctly for the experiment.

mode 1: the carriage speed \dot{x}_c is brought to printing speed v_c using a 2nd order set-point trajectory and is kept on v_c until the reverse command is given. A velocity controller is suited for this. During the constant speed trajectory of the carriage, the drive-aid should follow the carriage keeping the cam rollers in the middle of the cam clearance. This is typically a synchronization task where the position of the drive-aid x_d is synchronized with the position of the carriage x_c by using position control with the carriage position as reference.

mode 2: the reverse command is given by changing the sign of v_{des} such that:

$$\text{guard}_{1 \rightarrow 2} : v_{des} \dot{x}_c < 0 \quad (9.1)$$

The drive-aid should break and stand still before the cam roller reaches the end of the cam clearance. Assuming that the drive-aid decelerates with

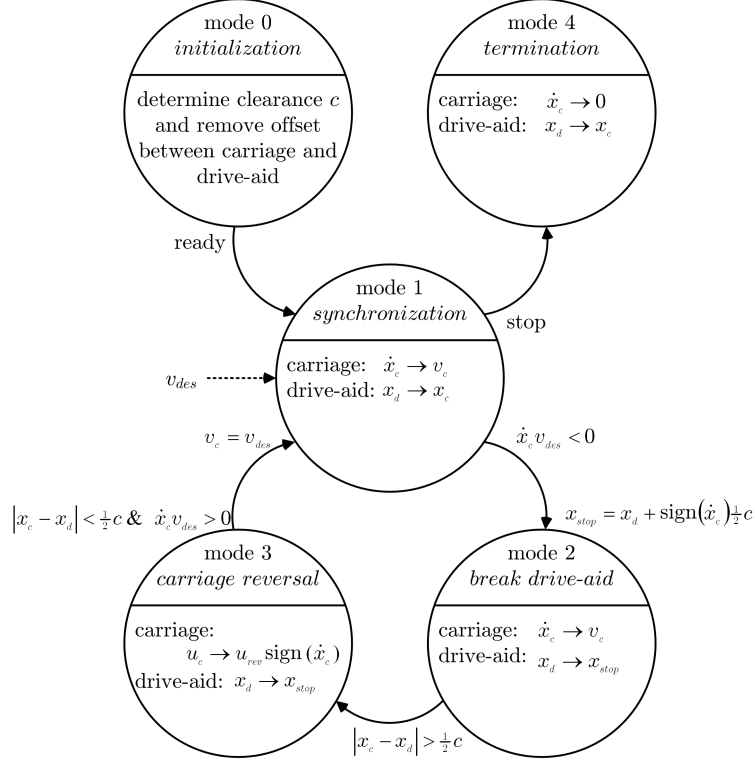


Figure 9.3: Hybrid automaton of the supervisory control of both the carriage motor and the drive-aid motor.

constant acceleration a_d from speed v_c to 0 and travels over a distance $\frac{1}{2}c$ we obtain:

$$a_d = \frac{v_c^2}{c} \quad (9.2)$$

$$t_d = \frac{c}{v_c} \quad (9.3)$$

where t_d is the breaking duration in s. For this mode, the synchronization is interfered because the trajectory is generated with respect to the drive-aid position x_d at the moment of the mode switch from mode 1 to mode 2 to obtain a smooth stand still on position:

$$x_{stop} = x_d + \text{sign}(\dot{x}_c) \frac{1}{2}c \quad (9.4)$$

Because the cam roller is still within the cam clearance the drive-aid does not disturb the carriage position which remains in velocity control with desired speed v_c .

mode 3: a mode switch from mode 2 to mode 3 occurs when the difference between the carriage and drive-aid position is larger than half the cam clearance:

$$\text{guard}_{2 \rightarrow 3} : |x_c - x_d| > \frac{1}{2}c \quad (9.5)$$

Hence, the cam roller is on the cam slope. The drive-aid controller remains a position controller with reference x_{stop} . It only needs to deliver power for a short time until the clutch has been engaged and the self-breaking property of the clutch has been engaged. The carriage is now decelerating while the kinetic energy of the carriage is being stored in the spring. For this mode, the carriage controller is disabled where only a constant voltage is applied in the direction of the carriage velocity. This way, the small energy dissipation during carriage reversal is compensated such that the carriage speed after reversal is equal to v_c . If the position difference of the carriage and drive-aid is again smaller than half the cam clearance, i.e. the clutch has been disengaged and the carriage velocity has been reversed, then a switch occurs towards mode 1:

$$\text{guard}_{3 \rightarrow 1} : |x_c - x_d| < \frac{1}{2}c \quad \& \quad \dot{x}_c v_{des} > 0 \quad (9.6)$$

In mode 1, the drive-aid is synchronized again with the carriage, using a second order trajectory towards the carriage position. An extra guard $\dot{x}_c v_{des} > 0$ has been included for the mode switch from mode 3 to mode 1 to be robust for skipping mode 3 due to sensor noise on the position signal.

mode 4: when a stop command is given, the carriage is slowed down to zero speed using a second order trajectory, where the drive-aid keeps the position control with the carriage position as reference.

This hybrid automaton has been implemented in a Matlab/Simulink S-function and is included in a Matlab/Simulink/RTW application which also contains code for communication with the TUE DACs AQI data acquisition device. The Matlab/Simulink/RTW application is then built with RTW into a real-time application with a fixed sampling time of 4096 Hz which is executed on the laptop.

9.3 System Identification

9.3.1 System Dynamics

For the frequency response measurements we use the model as shown in Figure 9.4 where y_c and y_d are the position of the carriage and drive-aid respectively. The positions are measured using encoders attached to the motor and converted to a

position at the belt. The carriage motor current amplifier and drive-aid motor current amplifier inputs are u_c in V and u_d in V respectively. They are proportional with the generated torques by the motors.

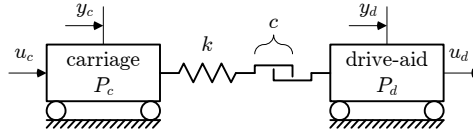


Figure 9.4: Model of the drive-aid and carriage system.

Carriage Frequency Response Function

The control of the carriage is done using velocity control. The encoder signal of the carriage motor is filtered with a differentiator including a 2nd order low pass filter with a cut-off frequency of 200 Hz, see Figure 9.5. The filtered output is considered as speed measurement y'_c .

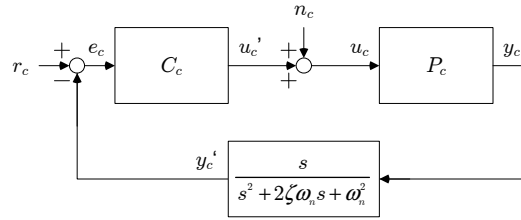


Figure 9.5: Carriage control scheme.

By injecting noise at n_c , and measuring the plant input u_c and the carriage speed y'_c we can compute the frequency response function (FRF) of the carriage system:

$$P_c(j\omega) = \frac{T_{n_c \rightarrow y'_c}}{T_{n_c \rightarrow u_c}} = \frac{S_{pc}(j\omega)}{S_c(j\omega)} \quad (9.7)$$

where $S_{pc} = \frac{P_c}{1+P_c C_c}$ is the process-sensitivity, $S_c = \frac{1}{1+P_c C_c}$ the sensitivity, and $T_{x \rightarrow y}$ denotes the transfer function from x to y .

For the reference r_c a constant speed of 0.5 m/s is chosen. The FRF is shown in Figure 9.6. The drive-aid is synchronized with the carriage such that the cam roller stays within the cam clearance, hence, the carriage and drive-aid are disconnected.

The anti-resonance and resonance are located far from each other with a resonance at a high frequency. This is caused by the heavy carriage with respect to the carriage motor. Furthermore, the carriage motor does not contain a gear to properly

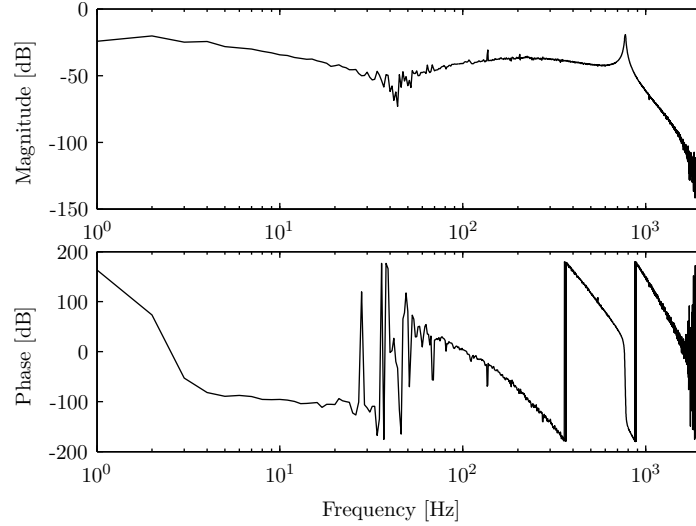


Figure 9.6: FRF of the carriage system from u_c to y'_c in m/v.s.

match the inertia of the carriage and carriage motor. Nevertheless, the carriage motor only needs to provide little power because it should only compensate for frictional losses.

Drive-aid Frequency Response Function

The drive-aid system $P_d(j\omega)$ is identified closed loop by injecting noise n_d at the plant input u_d and measuring the plant output y_d as shown in Figure 9.7.

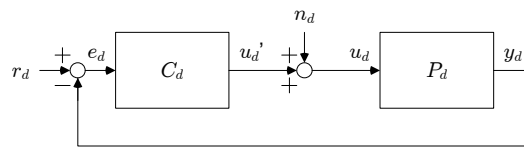


Figure 9.7: Drive-aid control scheme.

The control of the drive-aid is position based. By using a constant speed trajectory, noise is injected at n_d where u_d and y_d are measured to compute the FRF of the drive-aid system $P_d(j\omega)$ which is computed by dividing the process sensitivity $S_{p,d}(j\omega)$ by the sensitivity $S_d(j\omega)$.

In Figure 9.8, the FRF of the drive-aid system is shown. The FRF is determined with uniform distributed noise with maximum amplitudes 0.2 V, 0.4 V, and 0.6 V. The FRF differences are caused by nonlinear dynamics. At low frequencies the coherence is close to zero probably caused by coulomb friction in the bear-

ings resulting in a bad FRF measurement for low frequencies. However, for the controller design this is no problem because it is below the bandwidth which will lie somewhere between 10^1 Hz and 10^2 Hz. The difference at 40 Hz appeared to be caused by backlash in the gearbox. This lies around the bandwidth hence it jeopardizes the controller synthesis.

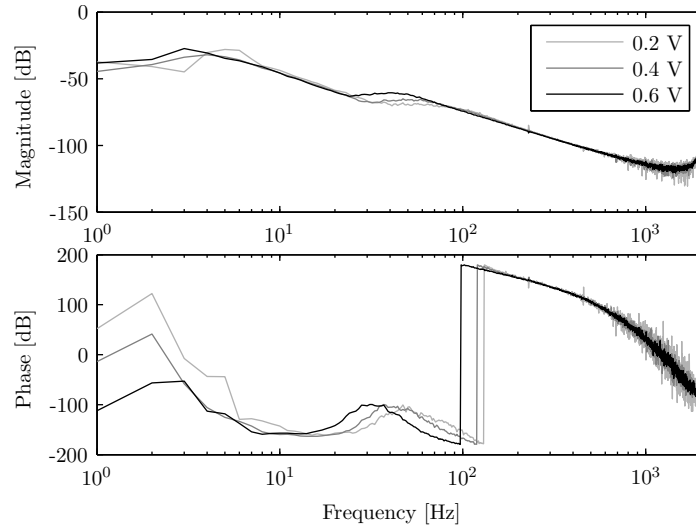


Figure 9.8: FRF of the drive-aid system. The FRF is measured with an input level noise of 0.2 V, 0.4 V, and 0.6 V in m/v.

9.3.2 Drive-aid Frequency Response Function at the Cam Slope

The system dynamics of the drive-aid change when the cam roller moves up the cam slope resulting in engagement of the clutch and an additional stiffness due to the spring. These dynamics are investigated by varying the open loop voltage applied to the carriage motor used to detect the cam slope positions. After initialization, the position of the drive-aid is controlled to the carriage position with an offset of $\frac{1}{2}c$ to perform the FRF measurement as shown in Figure 9.9. With the cam roller at the start of the cam slope, the clutch is not yet engaged.

At this position, the cam roller will just touch the cam slope as shown in Figure 9.9(b) which requires a voltage to keep it at that position. An additional speed is superimposed on the trajectory of the carriage. For several pretension levels, the FRF of the drive-aid is shown in Figure 9.10. All FRF's are measured with a maximum noise level amplitude of 0.6 V where the FRF with the pretension level of 0 V is the same as the FRF shown in Figure 9.8 with a noise level of 0.6 V.

As shown in Figure 9.10, the resonance shifts to a higher frequency. For a pretension level of 0.0 V, the stiffness and backlash of the gearbox and the drive-aid

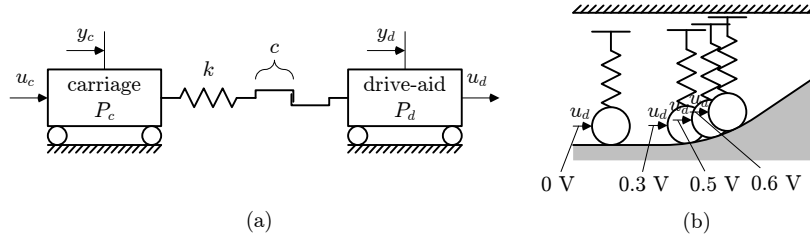


Figure 9.9: (a) The drive-aid is controlled at a position just at the slope while the speed of the carriage is controlled to 0.5 m/s, (b) the position of the drive-aid at the cam slope is varied with 0.3 V, 0.5 V, and 0.6 V average drive-aid controller effort. The clutch is not yet engaged such that the drive-aid can move freely.

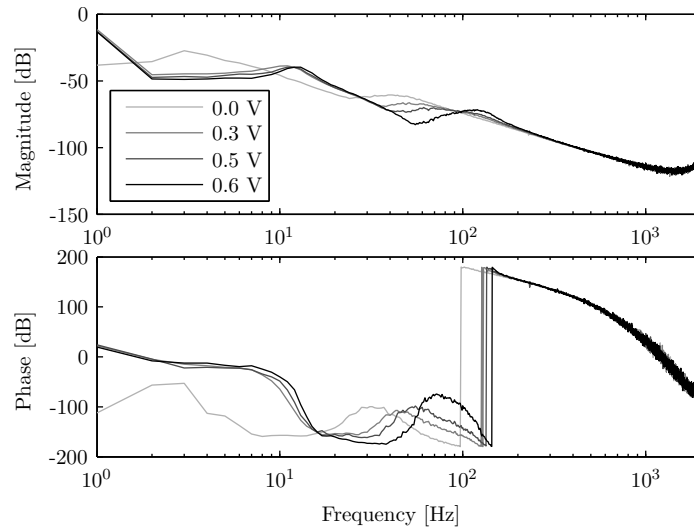


Figure 9.10: FRF of the drive-aid for the initialization voltage levels 0.0 V, 0.3 V, 0.5 V, and 0.6 V in m/v.

inertia determine the location of the resonance. When the cam roller approaches the cam slope, the backlash of the gearbox is forced to one side due to the additional spring, resulting in an increase of the resonance frequency. Furthermore, because the carriage and drive-aid are no longer uncoupled, a resonance shows up at 13 Hz. This resonance is determined by the carriage mass (0.0162 kgm^2), belt stiffness (325 Nm/rad) and gear stiffness (233 Nm/rad) placed in serial order:

$$\frac{1}{2\pi} \sqrt{\frac{1}{\frac{1}{325} + \frac{1}{233}}} = 14.6 \text{ Hz.}$$

9.3.3 Hysteresis in the Drive-aid Motor Gearbox

During carriage reversal, a small amount of energy is dissipated by the drive-aid. A contributor to this is the hysteresis in the gearbox. While fixing the drive-aid, a varying torque is applied to the drive-aid motor and the position of the motor shaft is measured. The result is shown in Figure 9.11. A hysteresis loop and a backlash of 0.1 rad is observed.

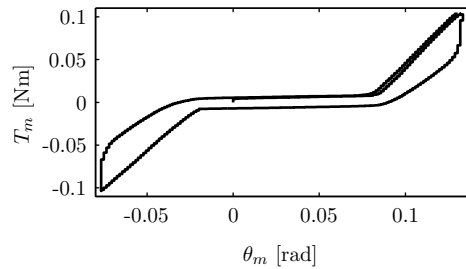


Figure 9.11: Hysteresis loop due to the gearbox of the drive-aid

Another contribution is the dissipation due to clutch engagement artifacts. The dissipated energy by the hysteresis can easily be compensated by the carriage motor. Backlash is a nonlinear effect causing variation of the resonance location around 40 Hz in Figure 9.8. The controller to be designed should be robust for such variations.

9.4 Controller Synthesis

The drive-aid remains in closed loop position control during an experiment, only the trajectory is generated online via the hybrid automaton. The plant dynamics of the drive-aid change as shown in Figure 9.8 for the cam clearance and in Figure 9.10 for the cam slope. The drive-aid is not controllable during carriage reversal due to the engagement of the clutch, hence, the controller will only be designed for the FRFs shown in Figure 9.8 and Figure 9.10. A robustly stable controller is designed complying with a maximum sensitivity magnitude of 6 dB and a bandwidth of 20 Hz for all 6 FRFs. This design problem is dealt with using ShapeIt, an optimization aided loop shaping application as described in Appendix C. The open loop FRFs for all 6 plants are shown in Figure 9.12. The bandwidth is chosen at a lower frequency than the anti-resonance/resonance because of the large uncertainty in that area around 40 Hz. Furthermore, a bandwidth above 100 Hz is not possible due to the limited actuator power and due to the time delay in the closed loop control system.

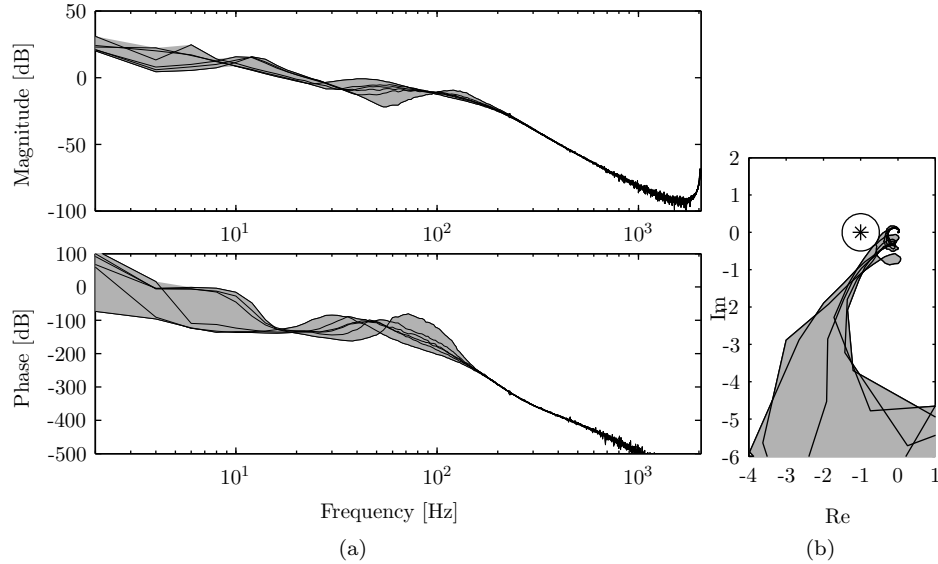


Figure 9.12: (a) The bode plot of 6 open loop frequency response functions $C_d(j\omega)P_d^i(j\omega)$, $i = 1\dots 6$. (b) Nyquist plot with point * $(-1,0)$ and circle: modulus margin equal to 6 dB.

9.5 Experimental Results

9.5.1 Initialization without the Hybrid Automaton

Because the carriage motor has a relatively low power, the system is speeded up over several cycles by directing a constant torque in the movement direction of the carriage while controlling the drive-aid position with a setpoint equal to zero. In Figure 9.13, this process is shown.

After about 6 s, the equilibrium has been reached. (In WFPS, a locking mechanism can be added to keep the energy in the spring as long as necessary, e.g. during carriage maintenance.) Clearly visible is the cam clearance between the grey lines. If these bounds are crossed, the clutch is engaged and the spring is loaded. In Figure 9.13(b), a ripple is visible which is correlated with the cam position. Probably, this is caused by the fine tuning of the position of the clutch. The clutch surface just touches the counter surface a little bit at that location resulting in a small ripple in the carriage speed. The steady state response is shown in Figure 9.14.

In this experiment, the carriage reaches a speed of 1.6 m/s with a reversal time of 0.09 s. If the constant torque for the carriage motor is increased, an equilibrium is obtained at a higher speed without an increase of the reversal time. The reversal time does not change because it only depends on the mass of the carriage and the

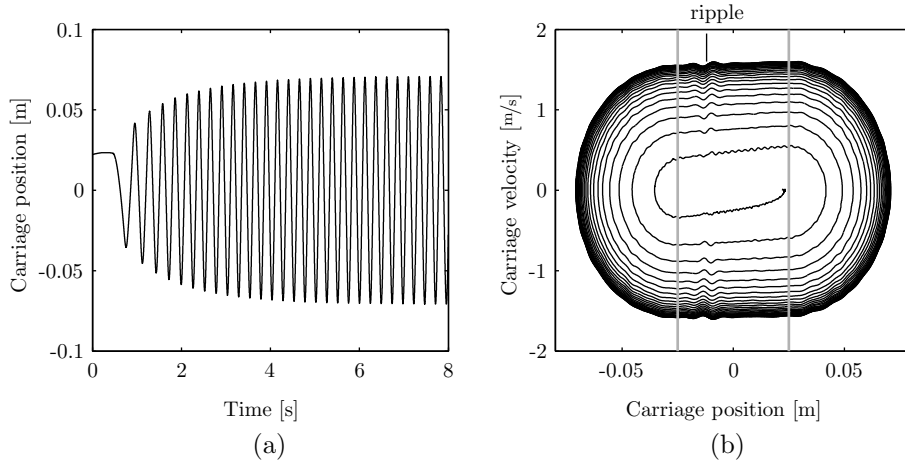


Figure 9.13: Speedup of the system by directing the torque of the carriage motor in carriage movement direction. (a): carriage position, (b): phase plot of the carriage speed versus the carriage position. The grey lines indicate the cam clearance.

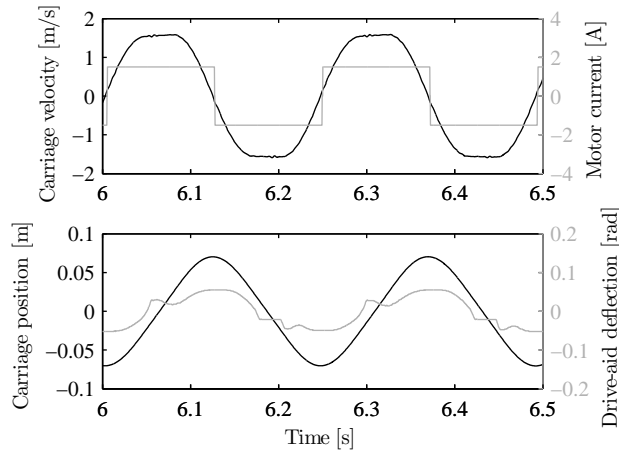


Figure 9.14: Steady state response of the speedup experiment. (a): the carriage speed and the carriage motor current, (b): the carriage position and the drive-aid deflection at the motor axle.

stiffness of the spring according to (8.4) and (8.5).

The drive-aid tracking error can be reduced with a more advanced feedforward design because it has a repetitive behavior resulting in less movement of the drive-aid and thus also less wear. Furthermore, the clutch gap has to be fine tuned such that it has no contact when the clutch is not engaged.

9.5.2 Carriage Speed Variation Including the Hybrid Automaton

In Figure 9.15, the results of three experiments are shown where the carriage speed v_c is chosen to be 0.5 m/s, 1.0 m/s, and 1.5 m/s respectively. In all experiments, the carriage moves over a distance of about 0.21 m (A4 width) with a constant speed and reverses on the sides.

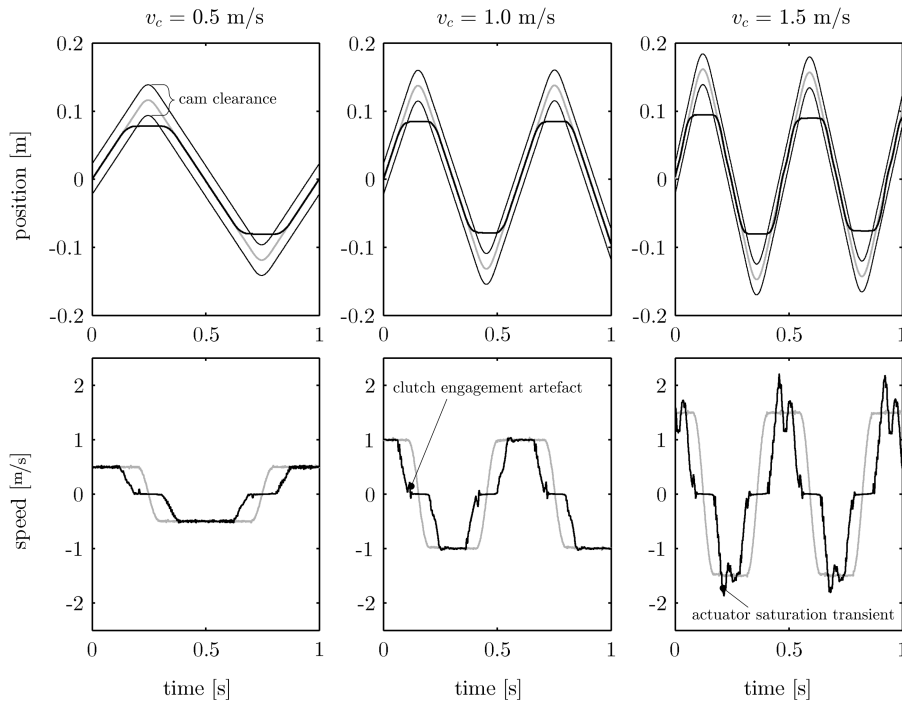


Figure 9.15: Three experiments with varying carriage speed v_c : 0.5 m/s, 1.0 m/s, and 1.5 m/s respectively. Black line: drive-aid, grey line: carriage.

The trajectories are very similar to the expected trajectories as shown in Figure 8.9. When the carriage is about to reverse, the drive-aid first slows down with a constant deceleration while the carriage keeps on moving at a constant speed. When the cam roller reaches the slope, a small clutch engagement artefact is observed at the drive-aid for varying carriage speeds, because the cam roller moves up the cam slope a little and generates a counter torque before the clutch is engaged. A feedback controller and a mass feedforward are implemented which do not take this torque peak into account. A more advanced feedforward is required to counteract this clutch engagement artefact.

As expected by (8.5), the reversal time remains the same for varying carriage speeds. Only the carriage mass and the spring stiffness determine the reversal time. For the experiment with a carriage speed of 1.5 m/s, the drive-aid shows some transient behavior after that the carriage is reversed. This is caused by the

rather conservative actuator saturation applied to the input of the drive-aid motor. This saturation could possibly be released after a thermal analysis. Nevertheless, the oscillations do not harm the performance, because the cam roller stays within the cam clearance, hence the drive-aid and carriage are uncoupled. This is also clearly visible in Figure 9.15 where the carriage speed is constant after reversal while the drive-aid shows some transient behavior due to the actuator saturation.

9.5.3 Varying Carriage Reversal Times

In Figure 9.16, an experiment is shown where the carriage moves with a speed of 1.0 m/s and reverses at varying moments. A pattern is chosen which represents a print containing areas that do not have to be printed. First it moves over distances of A0 width, then it moves over distances of A4 width at one side and afterwards on the other side. Finally, it moves over half a distance of the A0 width.

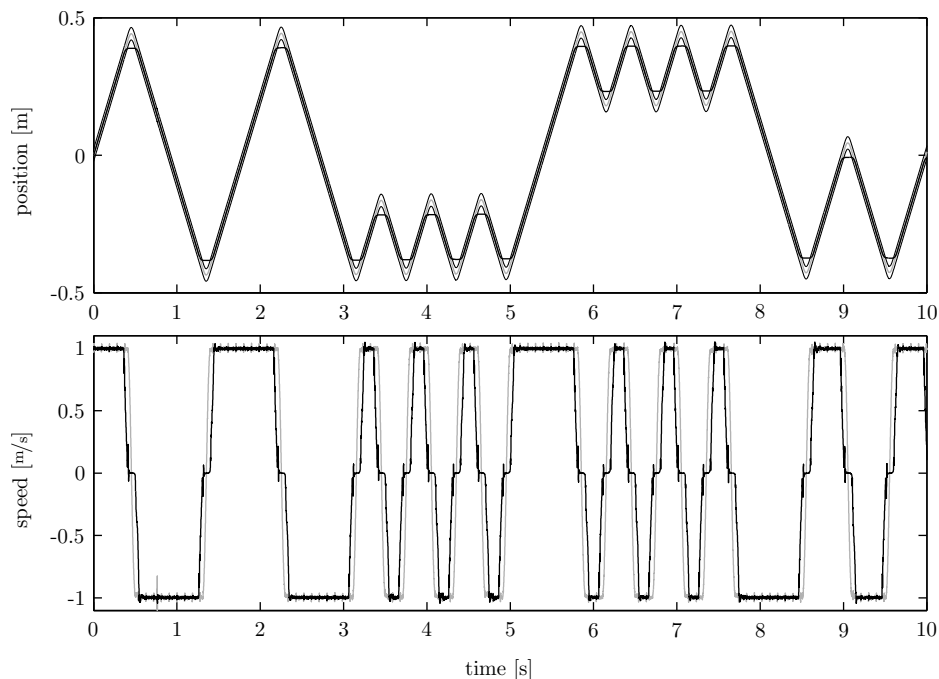


Figure 9.16: An experiment where the carriage reverses at varying times over a distance of 0.84 m (A0 width).

9.6 Discussion

9.6.1 Comparison with Scaling a Conventional Drive

From Equation 8.14 follows that a mechanical RMS power of 136 W is provided by the drive-aid ($v_c = 1.6$ m/s, $x_c = 0.05$ m, $t_{\%} = 74\%$) for the experiment as shown in Figure 9.13. When the drive-aid is in use, the mechanical RMS power that the carriage motor delivers can be approximated as follows: (assuming that the steady state speed is constant when not reversing)

$$\begin{aligned} P_{carriage}(t) &= T(t)w(t) = KI(t)\frac{\dot{x}(t)}{r} \\ &= KI_{ampl}\frac{|\dot{x}(t)|}{r} \end{aligned} \quad (9.8)$$

$$\begin{aligned} P_{carriage}^{RMS} &= \sqrt{\frac{1}{t_{cycle}} \int_0^{t_r} P_{carriage}^2(t) dt} \\ &= \frac{KI_{ampl}v_c}{r} \sqrt{2 - t_{\%}} \end{aligned} \quad (9.9)$$

which is 4.5 W for the parameters: motor constant $K = 25 \cdot 10^{-3}$ Nm/A, current amplitude $I_{ampl} = 1.5$ A, carriage speed $v_c = 1.6$ m/s, small pulley radius $r = 0.015$ m and relative reversal time $t_{\%} = 74\%$. Compared to the mechanical power required to reverse the carriage, this is about 30 times less.

For a minimum print width $x_c = 0.21$ m and a reversal time of 0.09 s ($t_{\%} = 46\%$), the drive-aid provides an RMS power of 168 W. Furthermore, the required current for the carriage drive linearly depends on the speed v_c resulting in $P_{carriage}^{RMS} = 5.6$ W. This is about 30 times less power consumption when using the drive-aid. When comparing the size of the drive-aid to a conventional carriage drive providing the same power, e.g. the Kollmorgen/Danaher AKM Brushless PM Servo Motor AKM33E, it will be about equal considering the volume as shown in Figure 9.17.

9.6.2 Cost Indication

In Figure 9.18, a cost indication is given of a Maxon EC-motor as a function of the motor's power showing a linear trend. A 500 W motor would cost about €300,- more than a motor of existing designs where most drives have a power output less than 100 W. This is an indication for the maximum budget for the drive-aid.

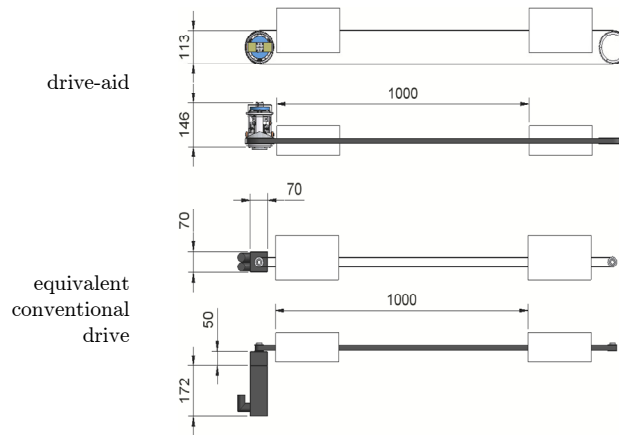


Figure 9.17: Comparison of the drive-aid with an equivalent conventional drive.

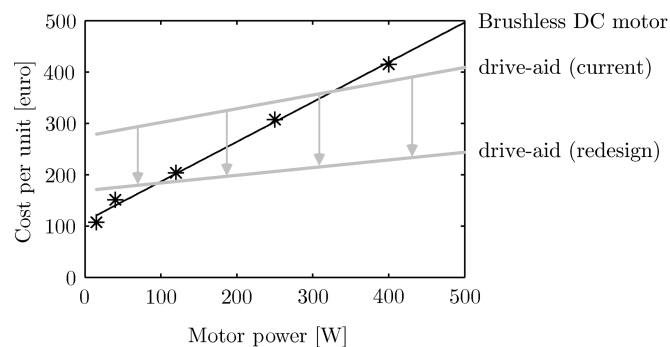


Figure 9.18: Price of a Maxon EC-motor including DEC amplifier (March 2007) as a function of the power assuming a purchase of 750 units compared to a cost estimate of the drive-aid.

Furthermore, the estimated cost per unit for the current drive-aid and its redesign is given. The slope is less steep due to the easy scalability of the drive-aid.

The drive-aid is the first prototype to assess the feasibility of buffering the kinetic energy of the carriage for reversal. To make this approach profitable compared to scaling a conventional drive, complexity has to be decreased. The most complex part in the current prototype is the linear guidance which should pass through a large torque over a large distance. Furthermore, size and weight can be reduced by further engineering the design, e.g. by optimizing the geometry and using lighter materials.

We already have ideas for a second prototype which does not require such a long stroke guidance resulting in a less complex, smaller-sized and lightweight design. This will make the design more compact and cheaper such that it is more profitable

compared to scaling a conventional carriage drive. Some illustrations are shown in Appendix D. The size decreases by about a factor of 2 as shown in Figure D.2.

9.6.3 Conclusions

A prototype has been built and experiments have been conducted showing promising results. The first experiments show that the power of the drive motor can be reduced at least by a factor of 30 while keeping the reversal time equal. This power reduction compensates the extra cost needed for the drive-aid. Because this drive-aid can be easily scaled for higher productive WFPS, it has the potential to become an attractive alternative in the future.

Experiments show that the concept is feasible. The reversal time is 0.09 s with a mass of 5 kg and a carriage speed of 1.6 m/s. A conventional carriage drive should provide an RMS power of 136 W to fulfill the same specifications. With the drive-aid, only an RMS power of 4.5 W is used by the carriage motor which is mainly used to compensate for energy loss due to friction. Although an energy gain of a factor of 30 is already achieved, with increasing performance requirements, this gain will even increase because of the easy scalability of the proposed drive-aid.

Part IV

Closing

Chapter 10

Conclusions and Recommendations

In this chapter, conclusions will be drawn and recommendations will be given for all parts in this thesis. This thesis focused on the performance improvement of higher productive WFPS. It started with an investigation of the design space to come up with innovative solutions for improving WFPS in Part I. Two concepts, (i) active printhead alignment and (ii) energy buffered carriage reversal have been worked out in Part II and Part III respectively.

10.1 Conclusions

This thesis focused on the performance improvement of higher productive WFPS by following the design methodology as presented in Section 1.4. Two concepts were developed by combining existing methods in the mechatronic design space to obtain innovative solutions. The design methodology is set up generically such that it can be applied to a wider range of applications where a trade off has to be made between productivity and accuracy.

10.1.1 Part I

In Chapter 1, the motivation of this thesis was presented. Inkjet technology is an established field of research, with a history going back to 1879. Today, it is still an active field of research where product innovations are created and new

applications are found. This thesis focused on improving performance of inkjet technology for WFPS. More specifically, the positioning in time and space in all 6 DOFs of the printheads was focused at. For higher productive WFPS design boundaries are crossed when scaling existing designs. The goal was to come up with mechatronic solutions to meet the desired performance specifications by following the design methodology as presented in Section 1.4. There is an analogy with the optimization of complex, non-convex problems, where the most important idea is that making a large step in the design space is necessary to come up with a concept which increases the performance by a large step.

In Chapter 2, a systematic method was proposed to investigate the influence of parameter variations, e.g. manufacturing tolerances, on the printing accuracy. The main contributors to printing inaccuracy are:

- (i) the carriage rotation in z caused by the carriage guidance straightness
- (ii) the mounting accuracy of all printheads in y -direction and φ_x rotation.

Most of the other parameter variations can be removed via calibration based on correcting the jet timing. Furthermore, the model derived with the systematic method can be used for error budgeting. The model is inverted where degrees of freedom are derived to redistribute the variations over the parameters without changing the printing accuracy.

In Chapter 3, both a productivity and a cost model for WFPS is proposed. Important findings are:

- (i) a higher jet frequency can result in a lower productivity,
- (ii) the carriage size $x_c y_c$ should be minimized for productivity however, increasing the carriage height y_c is less problematic than increasing the carriage width x_c ,
- (iii) using asymmetric rasters (increasing r_x/r_y) results in a higher printing efficiency for higher productive WFPS,
- (iv) multi-pass in x -direction decreases the productivity dramatically.

In Chapter 4, the design methodology as presented in Section 1.4 was projected onto the content of this thesis. The bottlenecks that show up for higher productive WFPS were explored in Chapter 2 and Chapter 3. In Chapter 4, a number of concepts were presented that overcome the bottlenecks which are found for higher productive WFPS. Two of them have been chosen and were worked out further in Part II and Part III.

10.1.2 Part II

In Chapter 5, a cheap printhead alignment sensor has been designed and investigated. The concept has been shown to be feasible regarding the target accuracy of $1 \mu\text{m}$. For WFPS, the sensor can be used to estimate the misalignment of the printheads. This enables control of the printheads which can reduce the tolerance specifications of the guidance, carriage, and printhead mounting. The sensor

could also easily be used in other applications for 2 DOF position measurements. If two of these sensors are placed on the same rigid body, a 4 DOF measurement can be done relative to a string.

In Chapter 6, a printhead alignment mechanism has been designed and tested. The mechanism, consisting of a leaf spring guided sled with a voice coil actuator and string sensor, was designed by means of FEM simulations. In this approach, the system's dynamic behavior has been examined and optimized.

The design allows for an easy printhead replacement, combined with an exact constraint sled connection with minimal hysteresis for high reproducibility. Most components can be made by common manufacturing processes, which saves cost. From the improvements of individual printhead positioning, a better print quality of WFPS can be expected with the new printhead alignment system.

In Chapter 7, experimental results were presented of the active alignment concept. By using active control, the accuracy is improved while confining cost of production. The worst-case performance has been determined by exciting the system with disturbances which represent manufacturing tolerances and dynamics of the printhead, printhead mounting, carriage, guidance and printer frame. A maximum error of $8.1 \mu\text{m}$ has shown to be the worst-case performance, where $2 \mu\text{m}$ accuracy is the nominal performance. The worst-case performance is below the specified $10 \mu\text{m}$, hence the concept is feasible.

10.1.3 Part III

In Chapter 8, a new carriage drive design for WFPS is proposed. The new drive reverses the carriage by buffering the kinetic energy of the carriage resulting in a fast reversal and a high energy efficiency for higher productive WFPS. A spring is used as an energy buffer and a clutch is designed which engages smoothly enabling reversal at varying moments. Only a small carriage motor is required to overcome friction forces acting on the carriage. The mechanical power required for carriage reversal has been investigated in relation to design parameters like carriage speed, carriage mass, carriage width and reversal time. Thereafter, the design of the realized prototype was presented.

In Chapter 9, a prototype has been built and experiments have been conducted showing promising results. Experiments show that the concept is feasible. The reversal time is 0.09 s with a mass of 5 kg and a carriage speed of 1.6 m/s . A conventional carriage motor should provide an RMS power of 136 W to fulfill the same specifications. With the drive-aid, only an RMS power of 4.5 W is used by the carriage motor which is largely used to compensate for energy loss due to friction. Although a power gain of a factor of 30 is already achieved, with increasing performance requirements, this gain will even increase because of the easy scalability of the proposed drive-aid.

To obtain more similar control with respect to a real printer, i.e. the carriage can

reverse at varying times at command, a hybrid automaton has been developed and implemented to realize this. Experiments show that the carriage is able to reverse at varying times. Furthermore, experiments show that the reversal time of the carriage is independent of the carriage speed as expected in Chapter 8.

10.2 Recommendations

10.2.1 Part I

- The productivity analysis, the sensitivity analysis, and the optimization based error budgeting can be applied to other types of printers, e.g. high volume printers or even other applications where a trade-off has to be made between accuracy and productivity, e.g. wafer-steppers.

10.2.2 Part II

- For the printhead alignment mechanism design, the bandwidth is limited to 50 Hz due to the total amount of time delay of 0.9 ms in the present setup. A faster data-acquisition/signal processing unit for the string position signal will open the way to higher bandwidth and even better performance.
- Implementation of the active alignment concept on a real printer is necessary to assess also the print quality that can be obtained with this concept instead of printing accuracy.
- The active alignment concept uses a reference fixed to the printer frame which enables the possibility to stagger printheads in paper transport direction and use several carriages without sacrificing printing accuracy. This extra design freedom can be used to improve printer performance in future designs.

10.2.3 Part III

- The first prototype was built to check the feasibility of the concept. However, it is still too complex to outperform a scaled conventional motor regarding cost of production and reliability. This was already expected during the design process. During the design process of the first prototype, feasibility was considered to be more important than cost of production. As an answer to this, a redesign is proposed in Appendix D which is less complex and half in size. A prototype would show whether this concept does outdistance a scaled conventional motor or not.
- The clutch engagement should be investigated in more detail to determine wear and lifespan of the drive-aid concept.

Bibliography

- [1] D. O. Anderson and J. B. Moore. *Optimal Control: Linear Quadratic Methods*. Prentice Hall, Englewood Cliffs, NJ, USA, 1990.
- [2] P. Barrade and A. Rufer. Current capability and power density of supercapacitors: considerations on energy efficiency. In *EPE 2003 : European Conference on Power Electronics and Applications*, 2003.
- [3] T. G. Beckwith, R. D. Marangoni, and J. H. Lienhard V. *Mechanical measurements*. Addison-Wesley, New York, 1993.
- [4] R. Beeson. Desktop inkjet - redefining the competitive landscape. *The 9th annual inkjet printing conference, IMI*, 2000.
- [5] D. J. H. Bruijnen, M. J. G. van de Molengraft, A. A. Draad, and T. Heeren. Productivity analysis of a scanning inkjet printer. In *NIP21: International Conference on Digital Printing Technologies*, pages 129–132, 2005.
- [6] D. J. H. Bruijnen, M. J. G. van de Molengraft, T. Heeren, A. A. Draad, and M. Steinbuch. Design of a printhead alignment sensor for a temperature varying environment. In *American Control Conference*, pages 388–393, Minneapolis, United states, 2006.
- [7] D. J. H. Bruijnen, M. J. G. van de Molengraft, and M. Steinbuch. Optimization aided loop shaping for motion systems. In *IEEE International Conference on Control Applications*, pages 255–260, Munich, Germany, 2006.
- [8] D. J. H. Bruijnen, M. J. G. van de Molengraft, and M. Steinbuch. Efficient iir notch filter design via multirate filtering targeted at harmonic disturbance rejection. In *4th IFAC Symposium on Mechatronic Systems*, pages 318–323, 2006.
- [9] D. J. H. Bruijnen, A. W. Notenboom, M. J. G. van de Molengraft, A. A. Draad, T. Heeren, and M. Steinbuch. Printhead alignment via active control. *Control Engineering Practice*, submitted, 2007.

-
- [10] D. J. H. Bruijnen, E. Tabak, M. J. G. van de Molengraft, and M. Steinbuch. Mechatronic design of an efficient drive for wide format printing systems. In *IEEE International Conference on Mechatronics*, Kumamoto, Japan, 2007.
- [11] D. J. H. Bruijnen, M. J. G. van de Molengraft, T. Heeren, A. A. Draad, and M. Steinbuch. Active printhead alignment for wide format printing systems. In *American Control Conference*, New York, United States, 2007.
- [12] W. L. Buehner, J. D. Hill, T. H. Williams, and J. W. Woods. Application of ink jet technology to a word processing output printer. *IBM J. Res. Develop.*, 21(1):2–9, January 1977. ISSN 0018-8646.
- [13] B. H. M. Bukkems, J. J. T. H. de Best, M. J. G. van de Molengraft, and M. Steinbuch. Robust piecewise linear sheet control in a printer paper path. In *2nd IFAC Conference on Analysis and Design of Hybrid Systems*, pages 142–147, Alghero, Sardinia, Italy, 2006.
- [14] H. Y. Jan C. L. Lin and N. C. Shieh. GA-based multiobjective PID control for a linear brushless DC motor. *IEEE/ASME Transactions on Mechatronics*, 8(1):56–65, March 2003.
- [15] R. Cardenas, R. Pena, J. Clare, and G. Asher. Power smoothing in a variable speed wind-diesel system. In *Proceedings of the Power Electronics Specialist Conference*, volume 2, pages 754–759, 2003.
- [16] S. Cole, K. Johnson, and Y. Kipman. A novel approach to print head alignment for wide format printers. *The 21st international conference on digital printing technologies*, pages 133–136, 2005.
- [17] L. S. Czarnecki and H. L. Ginn III. The effect of the design method on efficiency of resonant harmonic filters. In *Power delivery*, volume 20, pages 286–291, 2005.
- [18] E. O. Doebelin. *Measurement Systems: Applications and Design*. McGraw-Hill, 2004.
- [19] J. C. Doyle, K. Glover, P. P. Khargonekar, and B. A. Francis. State-space solutions to standard \mathcal{H}_2 and \mathcal{H}_∞ control problems. *IEEE Transactions on Automatic Control*, 34:831–847, 1989.
- [20] R. Elmqvist. Measuring instrument of the recording type, U.S. patent 2566443, 1951.
- [21] I. Endo, y. Sato, s. Saito, T. nakagiri, and S. Ohno. Liquid jet recording process and apparatus there for, great britain patent 2007162, 1979.
- [22] R. Fisher and D. Naidu. A comparison of algorithms for subpixel peak detection, 1996.
- [23] B. A. Francis and W. M. Wonham. The internal model principle for linear multivariable regulators. *Applied Mathematics and Optics*, 2:170–194, 1975.

-
- [24] G. F. Franklin, M. L. Workman, and D. Powell. *Digital Control of Dynamic Systems*. Addison-Wesley Longman Publishing Co., Inc., Boston, MA, USA, 1997.
- [25] P. D. Gast, M. S. Hickman, D. H. Donovan, X. Gros, and M. A. Gil. Inkjet printhead calibration, patent no. EP0978390, 2000.
- [26] J. F. Gieras. *Permanent magnet motor technology: design and applications, 2nd edition*. Marcel Dekker, Basel, 2nd edition, 2002.
- [27] L. C. Hale. *Principles and techniques for designing precision machines*. PhD thesis, University of California, 1999.
- [28] D. C. Hanselman and B. Littlefield. *Mastering MATLAB 6: A Comprehensive Tutorial and Reference*. Prentice Hall, 2001.
- [29] S. Hara, Y. Yamamoto, T. Omata, and M. Nakano. Repetitive control system - a new type servo system. *IEEE Transactions on Automatic Control*, 33: 659–668, 1988.
- [30] S. Hara, T. Iwasaki, and D. Shiokata. Robust pid control using generalized kyp synthesis: direct open-loop shaping in multiple frequency ranges. *IEEE Control Systems Magazine*, 26:80–91, 2006.
- [31] R. D. Haselby. Calibration system to correct printhead misalignments, patent no. US6568782, 2003.
- [32] M. R. Hatch. *Vibration simulation using Matlab and Ansys*. Chapman & Hall/CRC, 2001.
- [33] N. He, W. Jia, D. Yu, L. Huang, and M. Gong. A novel type of 3-axis lens actuator with tilt compensation for high-density optical disc system. *Sensors and Actuators A*, 115:126–132, 2004.
- [34] W. P. M. H. Heemels and G. J. Muller. *Boderc: Model-based design of high-tech systems*. Embedded Systems Institute, Eindhoven, The Netherlands, 2006.
- [35] W. P. M. H. Heemels, E. van de Waal, and G. J. Muller. A multi-disciplinary and model-based design methodology for high-tech systems. In *Proceedings of Conference on System Engineering Research*, 2006.
- [36] J. Heinzl and C. H. Hertz. Ink-jet printing. *Adv. Electronics and Electron Physics*, 65:91, 1985.
- [37] R. C. Hibbeler. *Engineering Mechanics - Mechanics of Materials*. Prentice Hall, 1997.
- [38] J. H. Holland. *Adaptation in Natural and Artificial Systems*. PhD thesis, University of Michigan, 1975.

- [39] K. Huber. On the design of cauer filters. *International Journal of Electronics and Communications*, 58:223–224, 2004.
- [40] K. Hushino, T. Nagai, Y. Mita, M. Sugiyamsa, and K. Matsumoto. Active ink-jet nozzles equipped with arrayed visual sensors for parallel alignment control. In *18th IEEE International Conference on Micro Electro Mechanical Systems*, pages 48–51, 2005.
- [41] Concepts in Digital Imaging Technology. <http://micro.magnet.fsu.edu/primer/digitalimaging/concepts/ccdanatomy.html>.
- [42] ANSYS Inc. <http://www.ansys.com>, .
- [43] Magnet Sales & Manufacturing Inc. <http://www.magnetsales.com>, .
- [44] NASA Space Instrument and Sensing Technology. Active pixel sensors. http://ranier.hq.nasa.gov/Sensors_page/MicroInst/APS/CmosAPS.html, 1994.
- [45] S. Kamisuki, M. Fujii, T. Takekoshi, C. Tezuka, and M. Atobe. A high resolution, electrostatically driven commercial inkjet printhead. In *The 13th annual international conference on Micro Electro-Mechanical Systems*, pages 793–798, 2000.
- [46] F. J. Kamphoefner. Ink-jet printing. *IEEE Trans. Elec. Devices*, 19:584, 1972.
- [47] E. Kan and J. Aggarwal. Multirate digital filtering. *Audio and Electroacoustics*, 20:223–225, 1972.
- [48] T. Kaneko, T. Ohmi, N. Ohya, N. Kawahara, and T. Hattori. A new, compact and quick-response dynamic focusing lens. In *International conference on solid-state sensors and actuators*, pages 63–66, 1997.
- [49] J. Kennedy and R. Eberhart. Particle swarm optimization. In *Proceedings of the IEEE International Conference on Neural Networks 1995*, pages 1942–1948, 1995.
- [50] N. Killingsworth and M. Krstić. Auto-tuning of pid controllers via extremum seeking. In *Proceedings of the 2005 American Control Conference*, pages 2251–2256, 2005.
- [51] K.-C. Kim, S. B. Oh, S. H. Kim, and Y. K. Kwak. Design of a signal processing algorithm for error-minimized optical triangulation displacement sensors. *Measurement Science and Technology*, 12:1683–1688, 2001.
- [52] S. Kirkpatrick, C. D. Gelatt, and M. P. Vecchi. Optimization by simulated annealing. *Science*, 220, 4598:671–680, 1983.
- [53] M. P. Koster and W. v.d. Hoek. *Design principles for accurate moving and positioning, 3rd edition*. Twente University Press, Twente, 3rd edition, 2000. (in Dutch).

- [54] L. Kuhn and A. Myers. Ink-jet printing. *Scientific American*, 240:162–178, 1979.
- [55] R. H. A. Kuypers. Active control of the printhead-paper distance in an inkjet printer. Master’s thesis, Technische Universiteit Eindhoven, 2000.
- [56] I. D. Landau, F. Rolland, C. Cyrot, and A. Voda. Digital robust control. the combined pole placement/sensitivity shaping method. *French version published in La Robustesse. Presented at the Summer Control School of Grenoble ‘Robustness Analysis and Design of Robust Controllers’*, 1993.
- [57] H. P. Le. Progress and trends in ink-jet printing technology. *Journal of Imaging Science and Technology*, 42:49–62, 1998.
- [58] S. Lemoufouet and A. Rufer. Hybrid energy storage systems based on compressed air and supercapacitors with maximum efficiency point tracking. In *Proceedings of the European Conference on Power Electronics and Applications*, pages 1–10, 2005.
- [59] W. Lloyd and H. Taub. Ink-jet printing. *Out Put Hardcopy Devices*, pages 311–370, 1988.
- [60] B. J. Lurie, B. J. Lurie, and P. J. Enright. *Classical Feedback Control with MATLAB*. Marcel Dekker, Inc., New York, NY, USA, 2000.
- [61] P. Mantegazza, E. L. Dozio, and S. Papacharalambous. RTAI: Real Time Application Interface. *Linux J.*, 2000(72es):10, 2000. ISSN 1075-3583.
- [62] The MathWorks. Genetic algorithm and direct search toolbox, 2003.
- [63] The MathWorks. <http://www.mathworks.com>.
- [64] K. L. Moore. Iterative learning control - an expository overview. *Applied and Computational Controls, Signal Processing, and Circuits 1*, 1:151–214, 1998.
- [65] G. J. Muller. *CAFCR: A multi-view method for embedded systems architecting; balancing genericity and specificity*. PhD thesis, Technische Universiteit Delft, 2004.
- [66] T. Nagai, K. Hoshino, K. Matminoto, and I. Shimoyama. Direct ink-jet printing of electric materials with active alignment control. In *The 13th International Conference on Solid-State Sensors, Actuators and Microsystems*, pages 1461–1464, 2005.
- [67] A. W. Notenboom. Mechatronic design of an active printhead alignment mechanism for inkjet printers, DCT 2006.088. Master’s thesis, Technische Universiteit Eindhoven, 2006.
- [68] A. W. Notenboom, D. J. H. Bruijnen, F. G. A. Homburg, M. J. G. van de Molengraft, L. J. M. van den Bedem, and M. Steinbuch. Mechatronic design of an active printhead alignment mechanism for wide format printing systems. *Mechatronics*, 17(2-3):109–120, 2006.

- [69] H. J. Orchard and Jr. A. N. Willson. Elliptic functions for filter design. *Fundamental theory and applications*, 44(4):273–287, 1997.
- [70] S. U. A. Qidwai and M. Bettayeb. A new robust scheme for harmonic elimination. *Electric Power Systems Research*, 43:45–51, 1997.
- [71] S. K. Ravensbergen, R. R. J. J. van Doorn, and E. J. P. van den Hoven. Report master project 4e089, hall effect position sensor, DCT 2006.070. Technical report, Technische Universiteit Eindhoven, 2006.
- [72] F. R. S. Rayleigh. On the instability of jets. *Proc. London Math. Soc.*, 10:4–13, 1879.
- [73] S. Rechka, E. Ngandui, J. Xu, and P. Sicard. Performance evaluation of harmonics detection methods applied to harmonics compensation in presence of common power quality problems. *Mathematics and Computers in Simulation*, 63:363–375, 2003.
- [74] H. G. J. Rutten and S. H. Koekebakker. Optical sensor device for detecting edge of moving sheet, includes control device for determining number of light sensitive components between two reference components, patent no. nl1016305c, 2002.
- [75] MSC Software. <http://www.mscsoftware.com>.
- [76] M. Steinbuch. Repetitive control for systems with uncertain period-time. *Automatica*, 38(12):2103–2109, 2002.
- [77] G. Strang and T. Nguyen. *Wavelets and Filter Banks*. Cambridge Press, Wellesley, 1996.
- [78] B. G. Streetman and S. K. Banerjee. *Solid State Electronic Devices*. Prentice Hall, Upper Saddle River, 6th edition, 2006.
- [79] R. G. Sweet. High frequency recording with electrostatically deflected ink-jets. *Rev. Sci. Instrum.*, 36:131, 1965.
- [80] F. F. Syed, A. H. M. A. Rahim, and J. M. Ba-Khashwain. Robust stat-com controller design using pso based automatic loop-shaping procedure. In *Proceedings of the 2005 IEEE Conference on Control Applications*, pages 440–445, 2005.
- [81] E. Tabak. Design of a reversal mechanism of the carriage in a wide format printing system, DCT 2006.132. Master’s thesis, Technische Universiteit Eindhoven, 2006.
- [82] H. K. Tang, W. H. Kuek, R. Gozali, and R. Liew. Ink jet printer pioneers and competitors. In *Management of Innovation and Technology*, pages 94–98, 2000.
- [83] K. S. Tang, K. F. Man, S. Kwong, and Q. He. Genetic algorithms and their applications. *IEEE Signal Processing Magazine*, 13:22–37, 1996.

-
- [84] L. Thede. *Analog and digital filter design using C*. Prentice-Hall, Inc., Upper Saddle River, NJ, USA, 1996.
- [85] P. Torpey and M. Sengun. A customer-oriented productivity model for thermal ink-jet printers. In *IS&T's NIP 14: International Conference on Digital Printing Technologies*, pages 44–49, 1998.
- [86] P. Tsao, M. Senesky, and S. R. Sanders. An integrated flywheel energy storage system with homopolar inductor motor/generator and high-frequency drive. *IEEE Transactions on Industry Applications*, 39:1710–1725, 2003.
- [87] TUE-DACS-Group. Tuedacs, tu/e data acquisition and control system. <http://www.tuedacs.nl>, 2000.
- [88] J. van Eijk. *On the design of plate-spring mechanisms*. PhD thesis, Delft University of Technology, 1985.
- [89] J. L. Vaught, F. L. Cloutier, D. K. Donald, J. D. Meyer, C. A. Tacklind, and H. H. Taub. Thermal ink-jet printer, U.S. patent 4490728, 1984.
- [90] M. J. G. v.d. Molengraft, M. Steinbuch, and A. de Kraker. Integrating experimentation into control courses. *IEEE Control systems magazine*, 25(1):40–44, 2005.
- [91] R. A. A. Verkooijen. Exploration of a printhead alignment sensor, DCT 2006.068. Technical report, Technische Universiteit Eindhoven, 2006.
- [92] Q. Wang, P. Spronck, and R. Tracht. An overview of genetic algorithms applied to control engineering problems. In *Proceedings of the Second International Conference on Machine Learning and Cybernetics*, pages 1651–1656, 2003.
- [93] E. Webster. *Print Unchained: Fifty Years of Digital Printing, 1950-2000 and Beyond*. DRA of Vermont, Inc., 2001.
- [94] J. G. Webster. *Measurement, instrumentation and sensors handbook*. CRC Press, 1999.
- [95] G. Wolberg. *Digital Image Warping*. IEEE Computer Society Press, Los Alamitos, CA, USA, 1994.
- [96] O. Yaniv and M. Nagurka. Automatic loop shaping of structured controllers satisfying qft performance. *Journal of Dynamic Systems, Measurement, and Control*, 127:472–477, 2005.
- [97] S. L. Zoltan. Pulse droplet ejection system, U.S. patent 3683212, 1974.

Appendix A

Efficient Harmonic Disturbance Rejection via Multirate Notch Filtering

This chapter is based on [8]. A computationally cheap method is proposed to filter a harmonic series where the first harmonic has a fundamental frequency f_1 and the super harmonics are located at frequencies $2f_1, 3f_1, 4f_1, \dots$. The method is based on multirate filter banks. With this method a large amount of IIR notch filters can be implemented much more efficiently than by simply staggering single rate IIR notch filters without deteriorating the frequency range of interest.

A.1 Introduction

Periodic disturbances are often found in practical applications. The field of repetitive control [29] deals with control systems subjected to periodic disturbances and exploits the internal model principle [23]. Also in other research areas, like electric power systems, elimination of harmonics is addressed, [17, 70, 73].

Our interest lies in attenuating harmonic disturbance signals which is a subclass of periodic disturbances. The first harmonic is a sine at frequency f_1 , the so-called fundamental frequency, and the super harmonics are sines at the frequencies kf_1 with $k \in \{2, 3, 4, \dots\}$. Furthermore, it is assumed that the harmonic disturbances contain higher frequencies than the frequency range of interest. Consider for example control systems where the bandwidth frequency lies in the lower frequency

range with respect to the sampling frequency. Above the bandwidth frequency, the only objective is to attenuate disturbances, which does not restrict the sampling rate necessarily. The only requirement is that signals above the bandwidth frequency do not alias such that the signal content below the bandwidth is deteriorated.

To attenuate harmonics at higher frequencies than the frequency range of interest, a lowpass filter would be a natural choice to remove these harmonics. However, the selectivity of such filter is bad. The selectivity is defined as the slope of the magnitude response at the band edge. Signal content in the frequency range of interest will either be deteriorated significantly or the periodic disturbance will not be sufficiently attenuated unless the difference between the frequency range of interest and the disturbance frequency is more than 2-3 decades. The use of notch filters is much more desirable in that case because of their higher selectivity.

Compared to the low pass filter, the filter order will increase dramatically when notches are placed at each harmonic frequency resulting in a high computational cost. An alternative which is often used in repetitive control is a FIR comb filter. However, compared to IIR filters, the required number of taps or "order" of the FIR filter is very large to obtain equal selectivity properties, which leads to a high computational cost.

Here, an efficient method is proposed to implement a large number of IIR notch filters to remove harmonics. "Efficient" in the sense of good harmonic disturbance rejection and in the sense of a low computational cost. The method is based on multirate filter banks [77]. The concept of multirate filtering has first been introduced in [47]. A low order IIR filter can provide low deterioration at the frequency range of interest together with good robustness against small frequency variations of the harmonic frequencies. First, the structure and design of the filter bank will be presented. After that, some examples will be discussed. Finally, conclusions will be drawn.

A.2 Method

A.2.1 Multirate Digital Harmonic Notch Filter Bank

A digital filter with sampling rate f_s consisting of n notches placed at the frequencies:

$$f_k = \frac{k}{n+1}f_s, \quad k = 1, 2, \dots, n \quad (\text{A.1})$$

suppresses n harmonics with the first harmonic at $\frac{f_s}{n+1}$. The simplest construction of such a digital harmonic notch (DHN) filter consists of a zero at $e^{j2\pi\frac{f_k}{f_s}}$ and a

pole at $ae^{j2\pi\frac{fk}{f_s}}$ for $k = 1, 2, \dots, n$ and $a < 1$ for harmonic attenuation. If the same filter coefficients are used at lower rates, the notch width becomes larger. To obtain an equal notch width for the i th-rate filter of an m -rate filter bank, it can be easily derived that the zeros and poles $z_k, p_k, k = 1, 2, \dots, n$ should be:

$$z_k = e^{j2\pi\frac{fk}{f_{s,i}}} \quad (\text{A.2})$$

$$p_k = a^{(n+1)(i-1)} z_k \quad (\text{A.3})$$

with sampling rate of the i th-rate filter:

$$f_{s,i} = \frac{f_s}{(n+1)^{i-1}} \quad (\text{A.4})$$

If a signal is filtered with a DHN filter at a sampling rate of f_s ($i = 1$) and the output of this filter is filtered by a similar filter at a sampling rate of $\frac{f_s}{n+1}$ ($i = 2$), obtained by downsampling/decimation [77], then a 2-rate DHN filter bank is obtained which attenuates the harmonic frequencies:

$$f_k = \frac{k}{(n+1)^2} f_s, \quad k = 1, 2, \dots, (n+1)^2 - 1 \quad (\text{A.5})$$

This recursive process can be repeated resulting in an m -rate filter bank which filters:

$$N = (n+1)^m - 1 \quad (\text{A.6})$$

harmonics (see also Table A.1) with frequencies:

$$f_k = \frac{k}{(n+1)^m} f_s, \quad k = 1, 2, \dots, N \quad (\text{A.7})$$

Table A.1: Total amount of harmonic frequencies N filtered by the m -rate filter bank containing n notches at each rate.

N	$m=1$	$m=2$	$m=3$	$m=4$
$n=1$	1	3	7	15
$n=2$	2	8	26	80
$n=3$	3	15	63	255
$n=4$	4	24	124	624

To clarify this recursive process, an example is shown in Figure A.1. In this example, attenuation of the first 15 harmonics is obtained by applying two 3rd

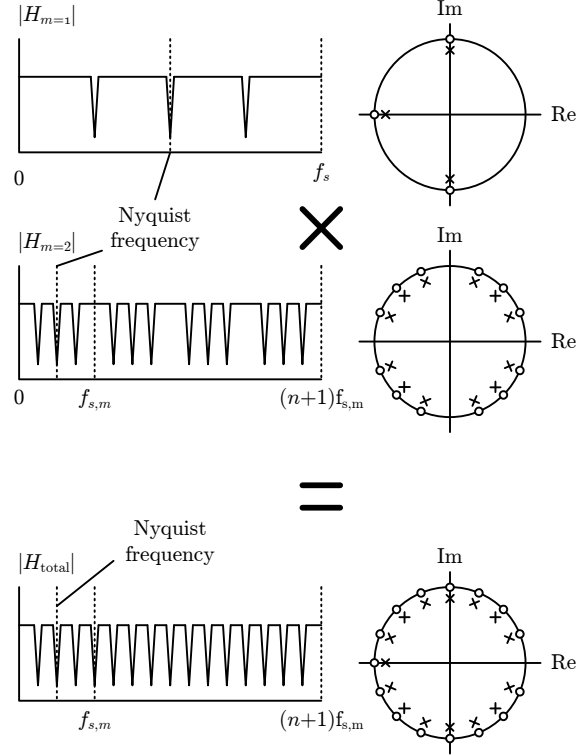


Figure A.1: Example of a multirate harmonic notch filter with $n = 3$ and $m = 2$. On the left, the magnitude of $H_{m=1}$, $H_{m=2}$ and $H_{total} = H_{m=1}H_{m=2}$ is shown. The equivalent single rate filter with sampling rate f_s is shown on the right in terms of zeros "o" and poles "x" in the complex plane.

order filters at a sampling rate of f_s and $\frac{1}{4}f_s$ respectively. It is obvious that this significantly reduces the computational cost compared to a 15th order filter at a sampling rate of f_s .

By choosing values for f_s , n and m , we obtain:

- the number of harmonic frequencies to be attenuated N
- the frequency of the first harmonic f_1
- the output sampling frequency $f_{s,m}$

which are computed by (A.4), (A.6) and (A.7) respectively.

Suppose $n = 1$, then one notch is located at the Nyquist frequency (half the sampling rate). Aliasing will occur if a disturbance frequency is higher than the

Nyquist frequency. Fortunately, this notch filter keeps on fulfilling its task. This can be easily verified by considering a disturbance signal with a frequency just above the Nyquist frequency. Also for $n > 1$, aliasing harmonics which coincide with notch frequencies will be filtered out.

A.2.2 Robustness to Frequency Variations

The distortion of the signal content of interest and the robustness to small frequency variations of the harmonics is determined by the selectivity of the basic notch filter which is multiplied for each notch location. The selectivity of the notch can be increased by increasing the order of the filter and/or using an Elliptic filter design approach [84]. A prototype notch filter can be created by designing a low pass filter with the cut-off frequency close to the Nyquist frequency with the function ELLIP in Matlab. The distance of the cut-off frequency to the Nyquist frequency determines the notch width and the distortion in the pass band. This prototype notch filter can then be shifted to all n frequencies (A.1). For each rate of the filter bank this procedure has to be carried out to obtain a multirate DHN filter as described before.

A.2.3 Filter Efficiency

The computational cost c of the filter bank is assumed to be proportional to the amount of evaluations of the filter multiplied by the filter order, hence:

$$\begin{aligned} c &\sim n f_s + n \frac{f_s}{n+1} + \dots + n \frac{f_s}{(n+1)^m} \\ &= n f_s \sum_{i=1}^m \frac{1}{(n+1)^{i-1}} \end{aligned} \quad (\text{A.8})$$

Values for some n and m are shown in Table A.2.

Table A.2: Cost expressed as the equivalent order at sampling rate f_s .

c	$m=1$	$m=2$	$m=3$	$m=4$
$n=1$	1	1.5	1.75	1.88
$n=2$	2	2.67	2.89	2.96
$n=3$	3	3.75	3.94	3.98
$n=4$	4	4.8	4.96	4.97

With this computational cost specification, the computational cost c_N of a conventional sequence of notches at a sampling rate f_s becomes:

$$c_N \sim N f_s \quad (\text{A.9})$$

The filter efficiency improvement $\frac{c_N}{c}$ follows from (A.6), (A.8) and (A.9):

$$\frac{c_N}{c} = \frac{(n+1)^m - 1}{n \sum_{i=1}^m \frac{1}{(n+1)^{i-1}}} = (n+1)^{m-1} \quad (\text{A.10})$$

From (A.4) and (A.10) follows that:

$$\frac{c_N}{c} = \frac{f_s}{f_{s,m}} \quad (\text{A.11})$$

which is a clear indication of the filter efficiency improvement, i.e. it is proportional to the output sampling rate reduction. In Table A.3, the filter efficiency improvement is shown for some values of n and m .

Table A.3: Filter efficiency improvement

$\frac{c_N}{c}$	$m=1$	$m=2$	$m=3$	$m=4$
$n=1$	1	2	4	8
$n=2$	1	3	9	27
$n=3$	1	4	16	64
$n=4$	1	5	25	125

A.2.4 Design Procedure

Now, the requirements that limit the choice for f_s , n and m are discussed. First of all, each hardware platform has its maximum sampling rate. Furthermore, the fundamental frequency f_1 of the harmonic disturbance and the number of harmonics are given. Next, signal content of interest at low frequencies f_{low} should be outputted with sufficient timing resolution, e.g. $f_{s,m} > 10f_{low}$. All combinations of n , m and f_s fulfilling these constraints can be checked. The parameter combination with the largest $\frac{c_N}{c}$ value is the most efficient implementation.

Example 1

Suppose that the highest frequency of interest $f_{low} = 10$ Hz, the fundamental frequency of the harmonics is $f_1 = 200$ Hz and the number of harmonics to be

suppressed is 24. Thus, the harmonic frequencies are $f_1 = 200$ Hz, $f_2 = 400$ Hz, $f_3 = 600$ Hz, ..., $f_{24} = 4800$ Hz. Furthermore, assume that the maximum sampling rate is $f_s \leq 6000$ Hz and the minimum output sampling rate is $f_{s,m} \geq 10f_{low}$.

Then, the optimum values for n , m and f_s are 2, 3, 5400 Hz respectively, implying an output sampling rate of $f_{s,m} = 600$ Hz, the number of notches $N = 26$ and an efficiency improvement $\frac{cN}{c}$ of 9.

Example 2

This example shows that the algorithm is also effective for a totally different choice of parameters. Furthermore, it is shown that the filter still works if the efficiency increase is very large. Finally, it is shown that a notch located at the Nyquist frequency filters disturbances just as good as a notch below the Nyquist frequency like in example 1.

For $f_{low} = 1$ Hz, $f_1 = 30$ Hz, 125 harmonics, $f_s \leq 5000$ Hz and $f_{s,m} \geq 10f_{low}$ the optimum values for n , m and f_s are 1, 7, 3840 Hz respectively. These values imply $N = 127$, $\frac{cN}{c} = 64$ and $f_{s,m} = 200$ Hz. In this case, the multirate DHN filter is 64 times more efficient than the equivalent singlerate filter. Such large efficiency gains can be achieved if f_{low} and f_1 are small with respect to the sampling rate f_s .

A.3 Simulations

A.3.1 Example 1

The filter input signal:

$$x = \sin 2\pi f_{low}t + \sum_{k=1}^N \sin(2\pi k f_1 t + S_k) \quad (\text{A.12})$$

with stochastic variable

$$S_k \sim U(0, 2\pi)$$

is subjected to the filter as described in Section A.2.4 with $n = 2$, $m = 3$ and $f_s = 5400$ Hz. For the basic filter, a 2nd order Elliptic filter with a pass band ripple of 10 dB and an attenuation of 80 dB is used. The frequency response magnitude for all rates are shown in Figure A.2. Also the equivalent single rate filter is shown in Figure A.2.

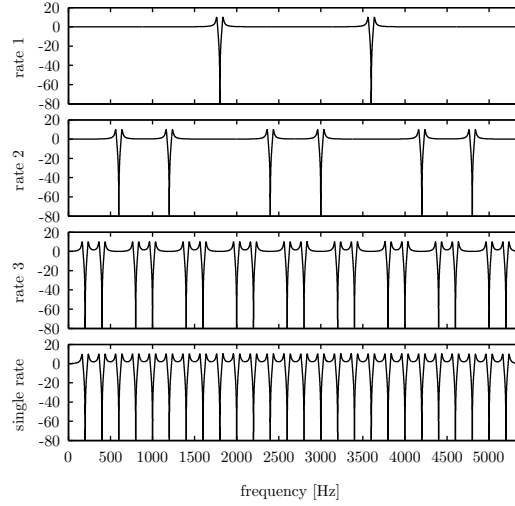


Figure A.2: Frequency response magnitude in dB of all filters in the multirate filter, rate 1: 5400 Hz, rate 2: 1800 Hz, rate 3: 600 Hz. The equivalent single rate filter is shown in the bottom figure.

The result of filtering one realization of (A.12) with the multirate filter is shown in Figure A.3 and the result of filtering the same realization of (A.12) with the equivalent single rate filter is shown in Figure A.4. Comparing Figure A.3 and Figure A.4, we see that the filter output is nearly the same, only the output sampling rate is lower for the multirate filter.

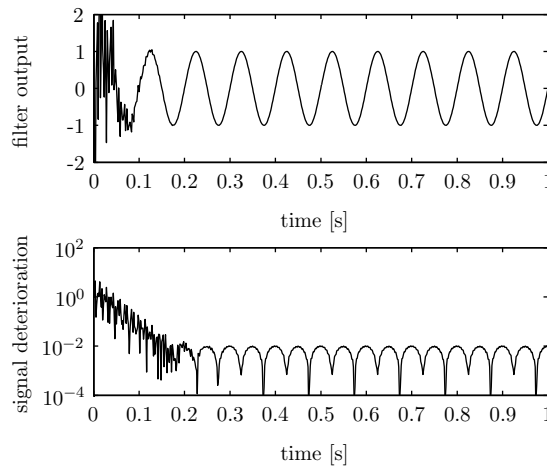


Figure A.3: Result of filtering a realization of (A.12) using the multirate filter.

In Figure A.5, the step response of the multirate filter and the equivalent singlerate filter is compared. It can be observed that the multirate filter has less overshoot

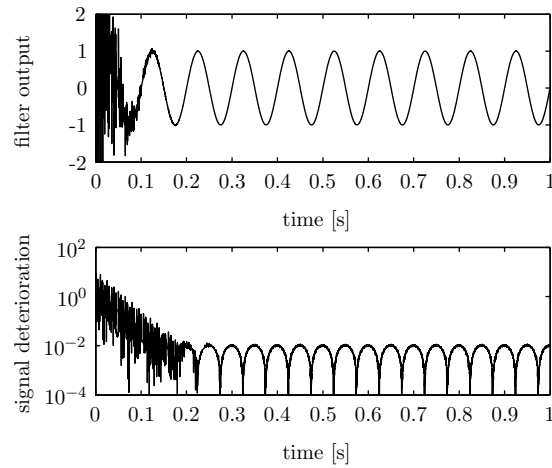


Figure A.4: Result of filtering a realization of (A.12) using the equivalent single rate filter.

than the singlerate filter. All other simulations conducted, showed the same result with varying filter settings.

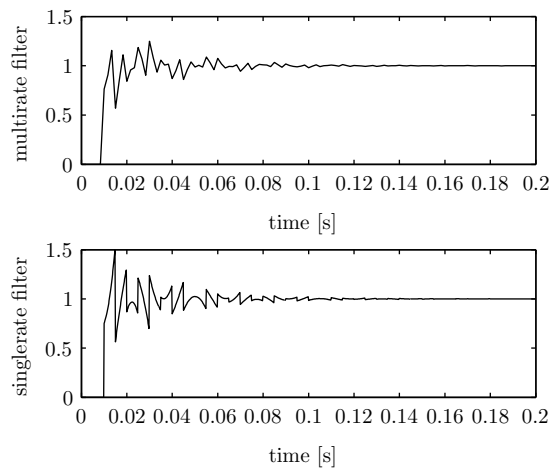


Figure A.5: Step response of the multirate and equivalent singlerate filter.

If f_1 is increased by 0.1 % in (A.12), then the result as shown in Figure A.6 is obtained. The performance has decreased somewhat, however, there is still a clear separation of the sine at f_{low} and the harmonic disturbances.

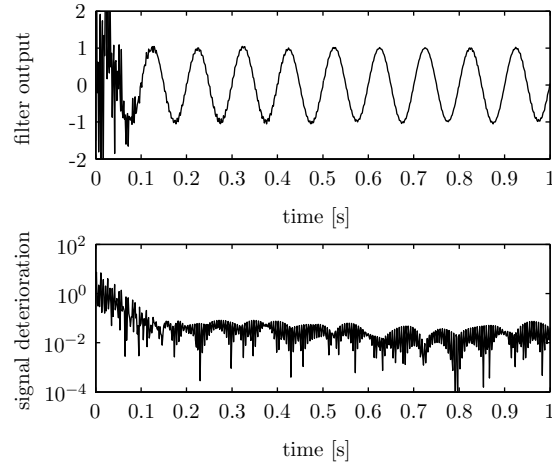


Figure A.6: Result of filtering a realization of (A.12) with a 0.1 % frequency shift of f_1 using the multirate filter.

A.3.2 Example 2

Next, the example of Section A.2.4 is considered where n , m and f_s are 1, 7 and 3840 Hz respectively. For the basic filter, a 2nd order Elliptic filter is used with a pass band ripple of 3 dB and a stop band ripple of 80 dB.

The frequency response magnitude of the 3 rates of this filter and the equivalent single rate filter are shown in Figure A.7.

Again, (A.12) is subjected to the filter with $f_{low} = 1$ Hz and $f_1 = 30$ Hz, so the input signal is a sine at 1 Hz with 127 harmonics with the same amplitude. The results are shown in Figure A.8.

A.4 Conclusions

It has been shown that the multirate DHN filter performs just as good as the equivalent single rate filter, however with a much lower computational cost at the cost of a reduced output sampling rate. It was found that the computational cost reduction is proportional to the ratio of the sampling rate and the output sampling rate. Furthermore, the multirate DHN filter shows less overshoot than the equivalent single rate filter.

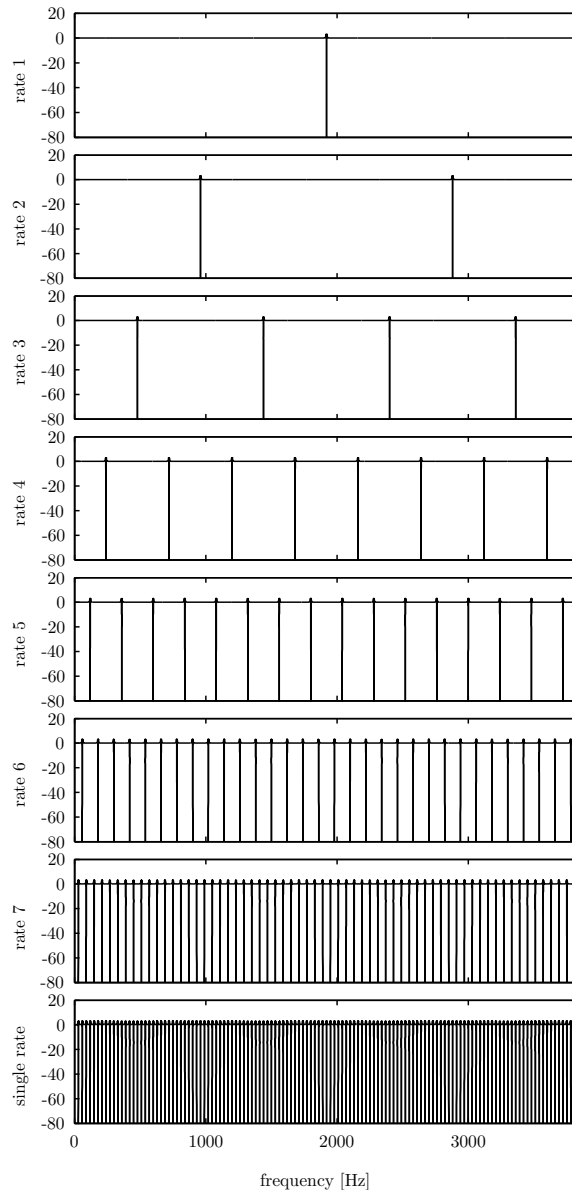


Figure A.7: Frequency response magnitude in dB of all filters in the multirate filter, rate 1: 3840 Hz, rate 2: 1920 Hz, rate 3: 960 Hz, rate 4: 480 Hz, rate 5: 240 Hz, rate 6: 120 Hz, rate 7: 60 Hz. The equivalent single rate filter is shown in the bottom figure.

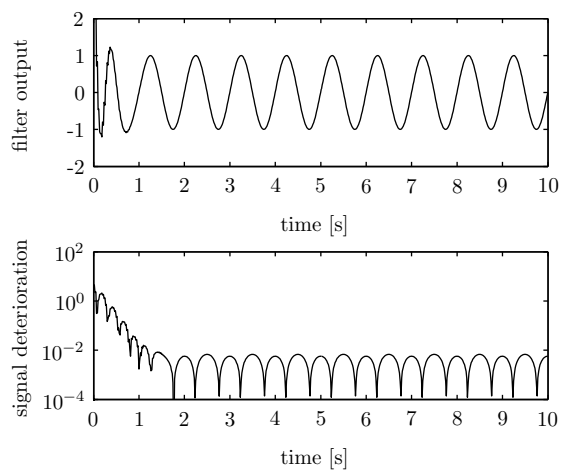


Figure A.8: Result of filtering a realization of (A.12) using the multirate DHN filter.

Appendix B

Alternative Printhead Alignment Sensor Methods

A lot of methods exist to measure the misalignment of printheads [71, 91]. The measurement range should be at least 300 μm with an accuracy less than 10 μm for sufficient printing accuracy. This chapter will give a global overview of some sensors, that are widely used in industry in many diverse applications. The focus lies on non-contact measuring the printhead position with respect to a string because of the advantages regarding robustness to thermal effects.

B.1 Inductive Sensors

Inductive sensors rely on electromagnetic fields and the magnetic properties of materials. Inductive displacement sensors are robust and compact and insensitive to humidity and dust. Inductive sensors can be classified as self-generating or passive [94]. For the self-generating type, a voltage is induced in the conductor when a relative motion occurs between the conductor and a magnetic field. Passive transducers require an external power source for sensing a movement. In the next sections some inductive sensors are presented based on [3, 94].

B.1.1 Basic Inductive Sensor

A simple magnetic circuit for an inductive sensor is shown in Figure B.1. The circuit consists of a ferromagnetic core with a coil wound on it. The coil drives

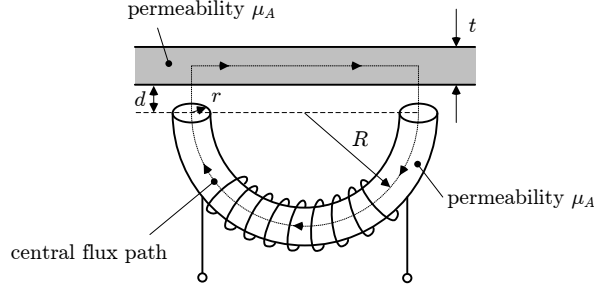


Figure B.1: Basic magnetic circuit of an inductive sensor.

a flux through the magnetic circuit and the air gap. The magnetic flux Ψ in Wb with zero air gap becomes:

$$\Psi = \frac{n^2 i}{\mathfrak{R}} \quad (\text{B.1})$$

Herein, n is the number of turns of the coil and \mathfrak{R} is the reluctance in A/wb (resistance of the material to the magnetic field) which satisfies the relation:

$$\mathfrak{R} = \frac{l}{\mu \mu_0 A} \quad (\text{B.2})$$

where l = the total length of the flux path in m
 μ = the relative permeability of the magnetic circuit material [-]
 μ_0 = the permeability of free space in H/m ($= 4\pi \cdot 10^{-7}$)
 A = the cross-sectional area of the flux path in m^2

The presence of the air gap causes a large increase in circuit reluctance and a corresponding decrease in flux. Hence, a small variation in the air gap d results in a measurable change in inductance. A sensor like this is called a single-coil variable-reluctance transducer. The total reluctance of the magnetic circuit is the sum of the individual reluctance of the core \mathfrak{R}_C , air gap \mathfrak{R}_G and armature \mathfrak{R}_A :

$$\begin{aligned} \mathfrak{R}_T &= \mathfrak{R}_C + \mathfrak{R}_G + \mathfrak{R}_A \\ &= \mathfrak{R}_0 + kd \end{aligned} \quad (\text{B.3})$$

where \mathfrak{R}_0 is the total reluctance of the core and the armature:

$$\mathfrak{R}_0 = \frac{R}{\mu_0 r} \left(\frac{1}{\mu_c r} + \frac{1}{\mu_A t} \right) \quad (\text{B.4})$$

and kd is the reluctance of the air gap with:

$$k = \frac{2}{\mu_0 \pi r^2} \quad (\text{B.5})$$

in A/Wbm. The inductance L in H can be written as:

$$L = \frac{L_0}{1 + \alpha d} \quad (\text{B.6})$$

where L_0 is the inductance at zero air gap in H, and α is equal to $\frac{k}{\mathfrak{R}_0}$ in m^{-1} .

Equation B.6 shows that there is a non-linear relation between the inductance L and the size of the air gap d . Therefore this basic sensor is not frequently used.

B.1.2 Variable Differential-Reluctance Sensor

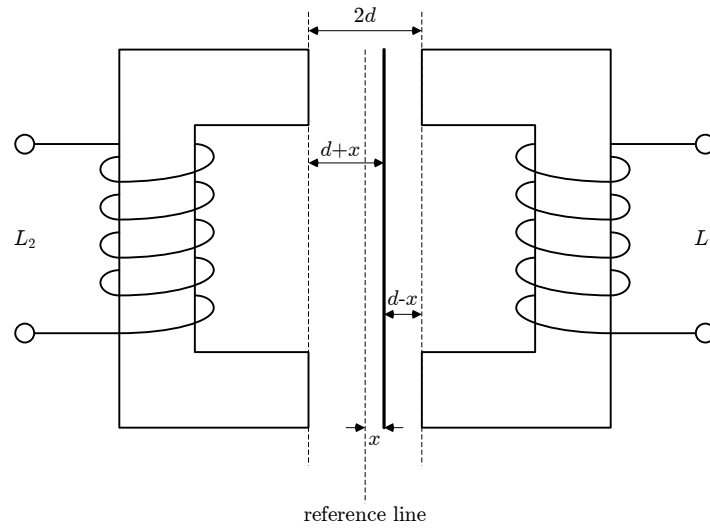


Figure B.2: Variable-differential reluctance sensor.

The problem of non-linearity can be overcome by modifying the single coil system into a variable-differential reluctance sensor as shown in Figure B.2. This sensor consists of an armature moving between two identical cores, which are separated by a fixed distance of $2d$. Now, (B.6) can be written for both coils as:

$$\begin{aligned} L_1 &= \frac{L_{01}}{1 + \alpha(d - x)} \\ L_2 &= \frac{L_{02}}{1 + \alpha(d + x)} \end{aligned} \quad (\text{B.7})$$

In this case the relation between the reluctance of the two cores is still non-linear, but the sensor now can be incorporated in a so-called AC deflection bridge to give a linear output for small movements. However, performance is deteriorated by external magnetic fields. In general, variable reluctance transducers have small ranges and are used in specialized applications such as pressure transducers. Magnetic forces imposed on the armature are quite large and this severely limits their application.

B.1.3 Eddy Current Transducer

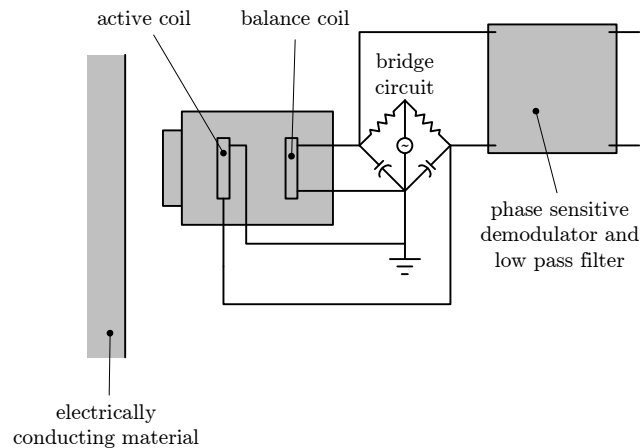


Figure B.3: Eddy current transducer.

Inductive sensors based on eddy currents are mainly probe types, containing an active coil and a balance coil, as shown in Figure B.3. The active coil is influenced by the presence of the conducting target. Probes are commercially available with full-scale diameter ranging from 0.25 mm to 30 mm and a maximum resolution of 0.1 μm . Flat targets must have the same surface area as the probe or larger. The surface area of curved-surface targets, has to exceed three or four times the surface area of the probe to ensure reliability. This will complicate measuring the position of a thin string.

B.2 Capacitive Sensors

Capacitive sensors are, like their inductive counterparts, extensively used in industrial and scientific applications. They are based on changes in capacitance in response to physical variations. They satisfy the requirements of applications where high linearity and wide ranges (from a few centimeters to a couple of

nanometers) are needed. In the following sections the main sensing principles of capacitive sensors are presented as described in [3] and [94].

B.2.1 Basic Capacitive Sensor

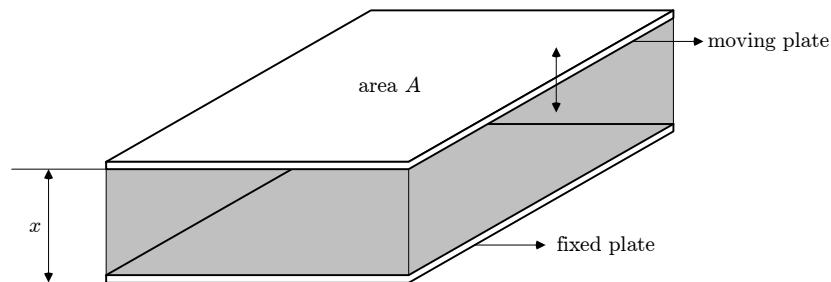


Figure B.4: Basic capacitive sensor.

A capacitor displacement sensor which is made from two flat plates with a variable distance apart is shown in Figure B.4. By moving one of the plates of the capacitor in vertical direction the capacitance will change. The relation between the distance and the capacitance of the transducer can be expressed by:

$$C(x) = \frac{\varepsilon A}{x} = \frac{\varepsilon_r \varepsilon_0 A}{x} \quad [\text{C}] \quad (\text{B.8})$$

where

- ε = the dielectric constant or permittivity $[\frac{\text{C}}{\text{m}}]$
- ε_r = the relative dielectric constant $[-]$
- ε_0 = the dielectric constant of vacuum $[\frac{\text{C}}{\text{m}}]$
- x = the distance of the plates $[\text{m}]$
- A = the effective area of the plates $[\text{m}^2]$

The sensitivity of the capacitance with respect to changes in plate separation follows from (B.8):

$$\frac{dC}{dx} = -\frac{\varepsilon_r \varepsilon_0 A}{x^2} \quad \left[\frac{\text{C}}{\text{m}} \right] \quad (\text{B.9})$$

This sensor is often used for measuring small incremental displacements without making contact with the object.

B.2.2 Differential Capacitive Sensor

Like inductive sensors, the non-linearity in capacitive sensors can be removed by using differential arrangements as shown in Figure B.5. For a displacement x , we

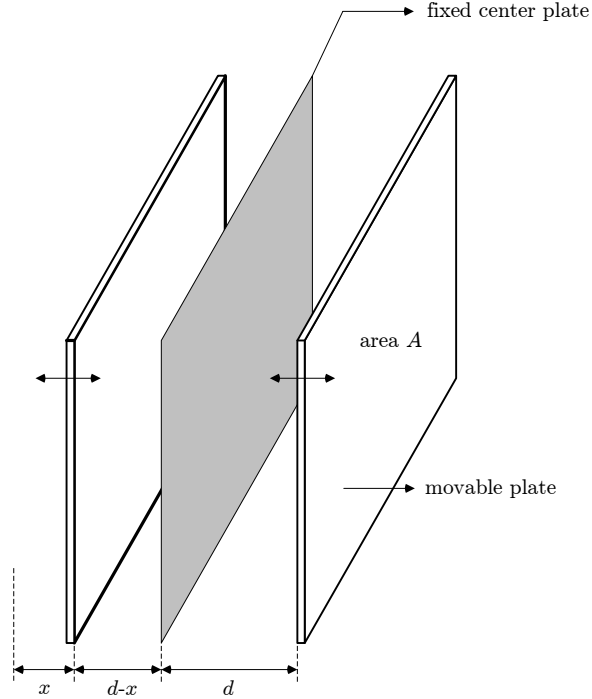


Figure B.5: Differential capacitive sensor.

obtain:

$$\Delta C = C_1 - C_2 = \frac{\varepsilon_r \varepsilon_0 A}{d-x} - \frac{\varepsilon_r \varepsilon_0 A}{d+x} = 2 \frac{\varepsilon_r \varepsilon_0 A x}{d^2 - x^2} \quad (\text{B.10})$$

and:

$$C = C_1 + C_2 = \frac{\varepsilon_r \varepsilon_0 A}{d-x} + \frac{\varepsilon_r \varepsilon_0 A}{d+x} = 2 \frac{\varepsilon_r \varepsilon_0 A d}{d^2 - x^2} \quad (\text{B.11})$$

From (B.10) and (B.11) we obtain:

$$\frac{\Delta C}{C} = \frac{x}{d} \quad (\text{B.12})$$

Equation (B.12) shows that the differential capacitive sensor is linear unlike the basic capacitive sensor. There is not a useful type of capacitive sensor for usage in combination with a string. The capacitive sensor principles are based on flat plates. A thin string has not enough material for good measurement of the capacitance.

B.3 Hall Effect Sensor

In [71], the use of Hall effect sensors is investigated to determine the string position. To obtain a Hall effect, a current should be applied to the string. The magnetic field of a straight current-carrying conductor can be calculated using the law of Biot and Savart:

$$d\vec{B}_P = \frac{\mu_0}{4\pi} \frac{I d\vec{l} \times \hat{r}}{r^2} \quad (\text{B.13})$$

where the magnetic field \vec{B}_P at point P is induced by the part of the string with length dl and direction $d\vec{l}$ equal to the direction of the current I , the unit vector \hat{r} points from that part of the string towards the point P , and the permeability of free space $\mu_0 = 4\pi \cdot 10^{-7}$ H/m. An illustration is shown in Figure B.6. Using

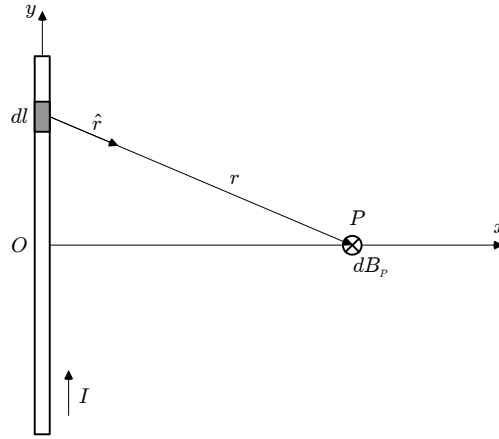


Figure B.6: Illustration of Equation (B.13).

(B.13) and assuming that the distance of the string to the point P is much smaller than the string length, we obtain:

$$B = \frac{\mu_0 I}{2\pi r} \quad (\text{B.14})$$

By measuring B with the Hall effect sensor and the current I which can be chosen freely, we obtain a distance estimate of r . In Figure B.7, a possible setup is shown. The relation between (r_1, r_2) and (x, y) for this setup is:

$$r_1 = \frac{a^2 + 2ax + x^2 + y^2}{a + x} \quad (\text{B.15})$$

$$r_2 = \frac{b^2 + 2by + x^2 + y^2}{b + y} \quad (\text{B.16})$$

According to [71], an accuracy of $2 \mu\text{m}$ can be obtained.

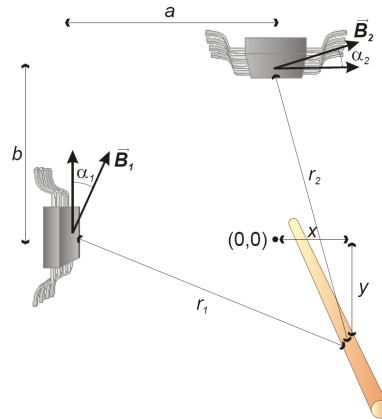


Figure B.7: String position measurement using two Hall effect sensors.

B.4 Optical Sensors

In the next sections the fundamentals of some optical detectors as described in [3, 18, 44, 78, 94] are explained.

B.4.1 Fotonic Sensor

A fotonic sensor consists of a probe with optical fibres, a light source and a light detector. The optical fibres in the probe are divided in two groups: transmitting and receiving fibres, see Figure B.8.

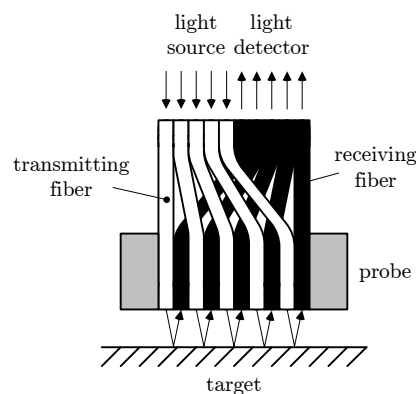


Figure B.8: Optical fibres.

The first group is exposed to a light source and carries the light to the probe tip where the light will be emitted and reflected. At zero gap (contact) there

is no light picked up by the receiving fibres, so the output is zero. The light intensity increases with increasing probe-to-target distance until the entire face of the receiving fibre is covered by the reflected light. After that, the sensor output decreases because the light intensity decreases with increasing distance. Fotonic sensors are commercially available with a measurement range from a few μm to ± 0.5 cm, and with probe diameters between 0.5 and 7 mm.

B.4.2 CCD and APS Sensors

Instead of a direct distance measurement, it is also possible to measure the string position with imaging techniques using a charge coupled device (CCD). A CCD is an integrated circuit which is made of silicon. It can receive charge via the photoelectric effect.

The CCD contains photodiodes which convert light energy into electric charge. A basic CCD sensor is shown in Figure B.9. Due the interaction of photons (light energy) with silicon atoms electrons are generated. These electrons are stored in a potential well. When a photon strikes a silicon atom in or near a photodiode it produces a free electron and a "hole" in the silicon crystalline lattice, created by the temporary absence of the electron. The free electrons are stored in the potential well, while the "holes" are forced away from the well. After the electrons have been collected, a voltage potential is applied to the gates.

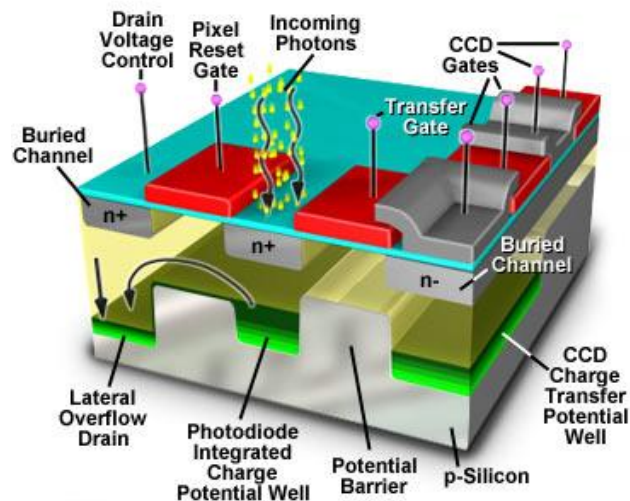


Figure B.9: Illustration of a CCD sensor [41].

A competitive sensor, based on the same principles is the active pixel sensor (APS). According to [44], the performance of the APS is comparable to the CCD

technology. The APS sensor is based on CMOS (complementary metal-oxide-semiconductor) technology, which is the dominant technology for chip making. Since the APS is inherently CMOS compatible, it is easy to integrate on-chip timing, control and drive electronics, reducing system cost and complexity. The cost of fabricating a CMOS wafer is one-third the cost of fabricating a similar wafer using a specialized CCD process. Another advantage with respect to CCD is that APS has a lower power consumption.

B.5 Conclusions

Inductive and capacitive sensors are compact, robust, but sensitive to environmental factors. The main fundamentals of both types of sensors can be used for measuring the distance of the printhead with respect to a string. The best commercially available solution seems to be a probe based on eddy currents. However, it would be better in that case to replace the string by a flat surface, to eliminate errors due to cross-axis movements. It is difficult to construct this, because of deformations of the surface on a long distance. When a string is used, the diameter of the string has to exceed three or four times the probe diameter, which causes a restriction on the lowest natural frequency of the string due to a limiting string tension. This may be a problem in the dynamical system, when the string harmonics have to be filtered out.

The optical sensors can be used with any kind of light source. The fotonic sensor can be used in the same sense as the eddy current based probe. Again the measured surface has to be at least the size of the probe diameter. With the CCD and the APS sensors, a position measurement based on the shadow of the object could be established. Although APS sensors are cheap, a cheap CCD was also available dedicated for this application while the performance of CCD sensors are slightly better.

The Hall effect also provides enough accuracy, however, it imposes more restrictions to the string used, because a current should flow through the wire.

Appendix C

Optimization Aided Loop Shaping for Motion Systems

This chapter is based on [7]. An approach is proposed which improves the quality and speed of manual loop shaping. Loop shaping is an iterative and creative controller design procedure where the control engineer uses frequency response function (FRF) data of the plant to shape the open loop response such that it satisfies closed loop stability, performance and robustness specifications. As an assisting tool in manual loop shaping, we add a global optimization method, in the form of a genetic algorithm, where the objective function resembles as good as possible what the control engineer wants. As a result, the tuning process is substantially accelerated. The approach has been implemented in a Matlab-based control tuning tool 'Shape-It'.

C.1 Introduction

Loop shaping in the frequency domain [24, 60] is a widely used method by control engineers in practice. It is an iterative and creative process to achieve desired closed loop behavior in terms of stability, performance and robustness to model uncertainties and disturbances. The main advantages of frequency loop shaping are freedom of choice of the controller structure and the possibility for the control engineer to assess his requirements directly after each adjustment to the controller. On the other hand, a lot of optimization based methods exist that automate the controller design process, such as LQ, LQG [1], \mathcal{H}_2 and \mathcal{H}_∞ [19]. Ideally, frequency loop shaping could be replaced totally by these methods. However,

the requirements of the control engineer always have to be compromised due to the limitations each method has, such as the class of controllers which can be handled, the performance criteria which can be optimized and to what extent disturbance models can be incorporated. The result is a suboptimal controller in view of the actual control engineer's requirements. Therefore, frequency loop shaping remains a popular, often applied method, in particular for SISO systems.

Automatic loop shaping is an active field of research [14, 30, 50, 80, 96]. The main challenge is to formulate the objective function for optimization such that it resembles the requirements of the control engineer as good as possible. Often, and certainly in the case of fixed order or structured controllers, this results in a NP-hard optimization problem where the optimal solution can be approximated by global optimization methods, e.g. Monte-Carlo, simulated annealing [52], evolutionary algorithms, such as genetic algorithms [38], swarm-based optimization algorithms, such as particle swarm optimization [49] etc. These algorithms are all computationally expensive and therefore they most often do not come up with the global optimal solution within an acceptable time span. Nevertheless, the suboptimal solution found can be good enough.

Here we exploit the synergy of manual frequency loop shaping and optimization aid via a genetic algorithm such that the control engineer is able to quickly design a high performance controller. The optimization aid is seen as an assisting tool to speed up the iteration process and not as a replacement for manual loop shaping. This approach enables the control engineer to use its expertise *during* the semi-automated iteration process. A software tool has been written in Matlab for SISO controller design which enables the user to: select plant data which can be a SISO model, SISO FRF-data or multiple SISO FRF-data, choose a set of filters for the controller, optimize a selection of them where some key parameters for high gain feedback loop shaping can be set, carry out the loop shaping iteration process with optimization aid until an acceptable result is obtained, and finally, export the resulting controller to a discretized Simulink block ready-to-use for simulations and experiments.

First, high gain feedback loop shaping is described in short. After that, the optimization aid is presented. Next, the loop shaping tool is presented and a loop shaping example with this tool is given. Finally, conclusions are drawn.

C.2 High Gain Feedback Loop Shaping

A standard feedback control loop is shown in Figure C.1. For SISO LTI systems, the transfer function from reference $r(t)$ to output $y(t)$, i.e. the complementary sensitivity function, is:

$$T(s) = \frac{Y(s)}{R(s)} = \frac{P(s)C(s)}{1 + P(s)C(s)} \quad (\text{C.1})$$

where $Y(s)$ and $R(s)$ are the Laplace transforms of $y(t)$ and $r(t)$ respectively, $P(s)$ is the plant model and $C(s)$ is the controller model.

From now on we only consider steady state relations for periodic signals, i.e. $s = j\omega$. The idea of high gain feedback is to increase the loop gain $P(j\omega)C(j\omega)$ such that $y(t)$ resembles $r(t)$. From (C.1) it is easy to see that $\frac{Y(j\omega)}{R(j\omega)} \approx 1$ and thus $\frac{y(t)}{r(t)} \approx 1$ for $|P(j\omega)C(j\omega)| \gg 1$.

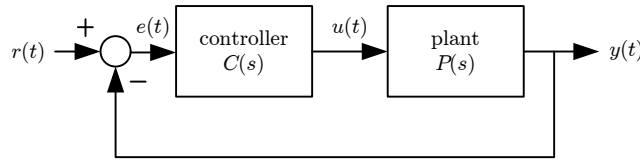


Figure C.1: Scheme of a standard feedback control loop.

In practice, the allowable loop gain is limited by e.g. the limited actuator capacity, parasitic plant dynamics and loop delay due to digital implementation. Moreover, the loop gain is always decreased further to obtain robustness to plant uncertainties and better disturbances attenuation above the bandwidth.

C.2.1 Requirements of the Control Engineer

Define the crossover frequency ω_{bw} as the frequency where $|P(j\omega)C(j\omega)|$ crosses the 0 dB level the first time, called here "the bandwidth":

$$\omega_{\text{bw}} = \inf_{\omega} |P(j\omega)C(j\omega)| \leq 1 \quad (\text{C.2})$$

Below the bandwidth we have $|P(j\omega)C(j\omega)| > 1$, hence $\frac{y(t)}{r(t)} \approx 1$. If most of the frequency content of the reference signal is in this region, the reference can be tracked well using this feedback controller. However, in practice, tracking performance for motion systems is primarily determined by feedforward design. The main goal of a feedback controller design is disturbance rejection which can be achieved by high gain feedback implying a high bandwidth.

Besides this performance specification, the control engineer requires stability and robustness to plant uncertainties. For non-parametric FRF-data, the Nyquist stability criterion [24] can be applied to guarantee stability of the closed loop system. Robustness against plant uncertainties is imposed by limiting the minimal distance to the point -1 in the Nyquist plot which is equal to limiting the maximum magnitude of the sensitivity function:

$$S(s) = \frac{1}{1 + P(s)C(s)} \quad (\text{C.3})$$

This maximum magnitude of the sensitivity function, also called the modulus margin [56], is:

$$\sup_{\omega} |S(j\omega)| \leq \alpha \quad (\text{C.4})$$

where $\alpha = 6$ dB is a common choice. For $\alpha = 6$ dB, the modulus margin also implies a phase margin of 30° and a gain margin of 6 dB. However, the opposite is not true so this makes the modulus margin the most important margin for controller design.

C.2.2 Objective Function For Loop Shaping

For optimization, we want to have an objective function which resembles the requirements of the control engineer as good as possible. The available data of the plant is assumed to be (non-parametric) FRF-data of a stable SISO system. The proposed objective function implements the following criteria:

- criterion 1: a target bandwidth
- criterion 2: low gain above the bandwidth
- criterion 3: high gain below the bandwidth
- criterion 4: constraint on the gain, phase and modulus margin
- criterion 5: constraint that the open loop should cross the 0 dB once

The constraint on the phase margin and criterion 5 are sufficient conditions to imply stability. The constraint on the modulus margin implies robustness against unstructured plant uncertainty. The gain margin is not necessary for optimization, nevertheless, it is a commonly used criterion by the control engineer and therefore it is added to the constraints.

The objective function has to combine all criteria into one value indicating the quality of an arbitrary controller. Criterion 1 can be implemented by a quadratic objective function with the minimum at ω_{target} :

$$J_{\text{bw}} = w_1 (\omega_{\text{bw}} - \omega_{\text{target}})^2 \quad (\text{C.5})$$

where w_1 is a weighting factor.

To stimulate low gain for all frequencies above the bandwidth (criterion 2), the mean gain in dB is added to the objective function. Similarly, the mean gain in

dB is added for frequencies below the bandwidth which accounts for criterion 3:

$$\begin{aligned}
 J_{\text{gain}} &= w_2 \sum_{\omega > \omega_{\text{bw}}} 20 \log |P(j\omega)C(j\omega)| \\
 &\quad - w_3 \sum_{\omega \leq \omega_{\text{bw}}} 20 \log |P(j\omega)C(j\omega)|
 \end{aligned} \tag{C.6}$$

where w_2 and w_3 are weighting factors.

The choice for w_1 , w_2 and w_3 is crucial. From a control engineer's point of view, it is logical to first obtain approximately the required bandwidth and after that increase the gain below the bandwidth and decrease the gain above the bandwidth, hence the weighting factor of the bandwidth criterion should be relatively large if the current bandwidth is not close to the target bandwidth. A proper choice for w_1 is:

$$w_1 = \frac{1}{\omega_{\text{target}}^2} \tag{C.7}$$

which normalizes the bandwidth criterion such that $J_{\text{bw}} = 0.01$ for 10% bandwidth deviation. Factors w_2 and w_3 are chosen to be $\frac{1}{2000}$ such that the contribution to J_{gain} for a mean value of 20 dB, which is the order of magnitude, is also 0.01. Because criterion 2 and 3 are linear and criterion 1 is quadratic, larger deviations of the bandwidth implies $J_{\text{bw}} \gg J_{\text{gain}}$, hence the bandwidth criterion is dominant. Constraints (criterion 4 and 5) are incorporated in the objective function by returning a large penalty $J_{\text{penalty}} = 10^{10}$ plus the amount of constraint overshoot $J_{\text{overshoot}}$ which can be for example the modulus margin. The total objective function J becomes:

$$J = \begin{cases} J_{\text{bw}} + J_{\text{gain}} & \text{if all constraints are satisfied} \\ J_{\text{penalty}} + J_{\text{overshoot}} & \text{if at least one constraint is} \\ & \text{not satisfied} \end{cases} \tag{C.8}$$

C.2.3 Optimization Aid

The objective function, as described in the previous section, is a nonlinear function for which the global optimum solution is difficult to find when using non-parametric FRF-data. A genetic algorithm [38] is chosen to deal with this problem because the effectiveness of the method has often been shown in literature [83, 92]. In short, it is an evolutionary algorithm which searches for the optimum solution by mimicking the evolution process in nature. A population of candidate solutions evolves where better solutions have more chance to reproduce itself by mutation and crossover operations. This way, candidate solutions can improve each generation until an adequate solution is found. For implementation, the "Genetic

Algorithm and Direct Search Toolbox” of Matlab [62] is used. Details of how the parameters of the genetic algorithm are chosen will not be further discussed.

Advantages of this optimization method are:

- freedom in choosing the objective function. The objective function can be chosen to be an arbitrary function of all criteria such that the output value represents the performance of the controller well.
- freedom of choosing the controller structure and its parameters with its bounds. The parameters can be chosen such that they have physical meaning which can be easily interpreted by the control engineer. Furthermore, the control engineer can easily fix some parameters and optimize only the rest which is a powerful method to include knowledge and expertise of the control engineer into the controller design.
- it explores the specified parameter space where it can explore solutions that the control engineer did not immediately think of.

Because in general a lot of function evaluations (>10000) are needed for global optimization methods to obtain a good solution, it is essential that the calculation time of the objective function is as short as possible. For the objective function as described in the previous section, subjected to FRF-data, tests have shown that the amount of function evaluations lies between 100 and 1000 per second depending on the controller complexity and the frequency gridding. The result is that the optimization method for the examples shown here comes up with a good solution in less than a minute which is considered fast with respect to manually iterating a set of controller parameters.

Moreover, for our goal it is not essential that after a single run of the algorithm the global optimal solution is found. The optimization is used as a tool which helps improving the controller during the loop shaping iteration process. During the optimization, the control engineer can observe the performance of the controller and stop the optimization at any time. Combined with the control engineer’s expertise, convergence to the optimal controller is accelerated.

C.3 Loop Shaping Strategy

In this section we will compare classical loop shaping to loop shaping combined with an optimization tool.

C.3.1 Classical Loop Shaping

In classical loop shaping, the control engineer performs the following steps:

1. Measure the FRF from an experimental setup or extract FRF-data from a model by computing $P(j\omega)$ for a selection of values for ω .
2. Select a controller structure.
3. Stabilize the control loop.
4. Increase the bandwidth by changing the parameters of the controller until one of the constraints has been reached.
5. If the controller is not yet good enough, change the controller structure by adding filter elements and go back to step 3.
6. Validate the controller performance with simulations and experiments.

The expertise of the control engineer, which allows him to use a priori knowledge in the design process, determines the quality of the final resulting controller. In practice, step 3 and 4 are time consuming and have to be repeated several times to obtain a satisfying result.

C.3.2 Optimization Aided Loop Shaping

With respect to classical loop shaping, optimization aid enables the following features:

1. OPTIMIZING CONTROLLER PARAMETERS:

If there are only a few parameters it is easy for the control engineer to tune the controller using the rules of thumb at hand. However, if the controller complexity increases, it is not that straightforward anymore how to manually tune the controller. In that case, an optimization algorithm can be much faster in improving the controller parameters. A first guess of how the controller should look like can be obtained by specifying the controller blocks, the desired bandwidth and the gain, phase and modulus margin and then run the optimization algorithm. The optimization process can be interrupted by the user at any time, after which the intermediate controller optimization result will in general be better than before optimization. In this way, step 3 and 4 are done much quicker, so the control engineer focuses more onto how to change e.g. the controller structure.

2. LOCAL NOTCH FITTING

Experience has shown that the optimization algorithm has difficulties with using notches well. The reason for this is their local manifestation in the frequency domain. The parameters have to be set quite accurate such that the notch has the desired effect, e.g. removing a resonance peak. Due to this locality, a global optimization method has difficulties to find these parameter

values. On the contrary, an experienced control engineer detects such a local problem immediately. Therefore, notch tuning is implemented as a separate optimization problem in which the user indicates the frequency range of interest. For placing a notch, the objective is most often removing a resonance peak. With specification of the frequency interval of interest, the inverse of the notch can be fitted onto the resonance. This way, such a difficult problem from a global point of view is changed in an easy problem from a local point of view.

Within a few seconds the optimal notch is computed which again accelerates the convergence to a high performance controller.

3. SELECTED OPTIMIZATION

A major benefit of using optimization during loop shaping is to optimize only a selection of controller blocks of the whole controller. This will be made clear with a few examples. Suppose that all poles and zeros lie on the correct spot except that the gain is not correctly tuned yet regarding the constraints. By optimizing only the gain, the gain is tuned such that the constraints are just met.

Another possibility is to add an integrator or low pass filter to the controller and then only optimize these filters together with the gain. This way it is possible to increase the gain below the bandwidth and decrease the gain above the bandwidth without deteriorating e.g. a correctly fitted notch filter.

Another example is to add a controller block with fixed parameters and then optimize only the other controller parameters. Suppose that the control engineer knows that disturbances are present at high frequencies. By adding a low pass filter with the pole at a lower frequency, the optimization algorithm will try to achieve the best result under this controller limitation. In such a way a priori knowledge about the plant and disturbances can be incorporated in the loop shaping procedure.

C.4 Application Description

An application, called *Shape It*, has been written in Matlab v7 suited for optimization aided loop shaping. The GUI of *Shape It* is shown in Figure C.2. The main features of it are described below:

- Class of plants: SISO LTI models (TF, SS or ZPK systems) or FRF-data can be loaded from an example list, the workspace or a file. For SISO LTI models, the frequency range and the amount of data points can be chosen freely, whereas for FRF-data, frequency information has to be included.
- Class of controllers: controller blocks which can be added to the controller are: gain, integrator, lead/lag, 1st order low pass, 2nd order low pass, notch

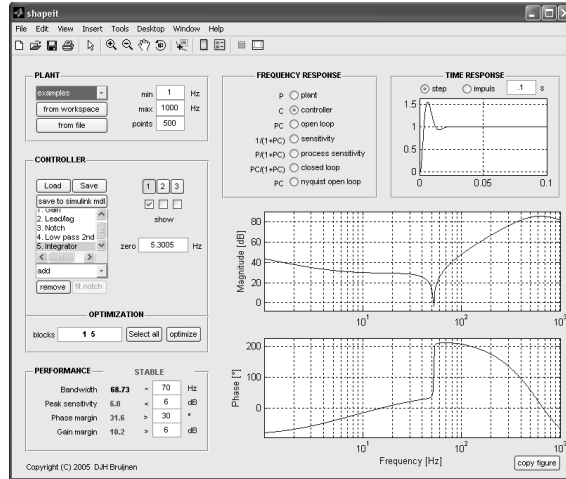


Figure C.2: GUI of Shape It.

and PD. Parameter values can be set per controller block. Load/Save functionality is included. Furthermore, if a notch controller block is selected it can be fitted onto a resonance peak by pressing the "fit notch" button. A figure will pop up with the magnitude plot of the plant such that the frequency interval can be selected. An additional functionality is saving the controller to a Simulink model. This model is discretized using the method of Tustin with prewarping properly applied per controller block. This controller can then directly be used in an experimental setup by the use of e.g. the Real-time Workshop Toolbox from Matlab/Simulink. Last but not least, three controllers can be designed simultaneously for the same plant which facilitates comparison of controllers.

- Optimization: selection of which controller blocks are to be optimized and starting of the optimization algorithm.
- Performance indices: the performance indices are computed using both the open loop FRF and the sensitivity FRF. The computation of the bandwidth and the modulus margin are straightforward using the magnitude information of these FRFs. To compute the gain and phase margin, the phase information of the open loop function has to be determined correctly. For models, a good way to do this is to sum the phase contribution of each pole and zero of the model. Simply determining the phase of the model as a whole and then unwrapping the phase is not a robust way, e.g. the phase can shift by 360° or due to a limited frequency resolution the phase can be unwrapped incorrectly near narrow resonances. This method of determining the correct phase is used for the controller. However, the plant can consist of FRF-data for which this method can not be applied. For a correct phase margin estimation it is necessary that the phase is unwrapped correctly up

to the bandwidth frequency, which requires a good FRF measurement at least up to the bandwidth. Otherwise, the objective function can not assess stability correctly, and hence, the optimization will not return a stabilizing controller.

- Visualization: to support the control engineer by interpreting the result of a controller, response figures can be generated such as Bode plots of the plant, controller, open loop, sensitivity, process sensitivity and closed loop, the Nyquist plot of the open loop and in case of using a plant model the step or impulse time response.

C.5 Loop Shaping Example

To test the optimization aided loop shaping tool, a non-collocated system is used as shown in Figure C.3. The system consists of two masses with a rod in between. The actuator is acting on the motor mass, while the position encoder is mounted on the load mass.

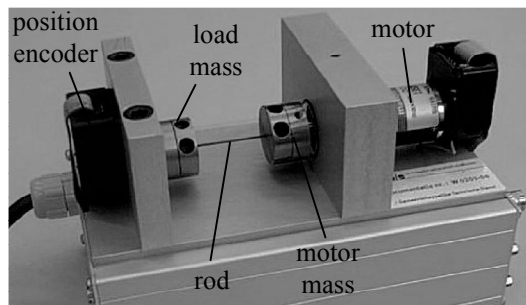


Figure C.3: Experimental setup.

FRF-measurements of 3 similar non-collocated systems are shown in Figure C.4. Differences are mainly due to small variations in the mechanics of the system. Around the resonance the phase drops from -180° to -360° which is limiting for the attainable bandwidth.

From experience, the control engineer knows that for this type of system a lead/lag filter is required to achieve stability. Furthermore, he knows that the resonance peak will cause stability problems when increasing the bandwidth due to phase loss. An integrator and a low pass filter are optional to increase gain below the bandwidth and decrease gain above the bandwidth respectively. The controller shown in Figure C.5 contains a gain, a lead/lag filter, an integrator, a low pass filter and a notch filter. First, the notch filter was locally fitted by optimization such that the resonance peaks are straightened as good as possible for all FRFs. Due to small differences in mass and stiffness, the resonances vary a little such

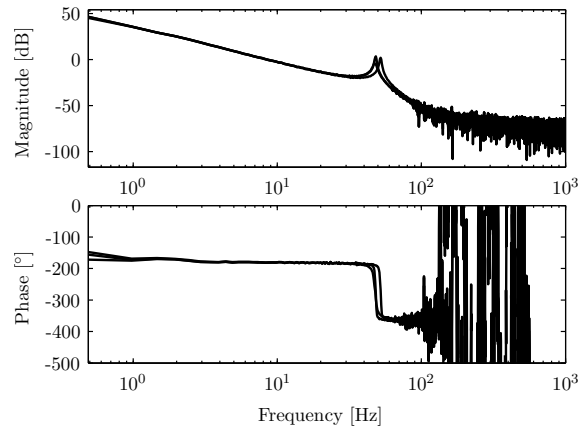


Figure C.4: Bode plot of 3 similar non-collocated systems.

that a compromising, wider notch results. After that, the other parameters are optimized with the optimization algorithm with a target bandwidth of 10 Hz, modulus margin of 6 dB, gain margin of 6 dB and a phase margin of 30° .

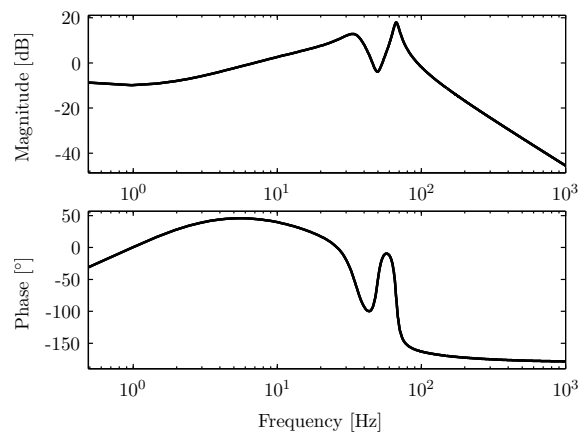


Figure C.5: Controller.

In Figure C.6 and Figure C.7 the resulting open loop and Nyquist plot are shown. The optimization algorithm managed to satisfy the target specifications for all 3 systems. The time that it takes to design this controller is only a few minutes including the optimization. The controller can be exported to ready-to-use code which makes the controller design process suited in a rapid control prototyping environment.

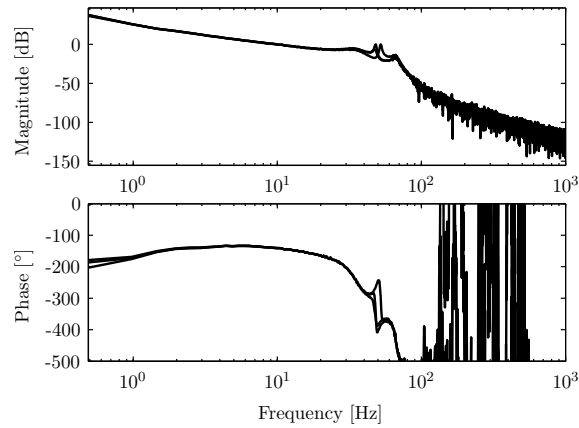


Figure C.6: Open loop.

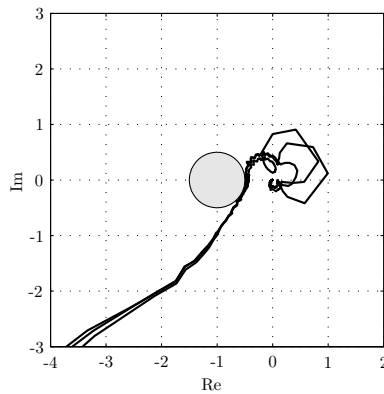


Figure C.7: Nyquist plot.

C.6 Experiments

The designed controller in the previous section is exported to ready-to-use code and tested for all 3 similar setups. In Figure C.8 and Figure C.9, the experimental step response and the response to a sine of 1 Hz respectively is shown for all setups. As expected, the behavior of all setups is similar because the performance criteria of all 3 setups are similar. The step response is an indication of how fast it can react to disturbances. The rise time of the system is approximately 0.1 s which corresponds to the closed loop bandwidth of 10 Hz. Furthermore, the response to a sine disturbance shows the disturbance rejection of the feedback controller around 1 Hz. The maximum error is about 10% of the disturbance amplitude which agrees with an open loop gain of about 25 dB at 1 Hz.

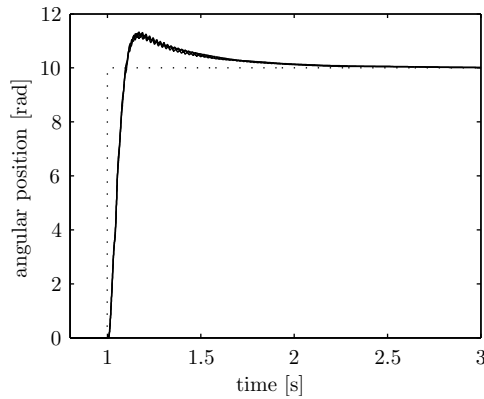


Figure C.8: Step response of the setups. The dotted line is the reference and the solid lines are the responses of the 3 setups.

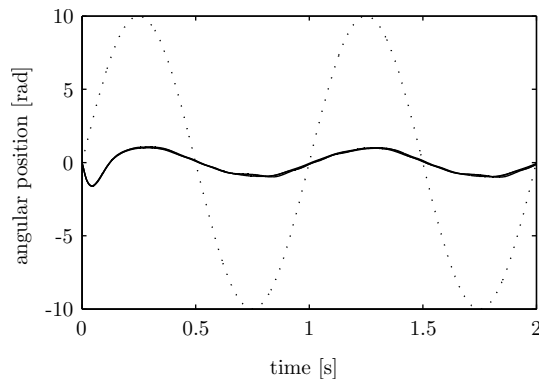


Figure C.9: 1 Hz sine disturbance response of the setups. The dotted line is the disturbance and the solid lines are the error signals of the 3 setups.

C.7 Conclusions

The optimization aided loop shaping approach as proposed here and implemented in the *Shape It* tool has shown to be a useful tool to assist the control engineer in rapidly designing a high performance feedback motion controller. The main advantages are: 1) the controller structure can be chosen arbitrarily out of a set of commonly used controller blocks, 2) measured FRF-data can be used directly for loop shaping, 3) manual loop shaping and notch placement is assisted by optimization such that the control engineer does not have to find the optimal balance between different tuning parameters which is time consuming, 4) a priori knowledge of the control engineer is easily integrated in the optimization process by fixing a selection of the controller blocks, and finally 5) the resulting controller can be exported to a discretized controller using Tustin and pre-warping

in Simulink ready-to-use for simulation and experimentation.

The approach can also be extended towards other manual tuning methods e.g. QFT tuning, where it can resolve one of the two major drawbacks of QFT (i.e. the loop shape part, not the grid problem). Also, combinations are possible with model-based designs, where model-based controllers could be used as starting point or reference.

Appendix D

Redesign of the Drive-aid

The first prototype presented in Chapter 8 has shown to be feasible, however it is still too complex to outperform a scaled conventional motor regarding cost of production and reliability. The main complexity comes from the fact that the reaction force to reverse the carriage has to be delivered by a linear guidance over a distance of about 2 cm.

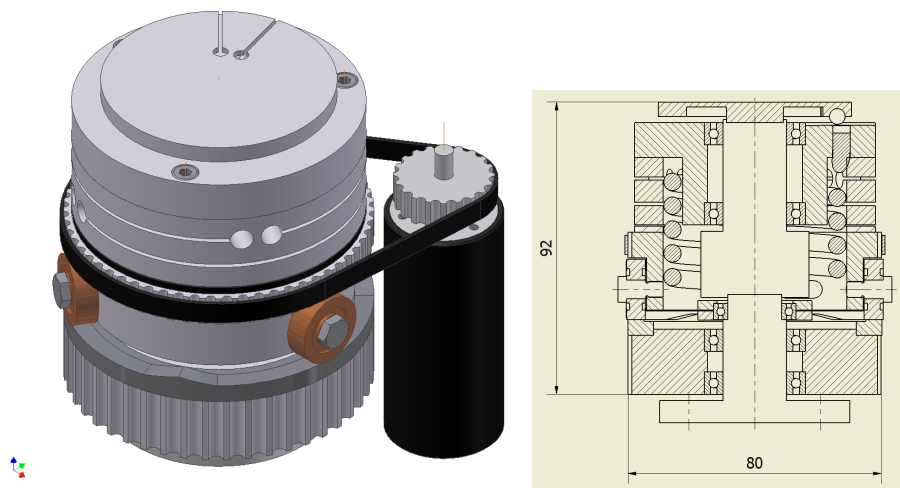


Figure D.1: Redesign of the reversal mechanism.

To overcome¹ this problem, the spring can be moved to a rotating clutch plate which is fixed for the first prototype. The result is that the clutch is engaged with

¹This work has been carried out by E. Tabak, M.Sc., which is gratefully acknowledged.

a linear guidance over a small distance via a membrane. A sketch of the design is shown in Figure D.1. The cam slope determines the normal force of the clutch, hence, whether it is self-braking or not. Because the spring is connected to the clutch plate instead of to the linear guidance, only a short cam slope is needed. The advantage of this concept is twofold:

- (i) no long linear guidance is needed anymore to counteract the reaction force of the carriage resulting in a simpler more compact design,
- (ii) no long cam slope is needed because only a short distance is required to engage the clutch and load the spring. This results in a smaller radius of the drive-aid, a lower inertia, and a smaller drive-aid motor.

Both the first prototype and the redesign are compared in Figure D.2. The volume reduces by about a factor of 2 when not including the external motor for the redesign. In Figure D.3, an exploded view is shown of the parts in the redesign. These parts are easier to built compared with the parts shown in the exploded views in Chapter 8.

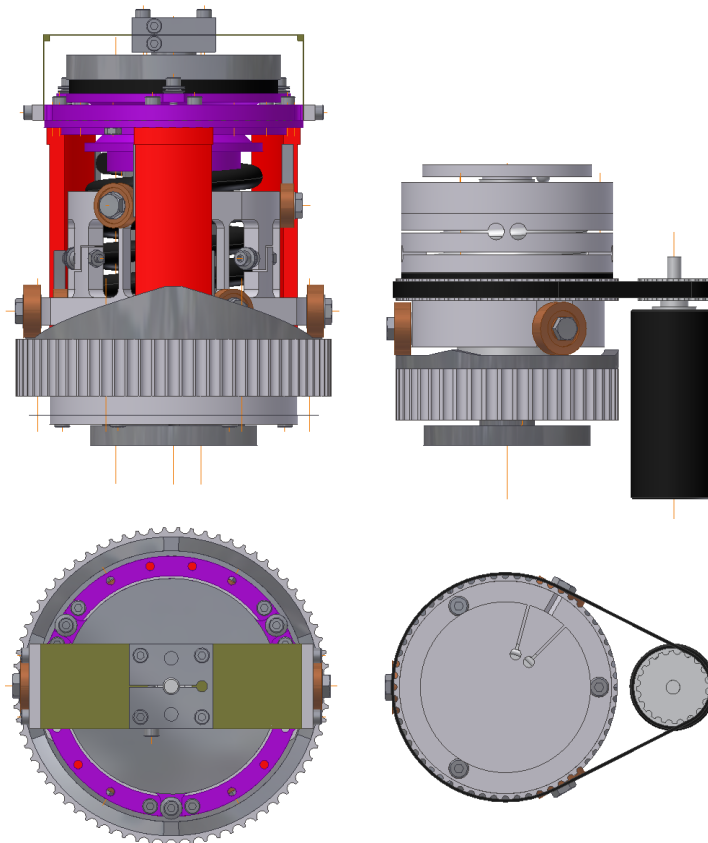


Figure D.2: Comparison of the redesign with the first prototype of the drive-aid.

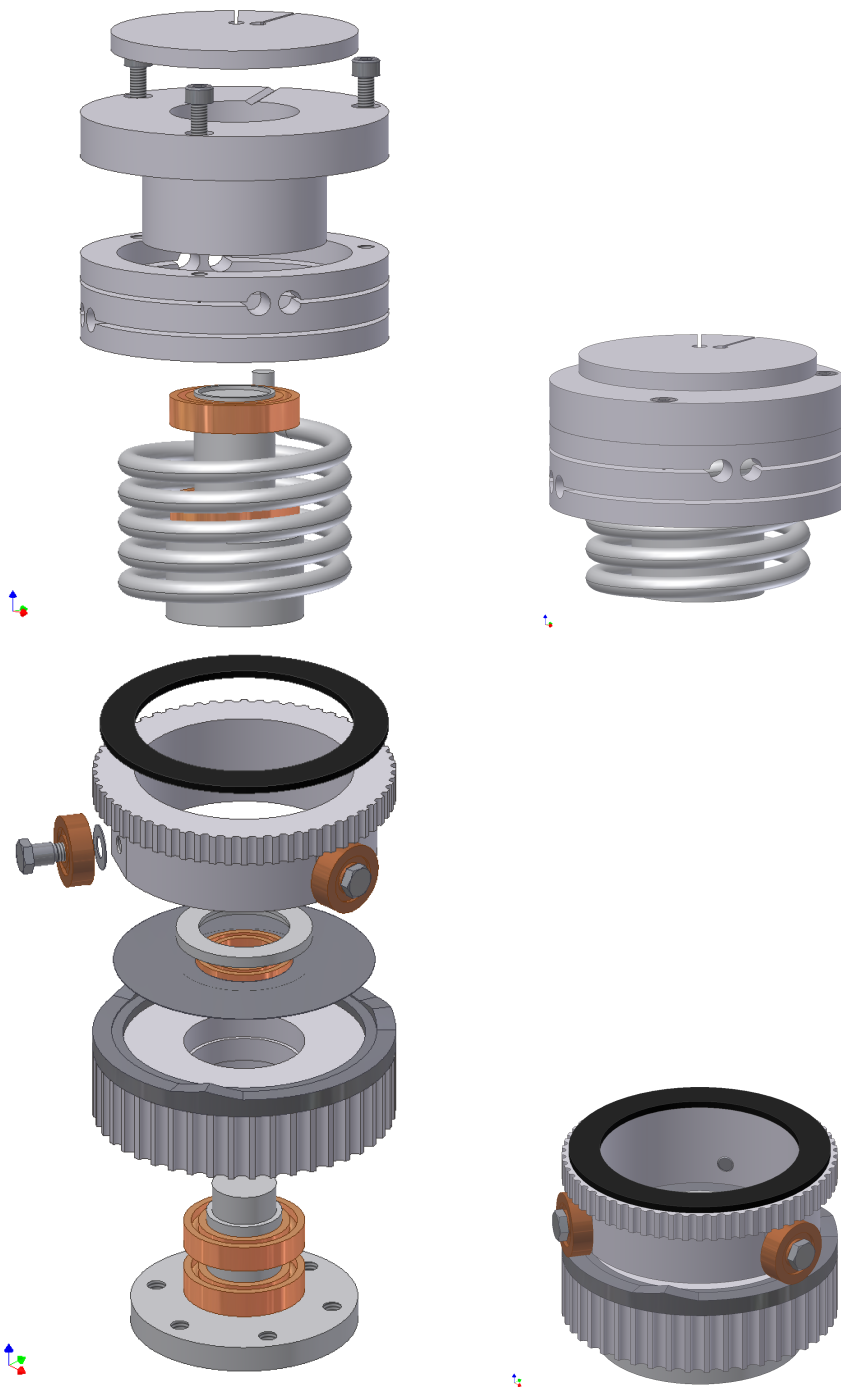


Figure D.3: Exploded view of the redesigned drive-aid.

Samenvatting

Dit werk richt zich op het verbeteren van breedformaatprinters gebruikmakend van mechatronische oplossingen. Onder "verbeteren" wordt verstaan het verbeteren van: de productiviteit, de print kwaliteit, de betrouwbaarheid en/of de fabricagekosten zonder dat dit ten koste gaat van de andere criteria. De nadruk ligt op breedformaatprinters, echter de methodologie die gevolgd wordt in dit werk is ook toepasbaar op een grotere klasse printers en andere toepassingen.

Scannende inktjet configuraties met meerdere printkoppen worden beschouwd waarbij iedere printkop honderden nozzles bevat. Dit werk richt zich voornamelijk op het beheersen van de zes graden van vrijheid in tijd en ruimte van iedere printkop. Processen die plaatsvinden in de nozzles worden niet beschouwd. Echter, de macroscopische effecten van de druppel vorming zal wel meegenomen worden zoals jet snelheid, jet timing en tijdelijk uitvallende nozzles door verontreiniging.

Een concept exploratie is uitgevoerd voorafgegaan door een productiviteitsanalyse en een print nauwkeurighedsanalyse waarbij met name mechanische ontwerpparameters zijn meegenomen in de analyse. Beide analyses zijn generiek opgezet zodanig dat ze ook toegepast kunnen worden op andere printerconfiguraties en op een breder applicatiegebied. Op basis van dit vooronderzoek zijn twee concepten gekozen en verder onderzocht.

Het eerste concept is actieve printkopuitlijning. In plaats van alle tijd en kosten te stoppen in het zoveel mogelijk verkleinen van alle maaktoleranties om een nauwkeurige printkop uitlijning te verkrijgen voor productievare breedformaatprinters, worden bij dit concept de uitlijnfouten actief gemeten en weggeregeld. Een goedkope sensor, actuator en uitlijn-mechanisme zijn ontworpen om dit te bewerkstelligen. Een experimentele opstelling is gebouwd om het concept te valideren. Het concept is haalbaar bevonden waarbij voldaan wordt aan de uitlijn specificatie van minder dan $10\ \mu\text{m}$. Bovendien maakt dit concept het mogelijk om (i) redundante printkoppen toe te voegen die het werk van tijdelijk verstopte nozzles overnemen en om (ii) printkoppen te stapelen in papier transport richting en zelfs printkoppen te verdelen over meerdere sledes. Voor conventionele breedformaatprinters zou dit niet mogelijk zijn als gevolg van thermische effecten en parasitaire dynamica.

Het tweede concept omvat een nieuwe aandrijf methode voor productievere breedformaatprinters. Productiviteitsverhoging kan gerealiseerd worden door het verhogen van het effectief aantal printende nozzles en door het verhogen van de jetc frequentie. Dit resulteert in een zwaardere slede als gevolg van de toevoeging van printkoppen en in een snellere slede als gevolg van de hogere jetc frequentie. Een verdubbeling van de massa en van de snelheid resulteert in actuatorvermogens toename van een factor zestien aannemend dat de relatieve keertijd gelijk blijft. Schaling van conventionele breedformaatprinters is daardoor duur en energie inefficiënt. Als alternatief is een concept onderzocht waarbij de aandrijving gebruik maakt van een energiebuffer. Tijdens het keren van de slede wordt de kinetische energie opgeslagen in een veer en deze energie wordt meteen geretourneerd, zodanig dat de slede in de tegenovergestelde richting beweegt. Op deze manier is er nog maar een kleine extra motor nodig om de slede op snelheid te houden waarbij alleen energieverliezen als gevolg van wrijving gecompenseerd moeten worden. Ter validatie is er een prototype gebouwd. Testen hebben uitgewezen dat het principe werkt. Echter, het prototype dient verder geoptimaliseerd en vereenvoudigd te worden zodanig dat het aanzienlijk lucratiever wordt in vergelijking met het schalen van de aandrijving in een conventionele breedformaatprinter.

Het mechatronisch ontwerp van beide concepten richten zich op een veel hogere prestatie ten opzichte van conventionele breedformaatprinters. Dit heeft geleid tot innovatieve ontwerpen die makkelijker schaalbaar zijn dan conventionele methodes. Bovendien maken deze innovatieve ontwerpen andere functionaliteiten mogelijk die niet mogelijk zijn met het schalen van conventionele breedformaatprinters.

Dankwoord

De tijd vliegt als je het naar je zin hebt en bij mij is deze dan ook behoorlijk hard voorbij gegaan. Het is alweer bijna vier jaar geleden dat ik begonnen ben als promovendus met als einddoel dit moment. Zonder de steun van alle mensen om me heen was dit hele project niet mogelijk geweest en daarom wil ik hen middels dit dankwoord bedanken.

Ten eerste wil ik Maarten Steinbuch bedanken voor het bieden van deze kans in een unieke omgeving waar ik altijd met plezier gewerkt heb. Verder wil ik René van de Molengraft bedanken voor de dagelijkse begeleiding als co-promotor. Ondanks de af en toe overlopende agenda blijf je altijd enthousiast, positief en kritisch wat voor mij een goede stimulans was. Het is een voorrecht dat ik deel heb mogen uitmaken van het "René-clubje" waarbij ik in het bijzonder de samenwerking bij verschillende onderwijstaken en Robocup wil noemen.

Van opdrachtgever Océ wil ik iedereen bedanken die me de afgelopen 4 jaar geholpen heeft met het vergaren van kennis. Specifiek wil ik Theo Heeren en Aswin Draad bedanken die me met raad en daad hebben bijgestaan door middel van een prettige en kritische begeleiding gedurende het hele promotietraject. Theo als directe begeleider vanuit Océ en Aswin als directe begeleider tijdens de inwerkstage met daarna een enthousiaste betrokkenheid.

Ook wil ik alle studenten bedanken die me tijdens het promotietraject geholpen hebben. Met name Arnoud Notenboom en Erik Tabak voor het kiezen van een afstudeeropdracht bij mij. Zonder jullie kennis en kunde was dit werk niet mogelijk geweest. De gezamenlijke besprekingen, de zogenaamde "PIM(P) meeting", was iedere keer weer genieten. Ook wil ik hierbij Linda van den Bedem bedanken voor haar inbreng bij deze bijeenkomsten. Voor de realisatie en de ondersteuning van experimenten wil ik graag Eric Homburg, Rob van de Berg, Harrie van de Loo, Peter Hamels en Pieter van Hoof bedanken.

Als afsluiting kan ik hier een hele lijst met alle namen plaatsen in de hoop dat ik niemand vergeet, dat doen we dus maar niet. Uiteraard wil ik alle DCT collega's bedanken voor de gezelligheid tijdens koffiepauzes, lunches, borrels, conferenties, squash-wedstrijden, poker- en Robocup-avonden. Afleiding van het dagelijkse

promotiewerk is gezond, bedankt allemaal! Jullie zijn de afgelopen jaren ook erg sterk geweest met het verzinnen van bijnamen voor mij, bij deze een aantal namen die IK regelmatig ben tegengekomen bij bovenstaande bezigheden: Ewouter van der Laangenent, professor Hamers, Buxus, Wevers, Smackdown Smeulen, Melly, T. Ohmi, JvH, J. the Beast, commander Marcos, Molenmeester, Hallie hallo, dmmdbdzit en uiteraard M.

Buiten het promoveren is er gelukkig ook genoeg tijd over voor andere dingen, je werkt tenslotte om te leven en niet andersom. Deze tijd breng ik dan ook graag zoveel mogelijk door met vrienden en familie. Feestjes en vakanties waren en zijn voor mij altijd genieten. Mijn ouders wil ik daarnaast nog speciaal bedanken voor de onvoorwaardelijke steun die ze mij geven. Betere ouders kan iemand zich niet wensen.

Ik wil dit dankwoord graag afsluiten met de goede raad te genieten van het leven aangezien het te mooi is om te verspillen.

Curriculum Vitae

Dennis Bruijnen was born on March 9th, 1980 in Tegelen, The Netherlands. After finishing Atheneum at the "Bouwens van der Boijecollege" in Panningen in 1998, he started his study Mechanical Engineering at the Technische Universiteit Eindhoven. The topic of his graduation project was automatic controller synthesis via Genetic Programming carried out at Philips CFT. Upon completion of his Master's degree within the Control Systems Technology group in 2003, he started as a Ph.D. student in the same group on the topic of "Mechatronic Design Exploration for Wide Format Printing Systems" in association with Océ-Technologies B.V., resulting in this thesis.